11-25-2020

Non-conventional sensors for measuring partial discharge under DC electrical stress

Mojtaba Rostaghihalaki

Non-conventional sensors for measuring partial discharge under DC electrical stress

By

Mojtaba Rostaghi Chalaki

Approved by:

Chanyeop Park (Major Professor)
J. Patrick Donohoe
Masoud Karimi Ghartemani
Mehmet Kurum
Qian (Jenny) Du (Graduate Coordinator)
Jason M. Keith (Dean, Bagley College of Engineering)

A Dissertation
Submitted to the Faculty of
Mississippi State University
in Partial Fulfillment of the Requirements
for the Degree of Doctor of Philosophy
in Electrical and Computer Engineering
in the Department of Electrical and Computer Engineering

Mississippi State, Mississippi

November 2020

Name: Mojtaba Rostaghi Chalaki

Date of Degree: November 25, 2020

Institution: Mississippi State University

Major Field: Electrical and Computer Engineering

Major Professor: Chanyeop Park

Title of Study: Non-conventional sensors for measuring partial discharge under DC electrical stress

Pages in Study: 152

Candidate for Degree of Doctor of Philosophy

Partial discharge (PD) is a micro discharge that occurs in defected regions within the insulating media. As these discharges are the main culprits that cause dielectric material aging, PD measurements have been used for assessing insulating materials, including solids, liquids, and gases for power applications. There are various methods and sensors available for measuring PD sensitive to specific characteristics and operable over a wide range of frequencies. Most PD measurement techniques provide patterns that enable PD interpretation more comfortable for users. For example, in AC applications, the phase-resolved partial discharge (PRPD) technique provides identifiable patterns for distinguishing various types of PDs. However, the establishment of meaningful patterns to multiple types of PD in DC systems requires more sensitive and accurate measurements of individual PD pulses with noise rejection functionality due to the lack of phase-resolved information.

Investigating of the transient phenomena such as individual PD pulses requires well-designed circuits with sufficiently large bandwidths. Waveshapes can be easily disturbed by background noise and deformed by the frequency response of measuring circuits and data acquisition systems (DAQ). Noises are unwanted disturbances that could be suppressed by suitable

filters or mathematical methods. Measurement circuits and DAQ systems consist of transmission lines, sensors, cables, connectors, DAQ hardware, and oscilloscopes. Therefore, matching the impedance of all components guarantees a reflection-free path for traveling signals and addresses most of the challenges relevant to transient measurements.

In this dissertation, we proposed and designed an appropriate testbed equipped with high bandwidth transmission line and electromagnetic field sensors suitable for investigating PD under DC electrical stresses. We comprehensively used finite element analysis simulations through the COMSOL Multiphysics software to design the dimensions and evaluate the frequency response of the testbed, transmission line, and electromagnetic sensors. Furthermore, based on the new testbed, DC PD measurements were performed using conventional and non-conventional sensors. Finally, various types of DC PD were statistically classified based on the proposed testbed.

Keywords: Partial discharges, cavity discharge, corona discharge, surface discharge, floating potential discharge, treeing, stress, degradation, COMSOL Multiphysics, electrostatic, radio frequency, electromagnetic fields, conventional sensors, non-conventional sensors, transmission line, D-dot, B-dot, pattern recognition method, phase-resolved partial discharge, time-resolved partial discharge, PD waveshape, shunt resistor, high frequency current transformer, loop antenna, monopole antenna.

DEDICATION

To my beloved wife, Mansoureh!

ACKNOWLEDGEMENTS

I would like to express my deepest gratitude to my former advisor Dr. Joni Klüss, for giving me this opportunity to work under his supervision during the first five semesters of my Ph.D. I am grateful to my current advisor, Dr. Chanyeop Park, for his support, especially in the last three semesters of my Ph.D. I am sincerely thankful for all the knowledge and supports that I received from Dr. Patrick Donohoe and Dr. Mehmet Kurum during my research at MSstate. I would also like to thank Dr. Masoud Karimi for serving as my committee member.

My thanks also extend to Dr. David Wallace, Mr. Jeremy Hamilton, Mr. Josh Weaver, and Mr. Jayson Warden for helping me while running my research and experiment in the High Voltage Lab. I would also like to thank all my friends in Simrall, Saeed, Maryam, Kamran, Pedram, Maziar, Nasim, Ali, Zeeshan, and Farhina for their precious supports. Lastly, I am thankful to all members of the Iranian Student Association (IRSA) at Mississippi State University, who made my life in Starkville more pleasant.

TABLE OF CONTENTS

LIST OF TABLES

LIST OF FIGURES

SUMMARY

The measurement of PD pulse waveshapes depends on the measurement circuit elements. For example, a similar type of PD discharge will appear differently depending on the measurement circuit, sensor, and acquisition unit (*i.e.*, transfer function). Moreover, there should be a significant difference among the measured PD pulses in the field compared to the waveshapes captured in laboratories due to the unpredictable disturbances. This dissertation addresses the requirements of precise individual PD pulse measurements for both AC and DC systems. The accurate measurements of individual PD pulses allow the extraction of useful information about PD waveshape characteristics. The information includes parameters such as rise time, decay time, amplitude, etc. which leads to the classification and recognition of various PD types caused by distinct types of defects.

Four common types of individual PD pulses – cavity, surface, corona, and floating potential discharges – were investigated under AC and DC stresses. The examinations of these types of PDs in this work provide useful information about their discharge mechanisms and quantitative studies of their waveform characteristics and frequency spectrums. Also, the time domain analysis of measured PD waveforms in this dissertation demonstrates apparent differences between AC and DC PDs. These data provide enough information for the statistical analysis of the waveform of PD. Similarly, the results of frequency domain analysis present the distinct characteristics among the frequency spectrums of PD defects in both AC and DC. That is, the results of this work allow the classification of PD according to the frequency components under both AC and DC electrical

stresses. The proposed method of this dissertation helps in mapping various types of PDs based on the time domain characteristics of PD waveforms and their amplitudes. One of the advantages of this method is its independence from the repetition rate of PD pulses under DC stresses, which takes a long time to record data (specifically in DC). The other advantage of this mapping is that the distinguishing and clustering of data can be performed by either of the rise time, decay time, and pulse width of PD waveforms.

In addition to the contributions above of this dissertation, the application of electromagnetic fields – D-dot and B-dot sensors – in capturing individual PD pulses provides more safety during measurement. The electromagnetic field sensors in this work are commonly the inductive or capacitive coupling sensors, which avoid direct connection of energized element and DAQ systems. It is essential to prevent the damage of DAQ systems in the case of failures occurring in the PD samples.

CHAPTER I

PROBLEM STATEMENT

PD measurements employ for assessing the quality and health of medium- to high voltage (HV) applications. Extensive research on developing online and offline PD detection methods for HVAC equipment has led to the establishment of AC PD measurement techniques [1]–[4]. Similarly, the demand for research on DC PD detection and classification methods has increased with the growing use of HVDC transmission systems and MVDC distribution systems. Most of the available AC PD detection methods and standards are focused on the PRPD patterns [2], [3] owing to the phase-resolved information available in AC systems. In contrast, due to the lack of phase in DC systems, most of the DC PD identification methods that have researched are based on temporal information known as time-resolved PD patterns [2], [4], [5]. The TRPD methods are majorly dependent on the repetition rate and timing characteristics of individual PD pulses, such as rise time, decay time, and pulse width. Technically, TRPD methods mostly use the statistical analysis of the individual PD pulses in quantifying their waveform characteristics and trends to find meaningful patterns. There are a variety of TRPD methods have used in the interpretation of various types of PDs. Some of the techniques focus on PD repetition rates to find trends related to stress changes and pulses. At the same time, some concentrate on the corresponding PD pulse characteristics (e.g., rise and decay times) [6]–[8].

Despite the existence of these methods, the lack of well-established DC PD measurement standards and practices threatens the dielectric integrity and system reliability of DC power applications. For example, there are reported cases where AC PD test procedures apply to evaluate DC cables and devices [4], [9]. Although using AC voltage to DC applications for PD measurement purposes may generate PD signals, their characteristics, including PD inception voltage (PDIV) and PD magnitude, may differ substantially compared to cases where DC voltage is applied. These differences are caused by the inherent differences of electric field distributions in dielectric materials under AC and DC electrical stresses. Hence, it is evident that DC power applications require their PD detection methods and standard procedures [4], [9]. Similarly, the results of recently published papers focusing on the comparison of AC and DC PDs also confirm the need for DC PD identification methods for the dielectric assessment of DC apparatus [9]–[12].

CHAPTER II

STATE OF THE ART

DC networks are overgrowing in various industries (e.g., transmission and distribution grids, electric ships, aircraft, and power-electronics-driven systems) and becoming effective alternatives of conventional AC systems owing to their advantages, including the capability of carrying more power with lower loss over long distances, the increasing availability and reducing cost of renewable energy sources, and the flexibility of converting energy among unsynchronized networks. However, the reliability of these power networks are threatened by the accelerated dielectric material aging and failure of subsystem components such as cables, transformers, switchgear, insulators, and bushings under DC electrical stress. Therefore, accurate and reliable assessments of these components are necessary to ensure the reliability of DC power networks.

Generally, insulating materials in all forms of solid, liquid, and gases or a combination of those are utilized in the design of high voltage apparatus to isolate high voltage conductors from the ground. Also, the role of insulators is to provide enough clearances and make the electric fields more uniform. However, the aging of insulating materials of HV equipment in service would limit their performances and reliabilities. There are various types of defects, failures, and faults that affect the reliability and performance of insulating materials. Partial discharge is one of the most chronic and unavoidable dielectric challenge that causes accelerated dielectric material aging and device failure. To name a few, the existence of metal particles in gas insulated substations (GIS)

causes PD that lead to system failure by generating floating potentials, flashover, carbonization along with spacers, and decomposition of gases [2], [13]. In the cases of cables, bushing, and transformers that are electrically insulated mainly by solid and liquid insulators, the inevitable formation of air bubbles (in liquid) or cavities (in solid) during the manufacturing processes leads to the generation of internal PDs [3], [9].

2.1 Types of Partial Discharge

Generally, PD under both AC and DC stresses are classified into the following discharge groups [14]–[17].

- Corona Discharge
- Internal Discharge
- Surface Discharge
- Treeing

2.1.1 Corona Discharge

Corona discharges occur around the sharp points or rough surface of conductors, where the intensity of the electric field at the tip of the conductor increases and causes the degradation of insulating material by gas ionization and streamer discharges. Corona discharge happens in gases and liquids. The byproducts of corona in various insulation materials would be hazardous and damaging. For example, corona in the air can make ozone (O_3), in oil can make small particles that leads to pollution and breakdown, and in sulfur hexafluoride (SF_6) makes poisonous gases [16]. Figure 2.1 shows the picture of corona discharge in air.

Figure 2.1 Corona discharge in the air [18]

2.1.2 Internal Discharge

Internal discharge happens inside gas filled cavities or bubbles surrounded by the bulk of insulating material. The weak insulating strength of cavities leads to the internal discharge inside the solid and liquid insulations under the high electric field. Internal discharge provides the floating particles in liquid and protrusion or hot spots in solid dielectrics, which result in their failures. Figure 2.2 illustrates various types of internal discharge in solid insulation.

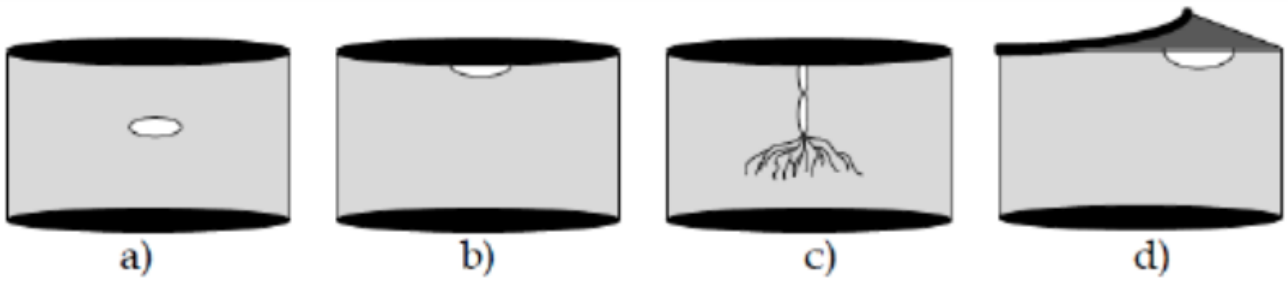

Figure 2.2 Internal discharges, (a) isolated cavity, (b) cavity with conductor contact, (c) cavity developed to an electrical tree, (d) cavity in the interface of dielectric materials [14].

2.1.3 Surface Discharge

Surface discharge occurs along with the interface of two different insulation materials when electric field becomes higher than the dielectric strength of the interface. Examples of surface discharge could be the discharges along the surfaces of solid and liquid or solid and gas insulators. Surface discharges cause degradation on the surface of insulating materials. For example, surface discharge results in the degradation of mechanical and electrical properties and causes chemical reaction of polymeric insulators [15]. Figure 2.3 shows a sample of surface discharge degradation.

Figure 2.3 Surface discharge propagation along the outer surface of the XLPE cable.

2.1.4 Electrical Treeing

Electrical treeing in solid insulation material is mostly considered a type of internal discharge (Figure 2.2c). It is commonly initiated by cavities or the interfaces of high voltage conductors and solid insulators, and progresses within the insulator and forms several branches. The growth of electrical trees is destructive and develops conductive channels, which leads to the breakdown along the insulator [15], [16]. Figure 2.4 shows the evolution of electric tree formation up to the conductive discharge channel formation.

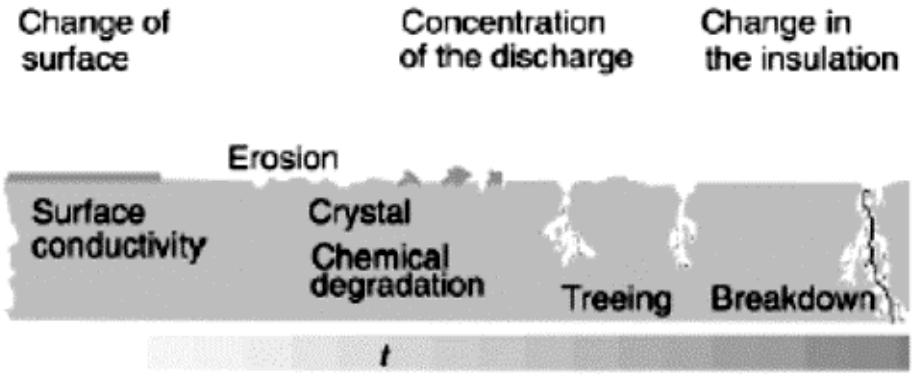

Figure 2.4 The evolutions of electric treeing within a solid insulator [15].

2.2 Partial Discharge modeling in DC

There are two extended models for the mechanism of the PD occurrence within the insulation material (specifically for internal discharge) under DC stresses. These models, which are presented by Morshuis [19] and Lemke [20], [21], are called capacitive (abc) model and dipole moment, respectively. Both of the mentioned theories are based on the common concepts for modeling electric field enhancements inside cavities. According to [22], the intensity of the internal electric field within a cavity in AC results from the residual charges from prior PDs and applied voltages. Similarly, in DC, besides of two mentioned parameters, the electric field of deposited charges exceeds the electric field intensity inside a cavity.

2.2.1 Extended Capacitive Model [19]

Figure 2.5 shows the equivalent circuit of cavity discharge at DC voltage. Here, the cavity discharge is modeled by C_c and R_c in parallel with a spark gap. Also, the rest of the insulation and insulations in contact with the cavity are simulated by C_a, R_a, C_b, and R_b, respectively.

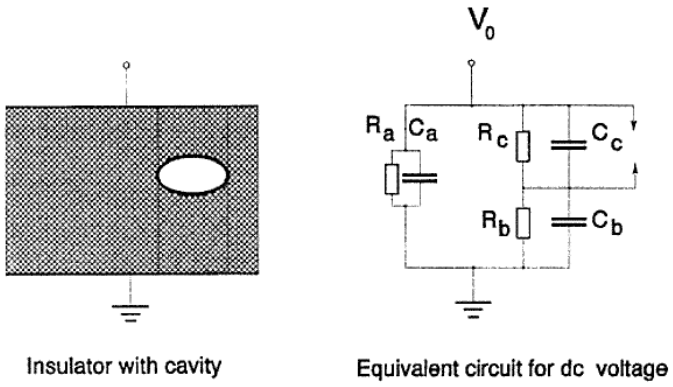

Figure 2.5 The equivalent electrical circuit of internal partial discharge at DC voltage [19].

Therefore, the charging time constant of the cavity follows the Equation (2.1).

$$\tau = \frac{R_b R_c (C_b + C_c)}{R_b + R_c} \tag{2.1}$$

Also, the drop voltage across the cavity is given by Equation (2.2).

$$V_c(t) = V_{c,\infty} - \left(V_{c,\infty} - V_r\right) e^{-\frac{t}{\tau}} \tag{2.2}$$

Where, $V_{c,\infty}$ is the max limit voltage across the cavity before PD occurrence, and V_r is the remained voltage across the cavity after PD occurrence, which are shown in Figure 2.6.

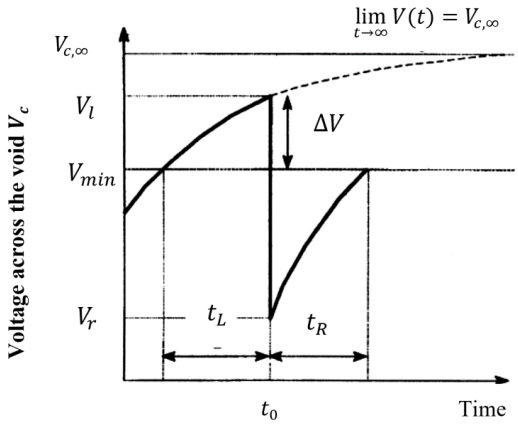

Figure 2.6 The diagram of voltage across the cavity before and after PD discharge at DC.

As seen in Figure 2.6, when the V_c approaches the minimum breakdown voltage across the cavity (V_{min}), which is caused by the increase of the electric field resulting from an increase of voltage or deposition of more charges, the process of discharge channel formation initiates in the presence of free electrons. Consequently, after elapsing of stochastic time lag (t_L), PD occurs across the cavity, and voltage falls to V_r due to the charge displacement. t_R is also called the recovery time, which presents the required time for approaching the V_{min} for the next discharge. Also, the waveshape of discharge displacement current in this model is described by two well-known discharge mechanisms *Townsend-like* and *Streamer-like*, which are introduced by Devins. The main characteristics of Streamer-like discharges are rise time values in the range of hundreds of ps and decay time values in the range of ns. In contrast, Townsend-like discharges include slow discharges with rising time values in the range of tens of ns, which follow the rate of electron avalanche formation and result in slow decaying time.

2.2.2 Extended Dipole Model [20]

According to the experimental research performed by Lemke in [20], the spark discharge phenomenon cannot occur in air cavities surrounded by dielectrics. Therefore, the discharge displacement current within the cavity should not simulate with two well-known discharge theories (the Townsend-like and Streamer –like). In opposite, he believes the dipole model was introduced by Pedersen could be a better alternative for describing this phenomenon. As seen in Figure 2.7, when the positive and negative charges deposit along the cathode and anode sides of the cavity, the corresponding electric field within the cavity forms as a dipole moment in the opposite of the main electric field. Consequently, the electric field within the cavity decreases and leads to disappearing more ionization for a specific time called recovery time.

Based on this model, the internal charge and transient voltage collapse across the cavity are not straightly proportional to cavity capacitance, which contrasts with the capacitive abc model for PD. The discharge waveshape in this model is described only with drifting of a massive number of electrons. Also, positive ions do not have any role due to their lower drifting speed.

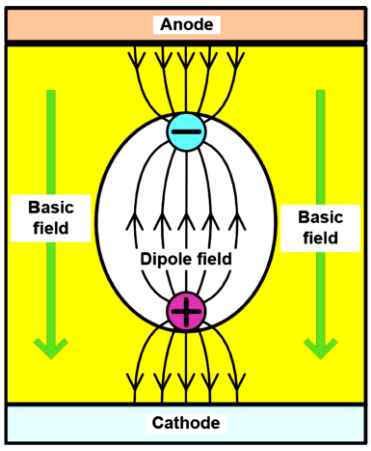

Figure 2.7 The dipole model of a cavity discharge extended between anode and cathode [20].

Furthermore, the dipole model expresses within the cavity the free electron only can produce through the neutral gas molecules. The quantities of corresponding molecules are very low in the face of electron liberated through the photo-ionization and collision, which require the formation of the spark discharge channel. As a result, consideration of full cavity capacitance discharge through the internal discharge is misleading. Thus, the possibility of strong spark occurrence within the cavities surrounded by dielectrics is very low because of the decent ionization process.

2.3 Partial Discharge Measurement

PD is a transient phenomenon, and observing fast phenomena can be challenging. If the observed event is faster than the response of the measurement system, errors will introduce, and the waveform will appear distorted and attenuated [23]. To fully understand the observed output, one must be aware of the input characteristics. Depending on what sensor uses to capture an event, the same phenomena may be viewed differently by varying acquisition devices. Challenges with PD are related to its uniqueness and ever changing nature. Even if observations are accurate and precise, their validity may be constrained to specific circumstances, materials, or fault types, thereby making universal application infeasible. PD patterns change as the source of defect changes. It is dependent on stress type, repetition rate, duration, and sample characteristics. On the measurement side, signal propagation, sensor characteristics (sensitivity, frequency response, calibration), attenuation, and noise, as well as interpretation of data, all influence assessments, and conclusions [23].

2.3.1 PD Measuring circuit

The PD measurement setup under DC stress, in most of the research studies has been performed [24]–[27], is based on the recommended test setup for PD measurement according to IEC 60270 in Figure 2.8.

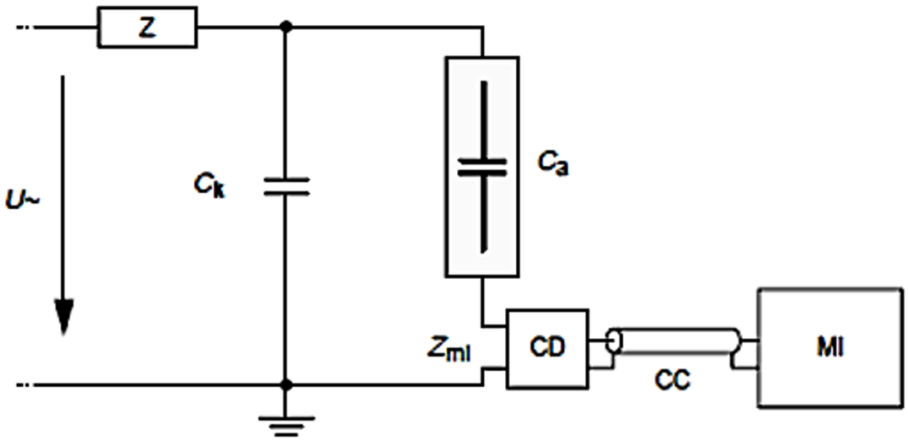

Figure 2.8 Recommended PD measurement test setup by coupling device in series with the test sample in IEC standard 60270 [28].

In Figure 2.8, U is the power supply, Z is the filter, C_k is the coupling capacitor, C_a is the test sample, CD is the coupling device (sensor), CC is the connecting cable, and MI is the measurement unit. The sensitivity and type of sensors, matching impedance of the measurement connection circuit, and measuring unit's bandwidth and sampling rates significantly affect accurate PD detection. Providing the matched impedance transmission line for transmitting the PD signal to the digitizer (matching impedance about 50 Ω which includes all the sensors output, connectors, cables, and digitizer input impedances) is required for minimizing the distortion of measuring PD pulses [24]. Figure 2.9 illustrates an example of a suitable test setup with a precise transmission line suitable for PD measurement.

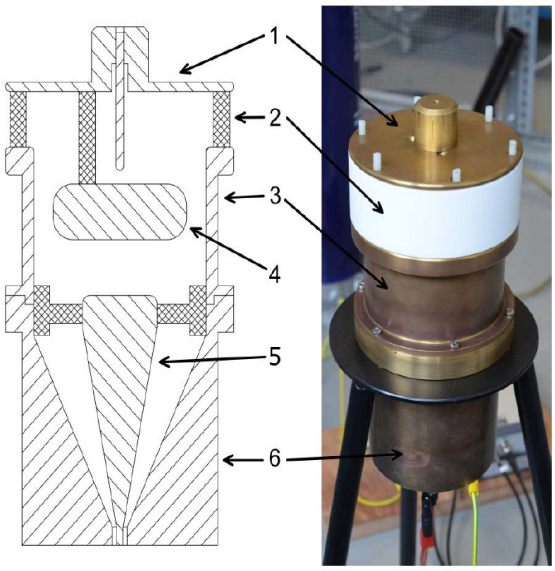

Figure 2.9 An example of a PD measurement test setup with an ideal transmission line [26], (1) HV Conductor, (2) PVC Insulator, (3) Shielding, (4) Coupling Capacitor, (5-6) Conical Transmission Line.

This test setup provides good shielding around the PD discharge location and avoids the radiation of electromagnetic fields to the outside of the test setup. This configuration terminates the PD signal to the measuring circuit through an ideal conical (tapered coaxial) transmission line, which enables a suitable connection to measuring cable s. Also, this configuration provides sufficient space for integrating the suitable coupling devices along the consistent (ideally matched) portion of the transmission line. The ideally matched transmission line prevents the reflection and attenuation of signals, particularly for high frequency components.

Generally, the coupling devices are commonly used for measuring the PD discharges divide into two different groups of conventional and non-conventional sensors. According to [29], conventional inductive couplers (e.g., quadripole, shunt resistors, HFCT, and Pearson CT) are the most widely used non-intrusive measurement technique. These sensors install onto ground

connections of HV devices (when available). As current flows to the ground circuit, signals induce into the measurement unit. Non-conventional sensors (e.g., inductive or capacitive coupling sensors and VHF/UHF antennas) convert electromagnetic waves into voltage or current. Probes intended for electric fields are designed with rods and planes, while sensors for magnetic fields utilized conductor loops. When a propagating electric field reaches the probe, an impressed voltage would observe along the probe length relative to the ground [15]. Moreover, other examples of non-conventional sensors are such as ultrasonic sensors, optic sensors, and the DGA methods. Ultrasonic sensors capture acoustic waves generated by PD activities, optic sensors detect light emitted by PDs, and the DGA method measures the level of byproduct gases resulted from PD activity, specifically in the insulating oils [1], [30].

The selection of a suitable sensor for PD measurement is mostly related to a way that PD manifest itself. In other words, depending on the insulating media is used in an HV apparatus, the physical characteristics of PD activities can be recognized better by a specific type of sensor. For example, electromagnetic waves resulted from PD can propagate with lower attenuation in gases respect to the solid or liquid dielectrics. Similarly, PD measurement situation and location is critical on the selection of suitable sensors. For instance, because of existing external noises and disturbances, most of the conventional sensors are not suitable for a field PD measurement, and operators utilize a non-conventional sensor. In the following, we discuss more various types of PD sensors and their principals.

2.3.2 Frequency Characteristics of Partial Discharge Measurement Units

As mentioned earlier, the accuracy of PD measurement is related to the characteristics of various elements in the measuring circuit. For example, in [31], it is shown somehow, a PD pulse can be affected by the measuring circuit. Figure 2.10 represents the result of measuring a typical

5 nC gaussian PD pulse with a 20 ns pulse width through two various filters with 30 MHz and 5 MHz bandwidths.

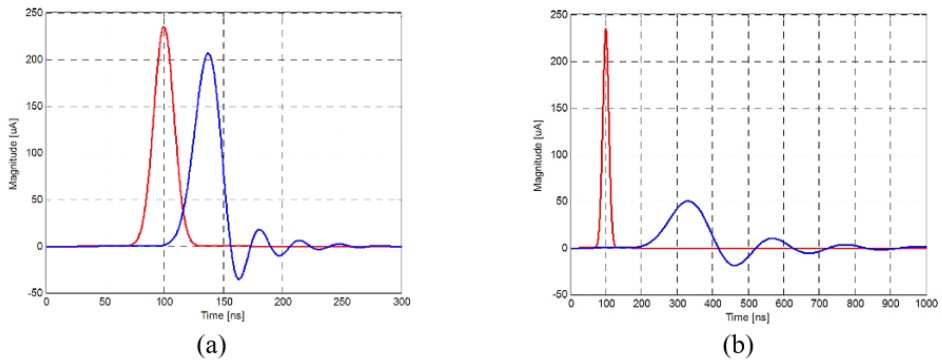

Figure 2.10 Measurement of 5 nC gaussian PD signal with 20 ns pulse width through the low pass filter circuits. (a) 30 MHz bandwidth, (b) 5 MHz bandwidth.

As shown in the figure, the selection of measuring circuits or sensors with insufficient bandwidth change the waveshape of PD signals and cause loss of data. The amplitude and pulse width of the original PD signal in Figure 2.10 are affected by both measuring circuits. IEC 60270 standard recommends measuring the apparent charge of PD to overcome the limitations of PD measurement. The apparent charge is equal to the area under the captured PD signal. The apparent charge measurement method is an alternative way of measuring PD signals without accurate measurement of PD signal waveshape. However, the application of measuring circuits with various transfer functions results in the PD signals with different amplitudes and durations. Consequently, the IEC 60270 standard classifies the PD measuring units to three groups that are suitable for different applications. These categories are explained in the following.

- **Wide-band PD Detection Instruments**

The transfer impedance Z(f) of the measuring instruments in this group has two fixed lower (f_1) and higher (f_2) limit frequencies as well as a specific bandwidth Δf which their values recommended in the standard.

$$30\ kHz \leq f_1 \leq 100\ kHz$$

$$f_2\ \leq 500\ kHz$$

$$100\ kHz\ \leq\ \Delta f \leq 400\ kHz$$

These types of sensors would have a well-damped response to the PD pulses in which determines both PD current polarity and apparent charges.

- **Narrow-band PD Detection Instrument**

These instruments have a narrow bandwidth Δf with a midband frequency f_m, which varies between the below limits.

$$9\ kHz\ \leq\ \Delta f \leq 30\ kHz$$

$$50\ kHz \leq f_m \leq 1\ MHz$$

The output voltage of these sensors in the face of PD pulse is a transient oscillating voltage whose peak is proportional to the number of charge displacements.

- **Ultra-wide-band PD Detection Instruments**

Standard explains, "*Partial discharges can also be detected by oscilloscopes providing very high bandwidth or by frequency selective instruments (for example, spectrum analyzers) together with appropriate coupling devices. The aim of application is to measure and to quantify*

the shape or the frequency spectrum of partial discharge current or voltage pulses in equipment with distributed parameters, for example cables, rotating machines or gas insulated switchgear, or to provide information about the physics or origin of the discharge phenomena". Thus, the application of sensors with the bandwidth in the range of MHz or GHz is suitable for investigating the waveshapes of PD pulses.

Recently, the application of high frequency coupling sensors and antenna with different types of bandwidths (e.g., VHF (30-300 MHz) and UHF (0.3-3 GHz)) has increased for PD measurement in AC fields. As expressed earlier, the conventional PD measurement sensors detect the apparent charge through the coupling capacitors. Their sensitivity depends on the ratio of the coupling capacitors to the test object capacitance [32]. Therefore, the high frequency sensors could be a good alternative for the conventional PD measuring instruments, which frequently suffering noises in the fields. Due to the high signal to noise ratio (SNR) among the VHF and UHF sensors, these sensors can easily suppress the external noises and disturbance. However, the determination of the midband frequency and type of bandwidth is important for more accurate measurement [33].

2.3.3 Common types of PD Detection instruments

As mentioned, the identification of the DC PD waveform requires accurate PD detecting instruments. These instruments vary by how PD pulses manifest themselves (e.g., discharge current pulses, electromagnetic waves, etc.) and are divided into the subcategories of conventional and non-conventional sensors. The conventional PD sensors refer to the detecting instruments following the IEC 60270 criteria for bandwidth, upper, and lower frequencies. In contrast, the non-conventional ones refer to sensors such as the electromagnetic field ones that measure propagated electromagnetic fields by PD signals in the range of 3 MHz to 3 GHz. Ultrasonic sensors capture acoustic waves generated by PD activities, and optic sensors detect light emitted by PDs [1], [30].

Also, the non-conventional sensors are type of sensors that have not limited to IEC 60270 limitations like frequency bandwidth or apparent charge scaling of PD signals. Examples of conventional sensors include shunt resistors, capacitive dividers, and inductive coupling sensors (e.g., HFCTs). Similarly, non-conventional sensors are electromagnetic field sensors (commonly named UHF sensors) such as Loop antennas, Monopole antennas, and acoustic sensors. The followings are a brief explanation of the most common types of PD sensors.

2.3.3.1 Shunt Resistor

A shunt resistor is one of the conventional coupling devices that operates to measure the charges replacement currents through the connection leads. Multiple resistors could be parallel together and make the required 50 Ω impedance to decrease the inductance of the shunt resistor and avoid mismatching impedance in the measurement circuit. Paralleling a series of resistors in shunt resistor sensors improve the frequency response of the sensor and is suitable for measuring the low current for a wide range of frequencies [34].

2.3.3.2 HFCT

A current transformer converts the time-varying current into a corresponding voltage (or current) signal that can be scaled based on the turns ratio of the transformer. Several design criteria described in [35], including avoiding high turns ratios (results in high leakage inductance – secondary output is less than predicted from primary and turns ratio, resulting in output error) and evenly spacing the secondary completely around the core. The magnetic core makes potentially from grain oriented silicon-iron for power frequency applications and metallic oxide materials (ferrites) for high frequency current transformers (HFCT) [29]. HFCTs are common inductive couplers installed on the ground connection of a device or sample. Current flowing along the

conductor through the HFCT induced a voltage measured across a resistive load. The primary is normally a single turn (straight conductor). The coupling strengthens by increasing the number of turns in the primary.

2.3.3.3 Loop Antenna

The loop antenna functions like an inductor coil coupling with the time-varying magnetic field of the radiated wave, inducing current into the wire loop. The sensitivity of the loop antenna is a function of sensors orientation. In electromagnetic waves, the magnetic and electric fields are transverse (transverse electromagnetic waves, TEM, where oscillations are perpendicular to the propagation direction). Hence, if the magnetic field is directed perpendicular to the direction of propagation, the loop plane should be aligned in parallel to the propagation direction of the TEM wave for the sensor to detect the field. However, presented model for inductive coupling sensors, as shown in Figure 2.11, consists of a mutual inductance M between the sensor and the lead passing the displacement charge and self-inductance L of the sensor [36].

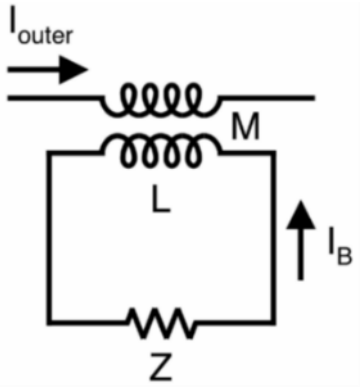

Figure 2.11 Equivalent circuit of inductive coil coupling sensors [36].

2.3.3.4 Monopole Antenna

"*A vertical cylindrical monopole element at the center of a horizontal circular ground plane is the simplest monopole antenna geometry because its structure and radiation pattern are both invariant in the azimuthal direction*" [37]. A monopole antenna is half of a dipole antenna placed on top of a ground plane. Assuming the plane is large enough (infinite) and perfectly conducting, the monopole antenna will be equivalent to a dipole whose lower half is the image of the upper half – i.e., the radiation pattern in the upper hemisphere will be identical to that of a dipole. Infinitely large ground planes are not feasible. The larger the plane, the lower the tilt/direction of maximum radiation (as the ground plane size approaches infinity, the radiation pattern approaches the horizontal x-y plane). Imperfectly conducting ground has a similar impact of tilting maximum radiation to higher angles. Radiation efficiency with perfect ground planes is 100%. An electrically short monopole element close to dielectric earth can have almost 0% [37]. Besides, edge diffraction of the ground plane, proximity to grounded objects, Fresnel reflections can all impact sensor performance. Standard monopole measures λ/4 in height, and to function properly, it must mount on a large conductive surface. The gain of the monopole increases as ground plane size increases – 2 dBi for λ/2 ground plane, 3 dBi for 2λ plane, and 5 dBi for infinite ground. In addition, the thickness of the monopole antenna determines its bandwidth (thicker conductor, higher bandwidth), and resonant frequency can be increased by decreasing monopole length [38]. However, the monopole antenna has been modeled by a capacitive coupling sensor in [36] is shown in Figure 2.12. In this model, the C_D is the capacitance between the head of sensor and the opposite conductor (HV conductor in PD measurement), C_{Stray} is the leakage capacitance between the sensor's tip and its ground, and Z is the impedance of the connection cable.

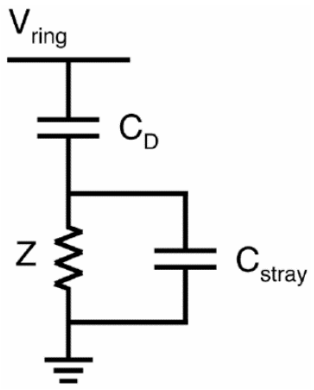

Figure 2.12 Equivalent circuit of capacitive coupling sensors [36].

2.3.3.5 UHF Sensors

Recently, non-conventional high-frequency coupling antennas that operate on the ranges of UHF increasingly are used for measuring PDs in AC systems owing to their advantages such as superior sensitivity, broad frequency range, and reduced external noise [32], [39]–[41]. The UHF sensors that analyze PD pulses by capturing their electromagnetic fields, specifically in GIS systems, are good alternatives to conventional PD detection sensors. These sensors are designed and utilized in a range of frequencies between 300 MHz and 3 GHz (commonly called UHF sensors). The sensitivities of UHF sensors employed in PD monitoring is related to parameters such as location, type of PD, equipment dimension, PD electromagnetic fields radiation within insulating media, frequency response, etc. [1].

However, there is too much flexibility in the design of UHF sensors, which makes them unique for various conditions of PD measurement. The UHF sensors normally design for narrow-band and wide-band applications, or even a combination of both. Figure 2.13 denotes the narrow-band and wide-band ranges utilized in the PD measurement with UHF sensors. The narrow-band

technique comprises the variable range of frequencies between 3 and 10 MHz, while the wide-band designs include frequency ranges from 200 MHz to 2 GHz [1].

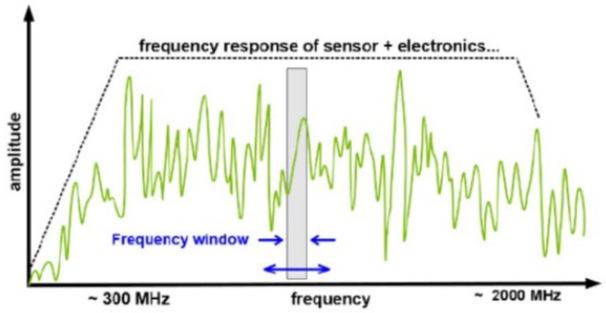

(a)

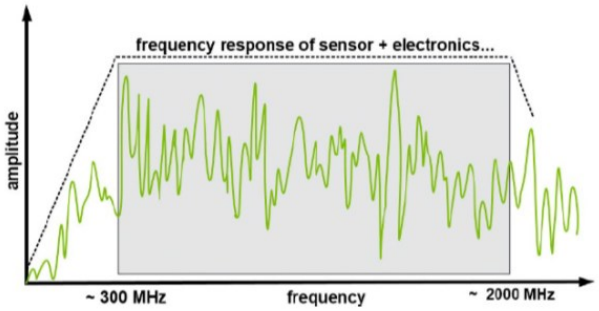

(b)

Figure 2.13 Example of variable bandwidth of frequency used for PD measurement with UHF sensors [1]. (a) narrow-band technique. (b) wide-band technique.

2.3.4 Electromagnetics field of PD

The application of high frequency antenna and UHF sensors for PD measurement is a challenging method that required good information about the electromagnetic fields radiated by PD activities. Generally, the electromagnetic field around a radiative electromagnetic source is divided into the near-field and far-field regions. Figure 2.14 shows the graphical view of the radiated electromagnetic near-field and far-field waves. The boundary between these two regions is determined by the wavelength (λ) of the radiating source. According to [42], the far-field region

includes the normal electric or magnetic fields with electric dipole characteristics, and the ratio of electric and magnetic fields intensities are constant. Perversely, the near field consists of multipole type fields, where the intensities of electric and magnetic fields change independently of each other and make the measurement in that regions more complicated.

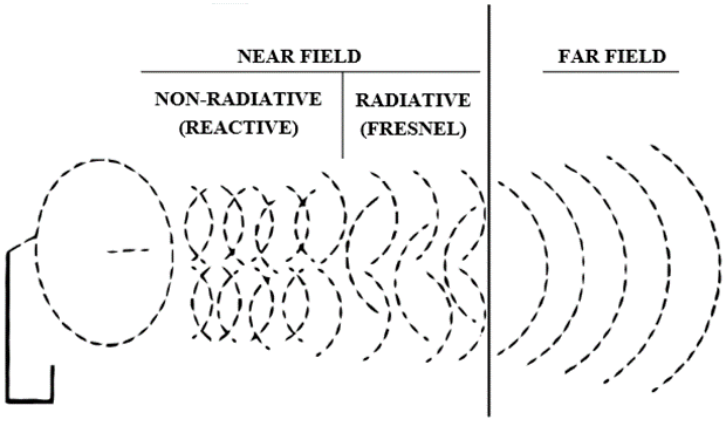

Figure 2.14 Electromagnetic radiation fields around the electromagnetic radiative source [42].

The electromagnetic fields radiated by PD pulses are originated by the transition of electrons within PD sources. Their frequency characteristics vary by the speed of electrons, recovery processes, and interruptions in discharge currents [20]. Thus, each type of PD shows different forms of electromagnetic fields due to differences in discharge mechanisms. Application of UHF sensors in GIS has shown high-order propagation modes of TEM waves that are related to their coaxial geometries [32], [39]. The electromagnetic fields emitted by PD discharge are represented as a Gaussian impulse and investigated using a finite difference time domain (FDTD) method in [43]. The results of the simulation in epoxy resin and ceramic are shown in Figure 2.15. According to this figure, the PD electromagnetic fields propagations during the first time steps (TS) (300th and 600th TS) is nondiffractive (for short distances of propagation), and for more

simulation time (900th, 1200th, and 1500 TS), it would be diffractive (for long distances). This phenomenon refers to the characteristics of near field regions in which electric field and magnetic fields influence each other. Also, the created electromagnetic fields within the varying dielectric materials are different. For example, the Gaussian source propagates as dipoles within the epoxy resin and as quadrupoles sequences in ceramics.

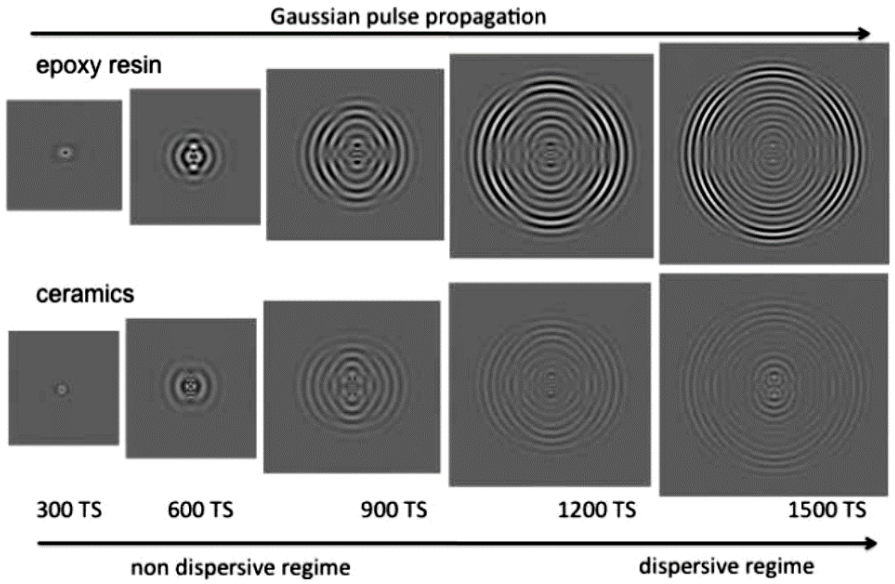

Figure 2.15 The electromagnetic field radiation of PD discharge (Gaussian pulse) around the epoxy resin and ceramic structures [43]

2.4 Partial Discharge Interpretation in DC

2.4.1 Individual Partial Discharge Waveshape

Two presented PD models in section 2.2 provide useful information about the discharge mechanisms of PDs. Understanding PD mechanisms can be useful for interpreting and distinguishing various types of PDs. In other words, the comprehensive PD patterns and providing the fingerprints for the PD phenomenon require the accurate measurement of PD waveshapes.

However, the discharge mechanism of a PD would be extracted from the characteristics of a PD induced current waveshapes in both time and frequency domains.

For PD in AC, some characterize observed waveforms as a double exponential, but the representativeness of such a model for all types of PD is questionable. Some recorded waveforms include rise times in the hundreds of picoseconds with pulse widths extending into tens of nanoseconds [44], [45]; other reports more Gaussian responses with rising times of approximately 100 ns and pulse width of 200 ns [29]. Frequencies have been reported in the 1-30 MHz range [40]. Figure 2.16 depicts a generic PD pulse waveform. The corresponding PD waveform is characterized by parameters such as amplitude, rise time (t_r), decay time (t_d), and pulse width ($t_{20\%}$).

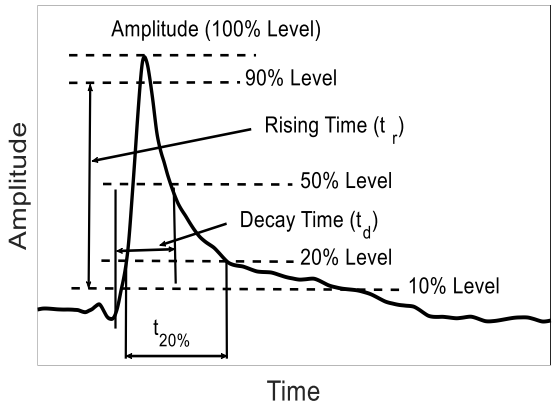

Figure 2.16 Typical PD waveform and characterization of its timing parameters.

The corresponding timing parameters of individual PD pulses are defined as follows in [6]. The amplitude refers to the difference between 0% and 100% (peak) levels of PD waveforms, which determines the intensity of the discharges. Rise time t_r is the time interval between the 10% and 90% amplitude levels of each pulse, which varies for different types of PDs and variations in the initiation of discharge channel growth. Decay time t_d is an interval between the origin

(approximately zero levels) and 50% of PD waveform tail, which relates to the type of PD and the end of the electron generation process through the discharge channel. In addition, $t_{20\%}$ is the period between 20% levels of PD waveforms, which has various values regarding the types of PDs and the positive ion velocities passing across the discharge channel.

The same type of PD discharge (cavity/surface/etc.) can look different depending on the utilized measuring circuit, sensor, and acquisition unit (i.e., transfer function). Moreover, significant differences are expected among measured PD pulses in the field with ideal waveshapes captured in the laboratory due to uncontrollable interference and the traveling wave phenomenon (attenuation and distortions as signals propagate from an unknown remote fault site to a sensor).

Although DC PD pulse analysis has been a rare research topic, in recent years, researchers have increasingly reported their studies on individual PD waveforms under DC stresses [8], [24], [25], [46]–[48]. Their findings show that DC PD pulses consist of double exponential functions and that their temporal characteristics are similar to those of AC PD pulses. The findings indicate that individual DC PD pulses were measured accurately via properly designed high-frequency measuring circuits and sensors with sufficiently large bandwidth. The results of captured waveshapes of PD under DC stress using the high bandwidth measuring circuit for corona discharge in air and oil as well as surface discharge in the air were compared by Kluteter *et al.* [24], [25], [47], [49], [50] (Figure 2.17). The results of the statistical analysis on the rise time, fall time, and amplitude parameters in that work demonstrated a low standard deviation among 1000 sequent pulses. As evident in Fig 2.16, the influence of insulating media is apparent for corona discharge in air and oil, where the pulse width is wider for corona in the air compared to oil. Also, both corona in air and oil accompanied by fast rise time pulses. In addition, the waveshape of

surface discharge represents a waveshape with a fast rise and decay time. The results from Figure 2.17 confirm the necessities of various PDs waveshapes analysis in DC.

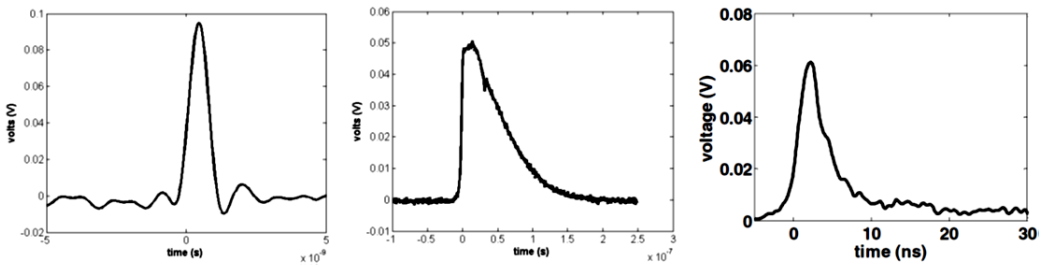

Corona in Oil Corona in Air Surface discharge

Figure 2.17 Corona and surface PD waveshapes under the DC stress [24].

2.4.2 Time-Resolved Partial Discharge (TRPD)

Investigation of the PD pulse waveshapes results in establishing patterns and fingerprints, which could help for better interpretation and monitoring of the PD phenomenon. As we know, the PRPD techniques are well established for AC-voltage. Fundamental quantities such as the instantaneous value of test voltage, phase angle, apparent charge, and several discharges (pulse count) are recorded and evaluated to derive quantities (distributions and statistical operators) used for pattern recognition, fingerprinting, and defect identification [23]. However, such approaches are inapplicable to DC voltages, where similar time-varying metrics are unattainable. There is no generally accepted method for the determination of PD quantities for tests with DC-voltage. Under DC-voltage stress, discharge pulse repetition rate can vary slowly (defined by relaxation times for solid insulation; displacement of liquid insulation also impacts relaxation time constants). Also, the discharge may occur during voltage change or polarity reversal but decrease under steady-state conditions, and test voltage ripple (dependent on the source and circuit) may influence PD characteristics [28]. However, the results of the relationship between PD characteristics and time

parameters and some initiative patterns for a different type of PD at DC were proposed in [51], [52]. These TRPD patterns are majorly dependent on the repetition rate and timing characteristics of individual PD pulses, such as rise time, decay time, and pulse width. In other words, TRPD interpretations commonly include various methods of analysis according to the individual PD pulse characteristics versus their time of occurrences, the correlation among the succeeding and preceding pulses, and the repetition rate of PDs [2], [6].

Moreover, TRPD methods mostly use the statistical analysis of the individual PD pulses in quantifying their waveform characteristics and trends to find meaningful patterns. There are a variety of TRPD methods used in the interpretation of various types of PDs. For instance, some of these methods focus on the PD repetition rates to find trends related to the stress changes and some pulses, while some concentrate on the corresponding PD pulse characteristics (*e.g.,* rise and decay times) trends [6]–[8]. Figure 2.18 provides comprehensive information about some consecutive PD signals recorded under DC. This figure concludes all the required information for the preparation of TRPD patterns. The variation of corresponding PD pulse regarding its successor and predecessor pulses would provide useful information that leads to the classification of PD data.

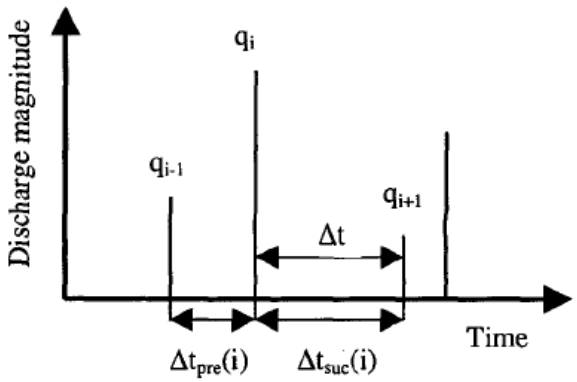

Figure 2.18 Discharge magnitude versus successor and predecessor time intervals [51]

Indeed, the time intervals between PD occurrences and their characteristics depend on the discharge mechanisms of PD defects. Therefore, because of existing differences between the various types of PDs, the parameters such as amplitude, time characteristics, and repetition rates can be distinguished significantly. Figure 2.19 shows examples of TRPD patterns.

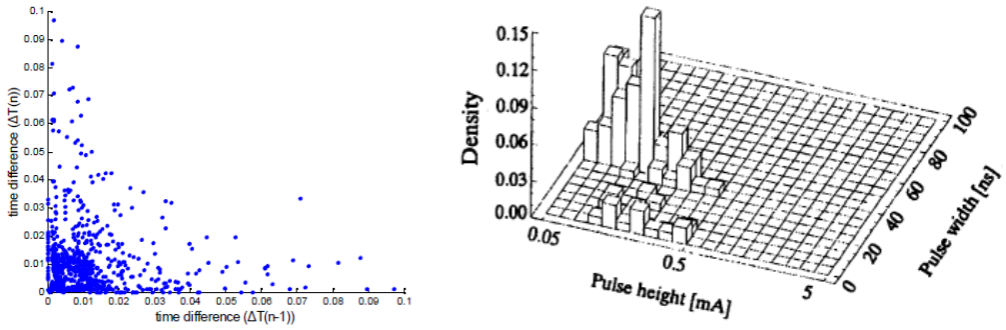

(a) (b)

Figure 2.19 The examples of TRPD patterns at DC voltage. (a) Scattering plot of successor and predecessor time interval for a cavity discharge [3], (b) 3D pattern of discharge density versus its amplitude and pulse width in a cavity discharge [19].

As shown in Figure 2.19, plotting the extracted data from Figure 2.18 provides meaningful information about the corresponding PD defects, which results to the clustering of PD data. For example, Figure 2.19a represents the repetition rate information for a cavity discharge measurement in DC. The figure shows that there is a short interval among successor and predecessor discharges. Similarly, Figure 2.19b presents most PD data in that research had a low amplitude with short pulse widths. Therefore, the useful information would be extracted through the correlation among the PD waveshape characteristics and their time intervals under DC application. However, finding the meaningful TRPD patterns require obtaining some PD data and finding a correlation between their parameters.

2.4.3 Frequency Domain classification of Partial Discharge

IEC60270 includes a short section related to ultra-wideband instruments for measuring and quantifying the shape or frequency spectrum of PD current or voltage pulses, but does not provide recommendations for the determination of PD quantities. Since quantification of apparent charge of the PD current pulses is limited to specific scenarios and validity ranges – an observation may be only applicable to a certain condition, device or material, or discharge form and deviate significantly for an alternate scenario. However, Sarathi and Koperundevi [53] used the frequency domain spectrum of floating particles PD pulse measured by UHF techniques to examine PD activities within the DC transformer oil. The results showed the effectiveness of broadband measurement techniques on detecting partial discharge through the PD pulse analysis. An example of the measured signal in both time and frequency domains is provided in Figure 2.20. As seen, the frequency domain waveform includes more useful information than the time-domain for analysis of corresponding PD defects.

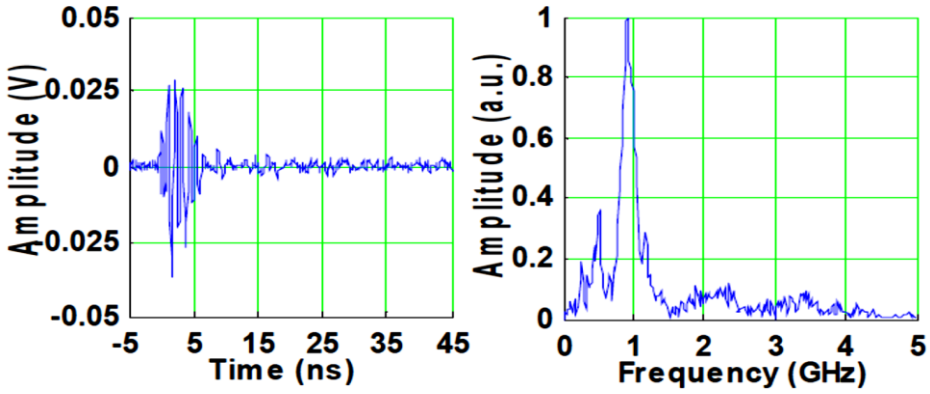

Figure 2.20 Example of floating particle PD waveshape measured by the UHF sensor in time and frequency domains [53].

CHAPTER III

RESEARCH OBJECTIVES

Accurate PD measurements are integral for the condition assessment and health monitoring of medium- and high-voltage DC applications. However, the accurate measurement and interpretation of PDs under DC stresses are more challenging than those of AC PDs accompanied by phase-resolved information. The PRPD analysis techniques are widely used for establishing patterns of various types of PDs (e.g., corona, cavity, and surface discharges) in AC systems. Advantages provided by PRPD, such as convenient PD interpretation and noise rejection, are not available in analyzing DC PDs. Therefore, utilizing individual PD pulse characteristics with respect to time, also known as TRPD, is the only option for PD interpretation under DC stresses. Despite the discussed difficulties and obstacles in measuring PD under DC voltage stresses, this dissertation presents the accurate methodologies for measuring individual PD pulses.

The primary objectives of this dissertation are:

- To investigate the feasibility of utilizing the conventional PD sensors and electromagnetic field sensors for capturing PD pulses (chapter IV).
- To present the design requirements of a testbed equipped with a high bandwidth transmission line for the measurement of individual PD pulses (chapter V).

- To specify and design suitable electromagnetic field sensors (D-dot and B-dot) to capture individual PD pulses (chapter VI).
- To compare, quantify, and classify the AC and DC induced PD pulses (chapters VII and VIII)

The outline of the succeeding chapters is listed below.

- Chapter IV investigates the utilization of conventional and commercial electromagnetic sensors for transient discharge measurement.
- Chapter V describes the design, simulation, and construction of an individual PD pulse measurement testbed and transmission line.
- Chapter VI explains the electromagnetic field D-dot and B-dot sensors.
- Chapter VII presents the case studies (PD sources), the individual partial discharge waveshapes captured by D-dot, B-dot, 50 Ω resistance, and various PD mechanisms.
- Chapter VIII represents a quantitative analysis of individual partial discharge pulses captured by the sensors, under both AC and DC stresses.
- Chapter IX draws the broad conclusions of the dissertation.
- Chapter X discusses the future outlook of this research and potential topics.
- Chapter XI lists all journal and conference papers published by the author.

CHAPTER IV

UTILIZATION OF CONVENTIONAL AND COMMERCIAL ELECTROMAGNETIC SENSORS FOR TRANSIENT DISCHARGE MEASUREMENT

4.1 Motivation

As discussed in Chapter II, various types of conventional and non-conventional sensors are used by researchers to measure PD activities. However, applying a typical sensor for measuring PD activities does not guarantee the performance of that sensor for capturing the individual PD pulses. In this chapter, a set of conventional and electromagnetic field sensors (with EMC applications) are examined to measure the radiated signals and induced current by electrical transient discharges and PD. The goal of this experiment is to understand the feasibility of these sensors for individual PD measurement and to find individual PD test circuit requirements. The results of this investigation help us to organize the simulation, design, and manufacturing of DC PD measurement circuit. To achieve these goals, first, we shortly introduce the prepared sensors, which are a combination of homemade and commercial sensors commonly used for high voltage testing purposes. Second, as the sensors have different operational principles and responses (based on either conduction, induction, or radiation), efforts are needed to ensure they are reacting to the same event – i.e., the observed response is a result of the discharge, not the measurement setup or external influence. The first experimental scenario outputs a single disruptive discharge (flashover)

pulse using a Van de Graaff generator (height = 75 cm, diameter = 25 cm), after which the sensors are assessed for their primary function (observing PD). Sensor sensitivity is also compared by detecting small traveling waves along a conductor using a PD calibrator as a source. Two 4-channel digitizers were used for data acquisition. The faster (electromagnetic) sensors were connected to a LECROY WaveMaster 806Zi-B (6 GHz, 40 GS/s) using 18 GHz Huber+Suhner Sucoflex 106 measurement cables. The other sensors were connected to a Tektronix DPO7104 (1 GHz, 20 GS/s) oscilloscope using RG58 coaxial cables.

4.2 Selection of Sensors

- Shunt Resistor

Figure 4.1 denotes a 50 Ω shunt resistor comprised of six 300 Ω metal-film resistors that are coaxially paralleled. The 50 Ω shunt resistor provides a matched impedance for measuring PD current though the connection cable and input resistance of the digitizer.

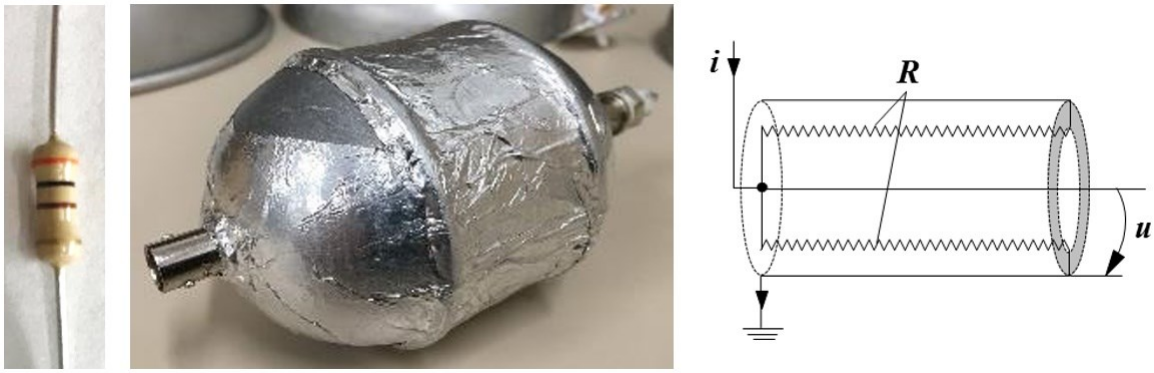

Figure 4.1 The 50 Ω shunt resistor is made by six paralleled 300 Ω metal-film resistors.

- Current Transformer

Two commercial non-clamp HFCTs – the Pearson 110A (0.1 V/A, 20 ns rise time, 1 Hz – 20 MHz) and Power Diagnostix CT1 (0.1 V/A, 0.5 – 80 MHz). Figure 4.2 shows a picture of the two sensors.

Figure 4.2 Pearson 110A and Power Diagnostix CT1 HFCTs.

- Loop Antenna

Two types of loop antennas used in this research are presented in Figure 4.3. The sensor in Figure 4.3a is the Beehive Electronics 100C model loop probe (diameter r = 22 mm, the cut-off frequency at 50 MHz). The sensor in Figure 4.3b is a loop antenna constructed by passing a single closed loop (r = 65 mm) through a Power Diagnostix high frequency current transformer.

(a) (b)

Figure 4.3 Loop antenna sensors. (a) Beehive Electronics model 100C, (b) HFCT loop.

- Monopole Antenna

The electric field sensors (short monopoles) used in this research were constructed from SMA connectors (18 GHz, 50 Ω, r = 1.275 mm beryllium copper center conductor, extending 15.9 mm past the ground plane, Figure 4.4).

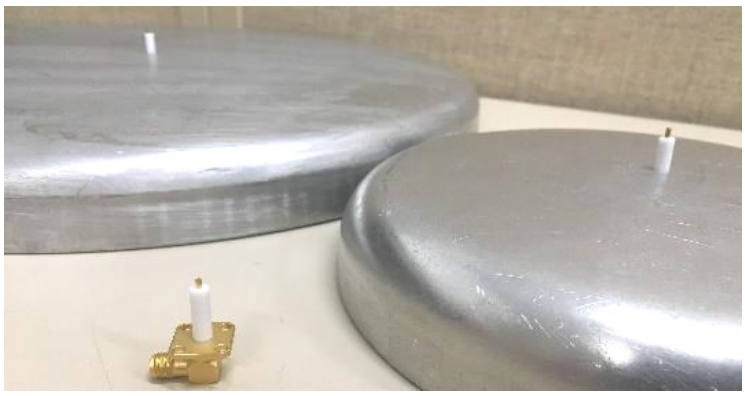

Figure 4.4 Monopole antennas on varying ground planes constructed from SMA connectors.

4.3 Disruptive Discharge

4.2.1 Monopole Antenna Position Tests

In this test, the spark discharge generated by the Van der Graff generator was examined. 12 locations are selected around the Van de Graff generator to find the best place for mounting the monopole antenna. Figure 4.5 shows the layout of Van de Graff and the positions of the sensors. The sensors at positions 1 and 2 directly measured the airborne radiations behind of ground and source conductors, and the sensors at positions 3 and 4 straightly measured the propagated signals from the discharge (Figure 4.5).

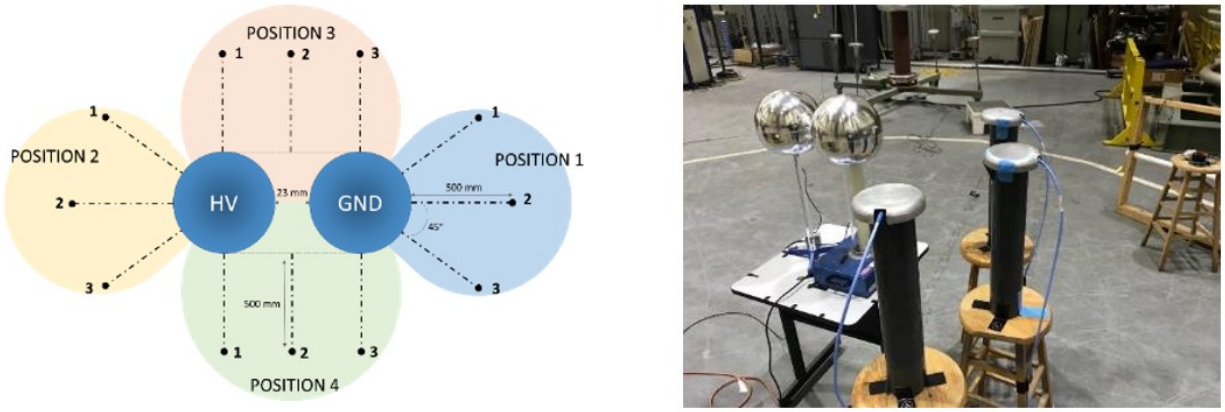

Figure 4.5 Placement of monopole antenna around Van de Graaff generator to establish approximate radiation pattern.

According to Figure 4.6, position 2 produced the most consistent waveforms in all sensors within this zone (in terms of amplitude, rise time, and pulse width of first major oscillation) compared to the HFCT signal.

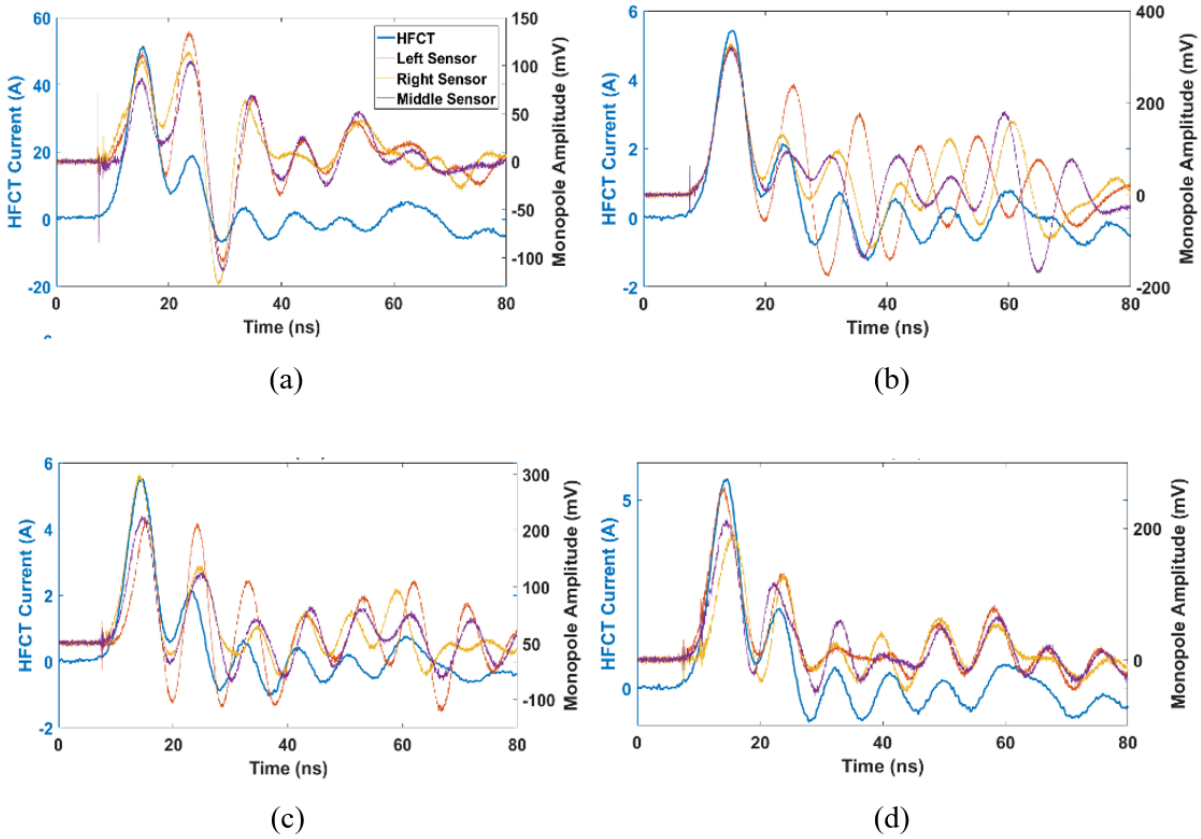

Figure 4.6 Comparison between monopole antennas and HFCT. (a) Position 1, (b) Position 2, (c) Position 3, (d) Position 4.

Naturally, Position 1 results in the most inconsistent waveform as it is situated behind the grounded sphere conductor (the HV conductor is the main radiator). The results show that the amplitude and waveform of the HFCT sensor are in better agreement in all positions, and thus, the measured discharges for all the positions can be assumed identical. Due to the characteristics of HFCT, which directly measures the discharge current, its response can be considered a good reference for describing the discharge phenomenon between source and ground conductors. Therefore, the places where the monopole antenna showed the closest responses to that of HFCT would be the best locations. Figure 4.6a illustrates the responses of the monopole around the

ground conductor (position 1 in Figure 4.5), which are not similar to the waveform of HFCT. It seems the ground conductor worked as a barrier and blocked the airborne radiations of discharge between the conductors.

Moreover, by comparing the amplitude of the monopole sensors in Figure 4.6a, it is clear that the left and right sides measured higher amplitude signals concerning the middle one, which proves the barrier property of the ground conductor. By changing the position of monopole antenna sensors and bring them closer to the discharge place and the source conductor, it is obvious that the responses of those sensors are more similar to HFCT (Figure 4.6b to 4.6d). Furthermore, the highest amplitude responses were measured when the sensors were near the source conductor, which is the radiating source (Figure 4.6b), and identify the best place for mounting the sensors to measure full breakdown in air. Additionally, there is an interesting distortion rightly before the first peak in the responses of all monopole antenna sensors, which do not observe on HFCT response. This should be related to the formation of discharge channels between source and ground conductors. Thus, it can be concluded the response of the monopole antenna to the discharge phenomenon is faster than HFCT, and based on Figure 4.6, the best place for observing the full discharge and pre-discharge (discharge channel formation) phenomenon is close to the HV source.

4.2.2 Effect of Distance and Ground Plate on Monopole Antenna Responses

In this part, after finding the best place for mounting the monopole antenna sensors (behind the HV source), the effects of distance from the source conductor and size of the ground plate on the performance of monopole antenna sensors would be investigated (Figure 4.7).

Figure 4.7 Location of samples with different sizes of ground plates around the HV source.

Figure 4.8 shows the response of the sensor for 25, 50, 100, and 150 cm far away from the source conductor. As shown, the sensitivity of the sensor is a function of distance from the discharge place; by increasing the distance, the amplitude of response dropped by five times, and wave shape was significantly destroyed for distances more than 50 cm.

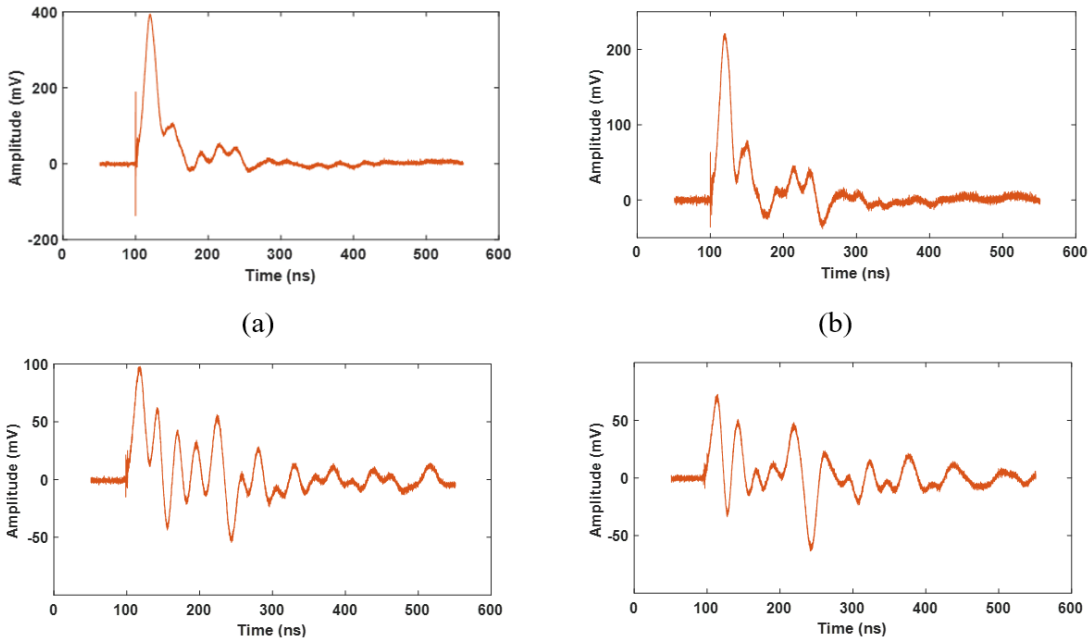

Figure 4.8 The responses of monopole antenna respect to distances from HV source. (a) 25 cm, (b) 50 cm, (c) 100 cm, (d) 150 cm.

The ground plate affects the sensitivity of monopole antenna sensors and significantly improves it. Three different diameters flat ground plates are provided to find the right side of the ground plate in our research. Also, their performance is shown in Figure 4.9 for various distances from the HV source.

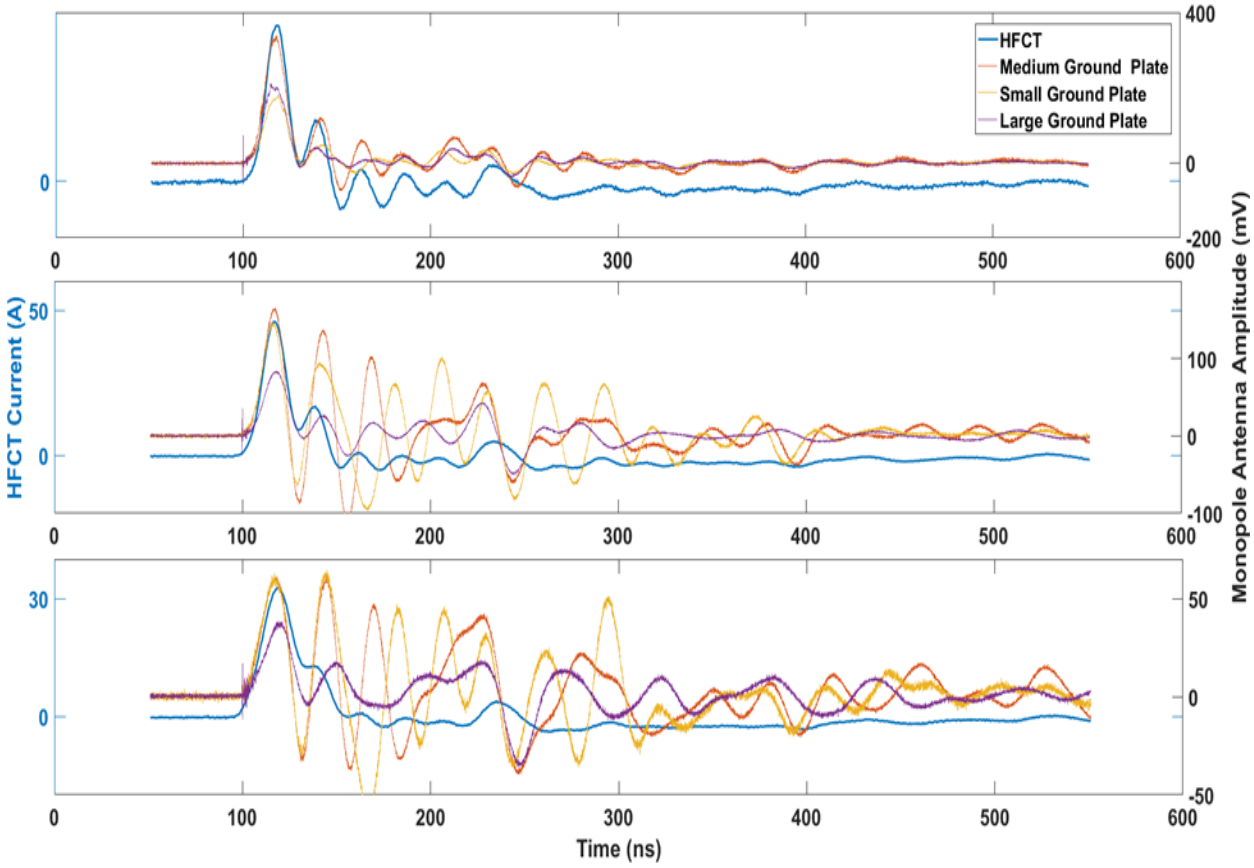

Figure 4.9 Responses of monopole antenna with different size ground plates for different distances, 50 cm (top), 100 cm (middle), and 150 cm (bottom), from HV source.

Due to Figure 4.9, for 50 cm far from the source conductor, the wave shapes of all sensors are the same as that of HFCT, but the sensor with medium size ground plate has the stronger peak than the rest. Although by increasing the distance, the sensor with medium and small size ground

plates have more sensitivity than the large one, their wave shapes are destroyed and not more similar to that of larger ones and HFCT. Therefore, using the monopole antenna with larger ground plates promote the application of sensors for further distances.

4.2.3 Loop Antenna (Inductive Sensor) Position Tests

The other type of wireless sensors used for measuring the full discharge between the source and ground conductors is a loop antenna. For finding the best place for mounting the loop antenna sensors, two types of them were chosen for performing this test. Two scenarios were assumed to find the performance of sensors around the discharge place and the discharge current lead.

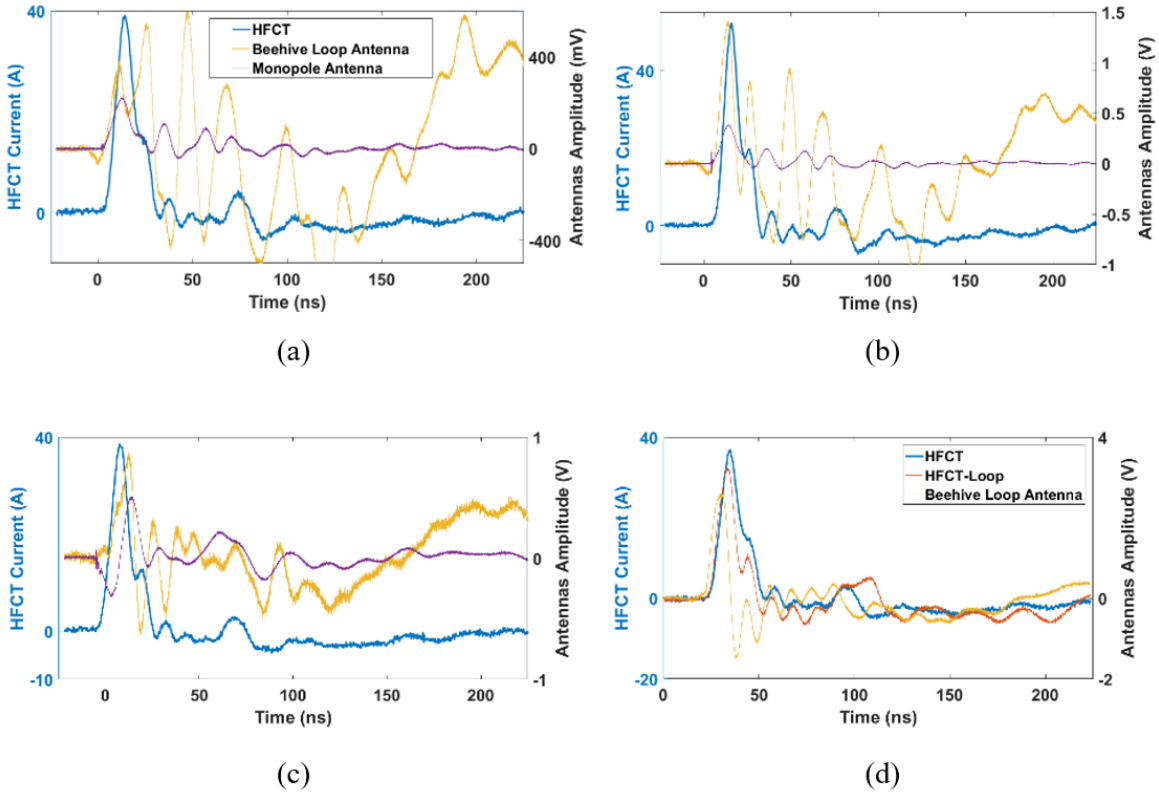

Figure 4.10 Comparison of Loop antenna sensors response at different places. (a) Around the discharge place, (b) behind the HV source, (c) 5 cm on top of the ground lead, (d) less than 1 cm on top of the ground lead.

Figure 4.10 illustrates the application of loop antenna for measuring the discharge between source and ground conductors. It is clear in Figure 4.10a to 4.10c that changing of sensors locations around the discharge place have no significant effects on the measurement of discharge phenomenon, but placing the sensors around the ground connection, where the strength of magnetic fields is high, their responses became fairly similar to that of HFCT (Figure 4.10d). Therefore, it can be concluded that the magnetic field around the discharge place is not as much as loop antenna sensors to capture it, but it is strong enough to be measured by loop antennas around ground connections. Moreover, the responses of the loop antenna in Figure 4.10d show that the sensitivity of the HFCT-loop is more than the Yellow Loop antenna because of its bigger diameter.

4.4 Anechoic Chamber Tests

Repeating the previous measurements inside the Anechoic chamber allowed uss to compare the monopole antennas, loop antennas, HFCTs, and shunt resistor without significant external distortions. Two monopole antennas were used – one with a flat ground plane (r = 180 mm) and another with a similar diameter spherical ground plane. Also, a measurement was performed in an anechoic chamber (Figure 4.11) to minimize reflection during the tests.

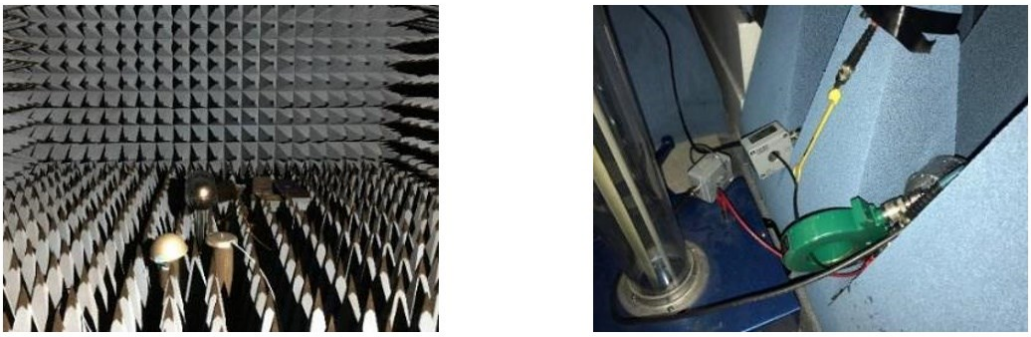

Figure 4.11 Van de Graaff generator and sensors inside the anechoic chamber.

As evident from Figure 4.11, all sensors respond to the discharge source in some manner. The antennas (monopole and loop), responding to airborne electromagnetic radiation, clearly have a faster response (shorter rise time and pulse width). The yellow Loop antenna exhibits a transient oscillation with both positive and negative peaks (typical to narrowband instruments, as explained earlier). The monopoles produce a distinguishable main surge followed by smaller oscillation, while the current transformers (HFCT and Pearson) observe almost identical damped single oscillation with a different polarity. The shunt produced similar trends to the HFCT, but slightly faster and (right/positive) skewed main oscillation. The HFCT loop sensor produced unreasonable oscillations. The investigated scenario is idealistic – quite distant from a typical high voltage (high interference) environment. Furthermore, the signals emitted from disruptive discharge are considerably greater than those produced by PD. A more representative input signal must be used to assess the suitability of the investigated sensors for PD applications.

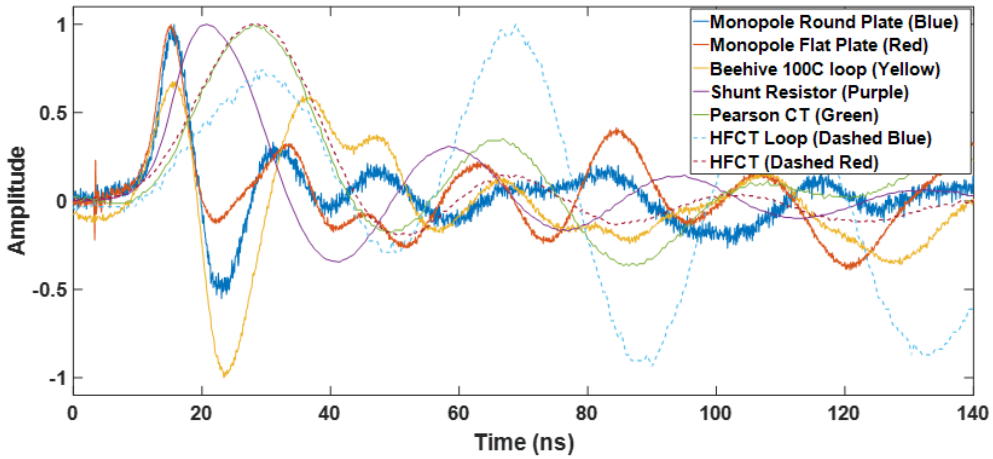

Figure 4.12 The response of all investigated sensors to discharge measured inside the anechoic chamber (amplitude normalized for improved visualization of waveforms).

4.5 AC Partial Discharge Waveshape Measurement

It is common to simulate the different types of PD on a laboratory scale through the sandwich samples. Therefore, in this thesis, two forms of PD were investigated – corona and cavity discharge (Figure 4.13). Shunt resistor and current transformers were placed on the ground connection of the sample while the distance of the monopole antennas was varied for optimal response. The loop antenna was placed in the proximity of the sample ground wire.

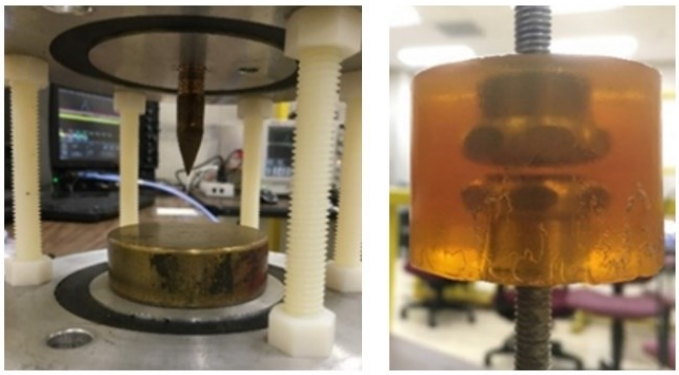

Figure 4.13 Left – corona source using rod-plane conductor configuration; right – cavity discharge using void inside epoxy resin sample.

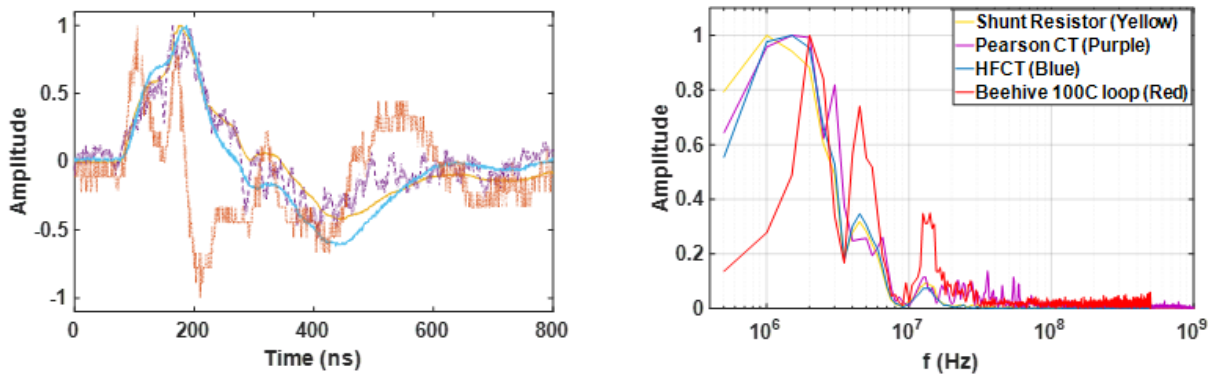

(a)

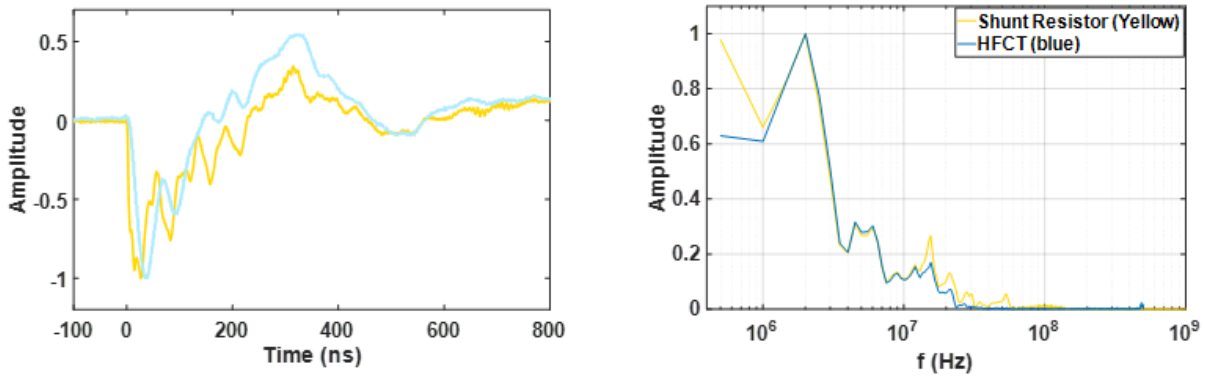

(b)

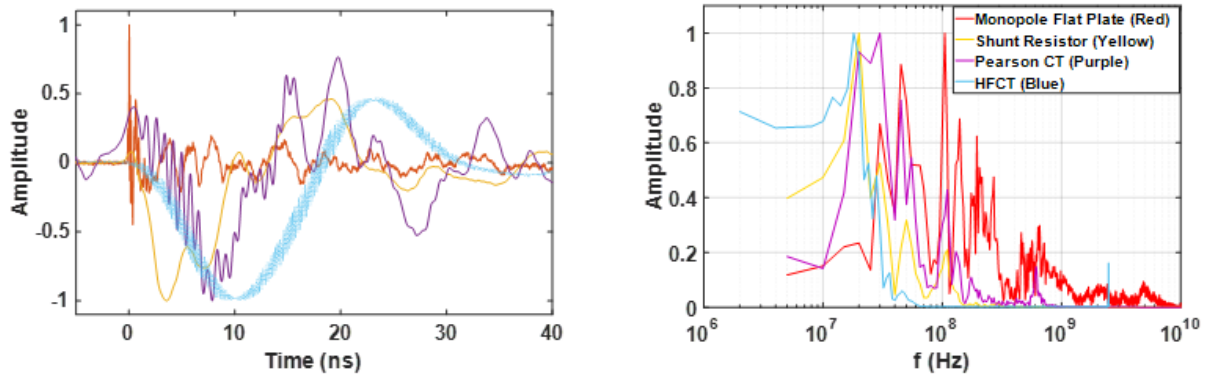

(c)

Figure 4.14 Measured partial discharge waveforms – time domain on the left side, and frequency domain on the right side. (a) positive streamer (corona) discharge, (b) Trichel pulses, and (c) cavity discharge

For corona discharge, only the shunt resistor, Pearson CT, HFCT, and loop antenna observing current in the ground path were able to detect strong positive streamers (2.3 nC). The loop antenna and Pearson had poor signal quality (low SNR), as evident in Figure 4.14a. However, the shunt and HFCT detected small Trichel pulses upon the onset of corona discharge (Figure 4.14b). For the monopole antenna to detect a signal, it had to be brought into such proximity that corona was igniting directly at the tip of the probe conductor and risking flashover. Internal cavity discharge within the resin sample produced relatively large PD signals (12 nC). This discharge was detected by the monopole antenna (20 cm from the source), but as a very different waveform, as evident in Figure 4.14c. Such differences are expected, considering that the airborne electromagnetic wave first needs to propagate through the resin insulation into the surrounding air, while other conducting circuit leads also radiate signals.

4.6 Traveling Wave Measurement

It is clear that PD events are highly varying and dependent on a vast multitude of factors, thus making it difficult to compare sensors responding to a different stimulus (radiative vs. conductive/inductive). To reduce the number of variables and yet again simplify the assessment of sensor performance, the focus was shifted away from the PD phenomenon itself and directed toward a simpler single excitation of comparable magnitude and speed to PD. A PD calibrator ("Reference Pulse (Black), 10-90% rise time = 3 ns, 50% pulse width = 6 ns, in Figure 10) was connected to a length of bare copper wire and set to output 1 nC. The different sensors were aligned along the wire to observe the traveling signal (resulting magnetic and electric fields). The

monopole antennas were unable to detect any signal. However, both loop antennas presented exhibit responses to the calibrator pulse.

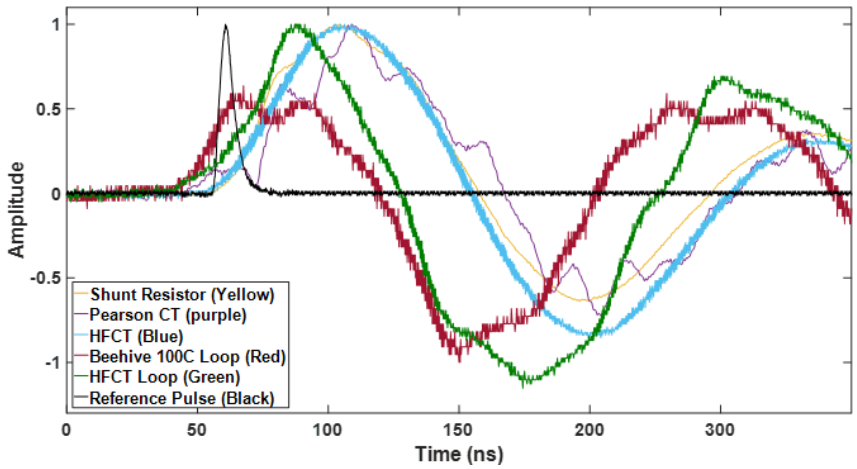

Figure 4.15 The response of sensors to propagating PD calibrator pulse along the conductor.

4.7 DC Partial Discharge Waveshape Measurement

The DC test setup was prepared by using the Haefely multi-test system (MTS) through rectifying the HVAC transformer by two diodes and charging a 200 kV, 15 nF capacitor, which is shown in Figure 4.16. As can be seen, two types of sensors, shunt resistor (conventional) and HFCT (nonconventional), were mounted in the measuring system to capture the charge displacement through the ground lead.

(a) (b)

Figure 4.16 Experimental PD test under DC stress. (a) Test setup, (b) Corona test sample.

Also, Figure 4.17 shows the measured positive corona pulse shape, which is compared by that of AC in both time and frequency domains. According to the figure, the DC corona pulse has a faster rise-time than AC, which is proven by both shunt and HFCT sensors. Moreover, the pulse width of corona pulses at DC is smaller than that of AC. In contrast, there are no significant differences in the sensors' responses in frequency.

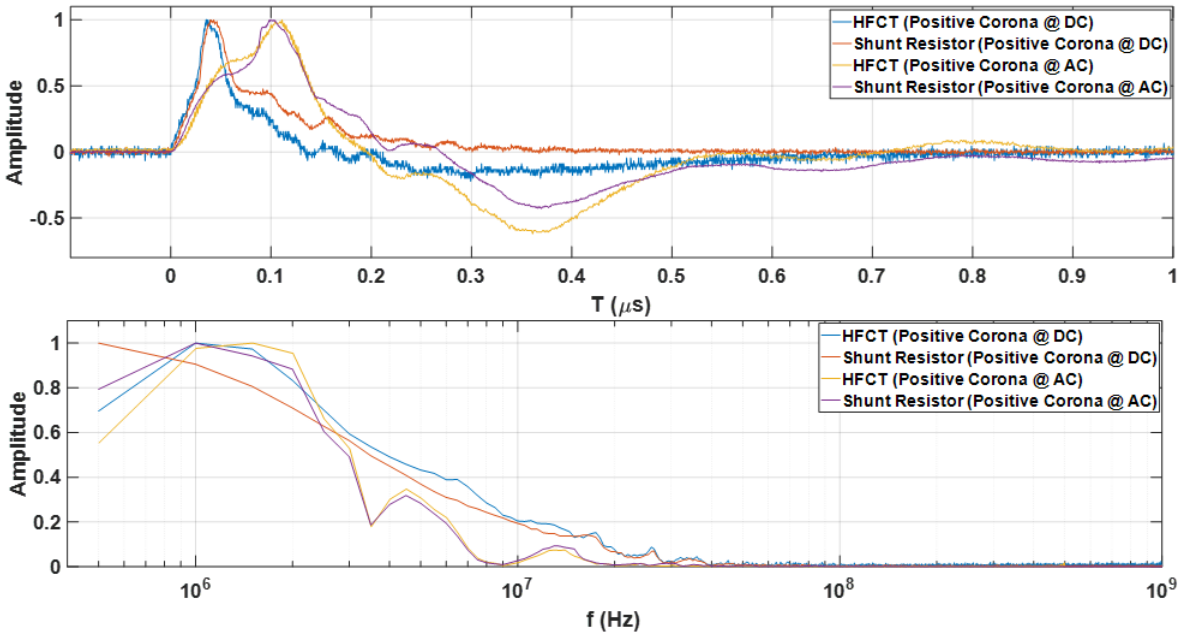

Figure 4.17 Comparison of AC and DC positive corona pulses in both time-domain (top) and frequency-domain (bottom) through conventional and nonconventional sensors.

4.8 Summary

This chapter dealt with utilizing some conventional PD sensors and high bandwidth EMC electromagnetic sensors to measure individual PD pulses. The obtained results explain:

- No meaningful information can be extracted by comparing the employed sensors because of the frequency response limitations or signal attenuations.
- It is difficult to measure PD pulses through any type of electromagnetic sensors; thus, specific consideration is required to utilize the electromagnetic field sensors for individual PD measurement.

Therefore, the mentioned challenges with applying non-conventional sensors are related to the subjects like their sensitivity and location issues, which should be improved for the precise measurement of PD waveshapes. Improving the sensitivity of sensors requires to design a better sensor and transmission line, which need more simulation and experimental activities.

CHAPTER V

DESIGN AND MANUFACTURING OF TESTBED AND TRANSMISSION LINE

5.1 Motivation

According to the information provided in Chapter III, PD measurement requires sensitive coupling devices and perfectly matched impedance measuring circuits, which includes an ideal transmission line and a high bandwidth data acquisition system. Furthermore, this Chapter aims to propose a method to design and develop a test setup with an ideal transmission line suitable for individual PD waveshape measurement through both the experimental and numerical methods. Indeed, the main goal of this Chapter is to integrate all test elements in a unique testbed, which follows the IEC standard 60270 criteria. Figure 5.1 shows the AC PD measurement circuit suggested by IEC standard 60270 [28].

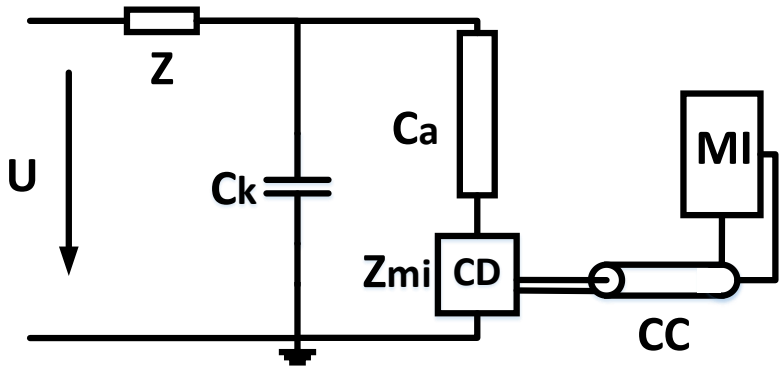

Figure 5.1 Schematic of the partial discharge measurement circuit

As it is seen, the PD measurement circuit includes an HV source (U), filter (Z), coupling capacitor (Ck), test object (Ca), coupling device (CD with input impedance Zmi), connecting cable (CC), and measuring instrument (MI). It should be mentioned that the application of filter in PD measurement is optional and usually is used to suppress background noises from the source side. In this work, since we are using a PD free HV source, we do not use any type of filter to improve background noise. However, the other elements, such as the coupling capacitor, PD source samples, transmission line, and sensors, should be designed.

5.2 Testbed Preparation

5.2.1 Design

Due to the lack of standards for DC PD measurement, recommended configuration of a high bandwidth testbed that measures individual PD pulses reported by Klueter et al. in [24] is used in this work. The testbed is shown in Figure 5.2. As shown in the figure, the testbed consists of a cap that connects to a high voltage supply. An insulating spacer separates the grounded shield from the energized top conductor. Also, an air-filled coupling capacitor between the HV cap and the shield conductor isolates the PD sources from external noise and disturbances (ground conductor). Besides, a matching 50 Ω conical transmission line (coaxial configuration) that terminates the PD source to an N-Type, which grounds the entire testbed through the oscilloscope. In addition, PD sources are mounted between the coupling capacitor and the center conductor of the conical transmission line. The coaxial symmetry of the testbed design simplifies simulation and machining.

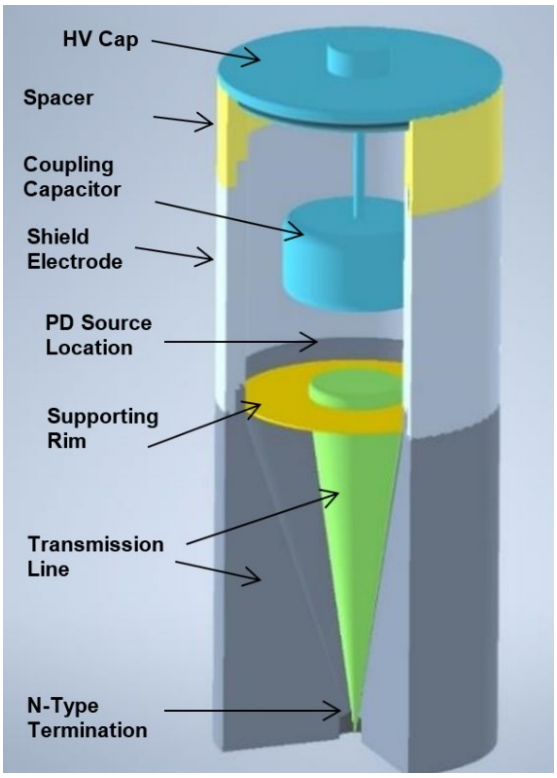

Figure 5.2 Cutaway view of the designed testbed for the investigation of individual PD.

To verify the performance of the testbed, we assume a case in which a needle is connected to the coupling capacitor facing the center conductor of the transmission line. Applying high voltage DC to the HV cap connected to the needle increases the electric field at the tip of the needle. As the voltage exceeds the required voltage of breakdown, after elapsing stochastic time lags (describe in [6]), corona PD occurs on the tip of the needle. Subsequently, the displacement of electrons in the gap between the needle tip and the center conductor of the transmission line flows current through the conical transmission line and received by the oscilloscope. Appropriate sensors measure the discharge current generated by PD.

5.2.2 Finite Element Analysis Simulation

For the accurate design of the testbed, all parts are simulated in COMSOL Multiphysics to finalize the dimensions. Through the simulation, required clearances are determined, and electric field distributions are analyzed to ensure corona-free conditions. Generally, COMSOL Multiphysics is commercial software that provides finite element analysis of various materials such as solids, liquid, and gases used for electrical, mechanical, chemical, etc. application. COMSOL widely uses in the field of high voltage engineering to simulate the electric field and voltage distributions across the insulating materials.

The testbed design simulation in this work was performed through the *Electrostatics* module of COMSOL software. Initially, two important limitations were considered through the design. First, the dimension limitation in manufacturing the testbed. The lathe machine manufactures all the testbed elements at the Electrical and Computer Engineering building. The lathe machine allows the machining of objects by 90mm diameter. Therefore, the dimension of the object affects the general size of testbed elements and their clearances. Second, the shape and clearance of testbed elements should be calculated somehow to avoid exceeding the electric field more than 3kV/mm. This electric field limitation is the breakdown field of atmospheric pressure air and should be considered to avoid corona discharge, specifically around sharp edges and discontinuities among different parts.

The 2D axisymmetric geometry of the designed testbed by considering the corresponding limitation is shown in Figure 5.3. As the electric field inside the conductive material (e.g., metals) is equal to zero, the COMSOL simulation only requires the drawing of conductive material boundaries with insulating media. In contrast, as the electric field within the insulating media is non-zero, then those media should draw as solid objects. Therefore, as it is illustrated in Figure

5.3, we just draw the metallic parts of our testbed with some lines which represent their boundaries. Consequently, the solid areas with gray color are the insulating media, which is filled mostly by air except for the blue color part that is an insulating spacer between the HV cap and shielding wall that is made by plastic.

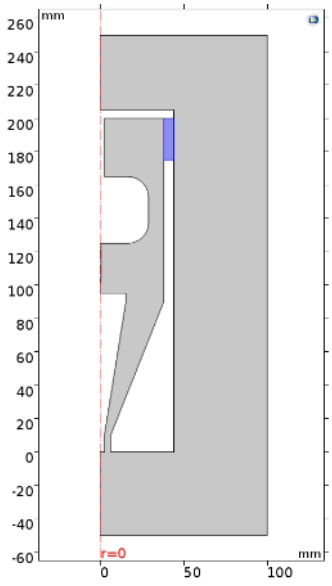

Figure 5.3 Sketch view of a designed testbed for measurement of partial discharge in COMSOL.

After finalizing the geometry of the testbed, the distribution of electric fields and voltage alongside the testbed were examined. Thus, we connected a needle at the bottom of the coupling capacitor, which works as a corona discharge source, and applied a 20 kV DC voltage to the HV cap and other connected element boundaries. The electric shielding wall and the outer conductor of the transmission line were assumed as a ground conductor. Also, the center conductor of the transmission line that will be grounded through the measuring cable and internal resistance of the oscilloscope was considered as a floating potential conductor. After that, the custom triangular

meshes with adjustable sizes between 0.05 and 1mm are selected for meshing the testbed. Consequently, the result of the simulation is provided in Figure 5.4.

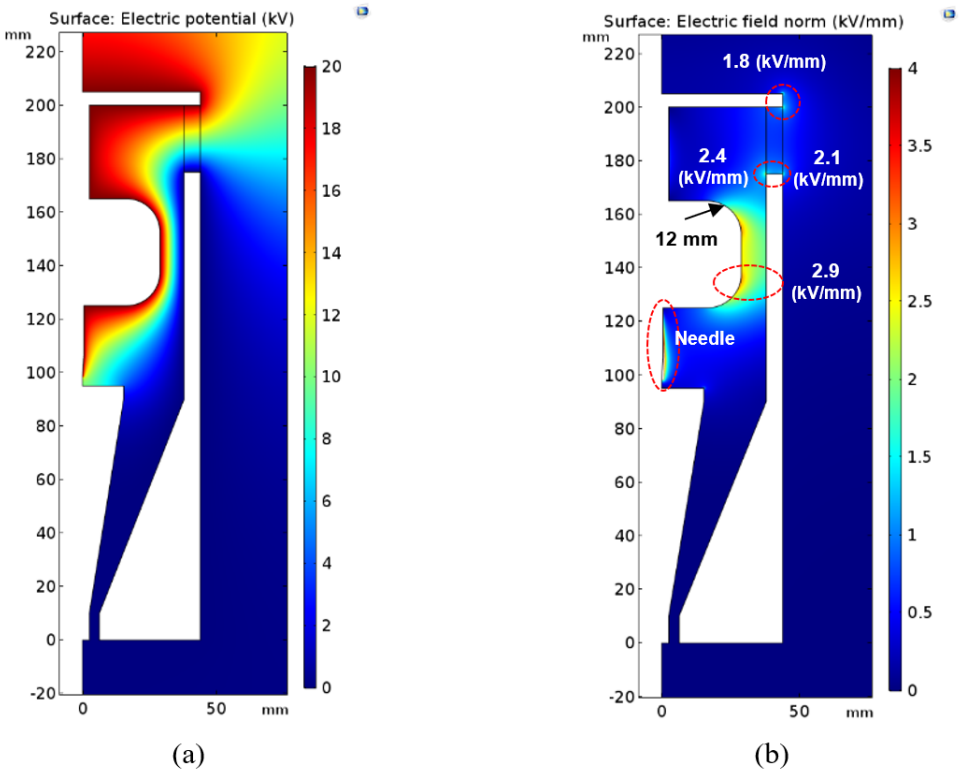

Figure 5.4 2D axisymmetric simulation of DC PD testbed. (a) Voltage distribution (kV), a) Electric field distribution (kV/mm),

According to the results, the applied voltage of 20 kV is evenly distributed, as shown in Figure 5.4a among the high voltage cap, coupling capacitor, and grounded shield conductors. As shown in Figure 5.4b, blue colors demonstrate the electric fields below 1 kV/mm. In addition, electric fields are strong around sharp edges, corners, and the interfaces among spacer and metal parts. Hence, the electric fields are reduced by applying larger radii on the edges to achieve values under 3 kV/mm. The highest electric field values of each part in the testbed are shown in Figure 5.4b at 20 kV.

5.2.3 Manufacturing of Testbed

All the metal parts of the designed testbed were manufactured by the lathe machine located at the Electrical and Computer Engineering department, and the insulating parts were manufactured by a 3D printer located at the same place. Figures 5.5 represent some photos that were taken during machining.

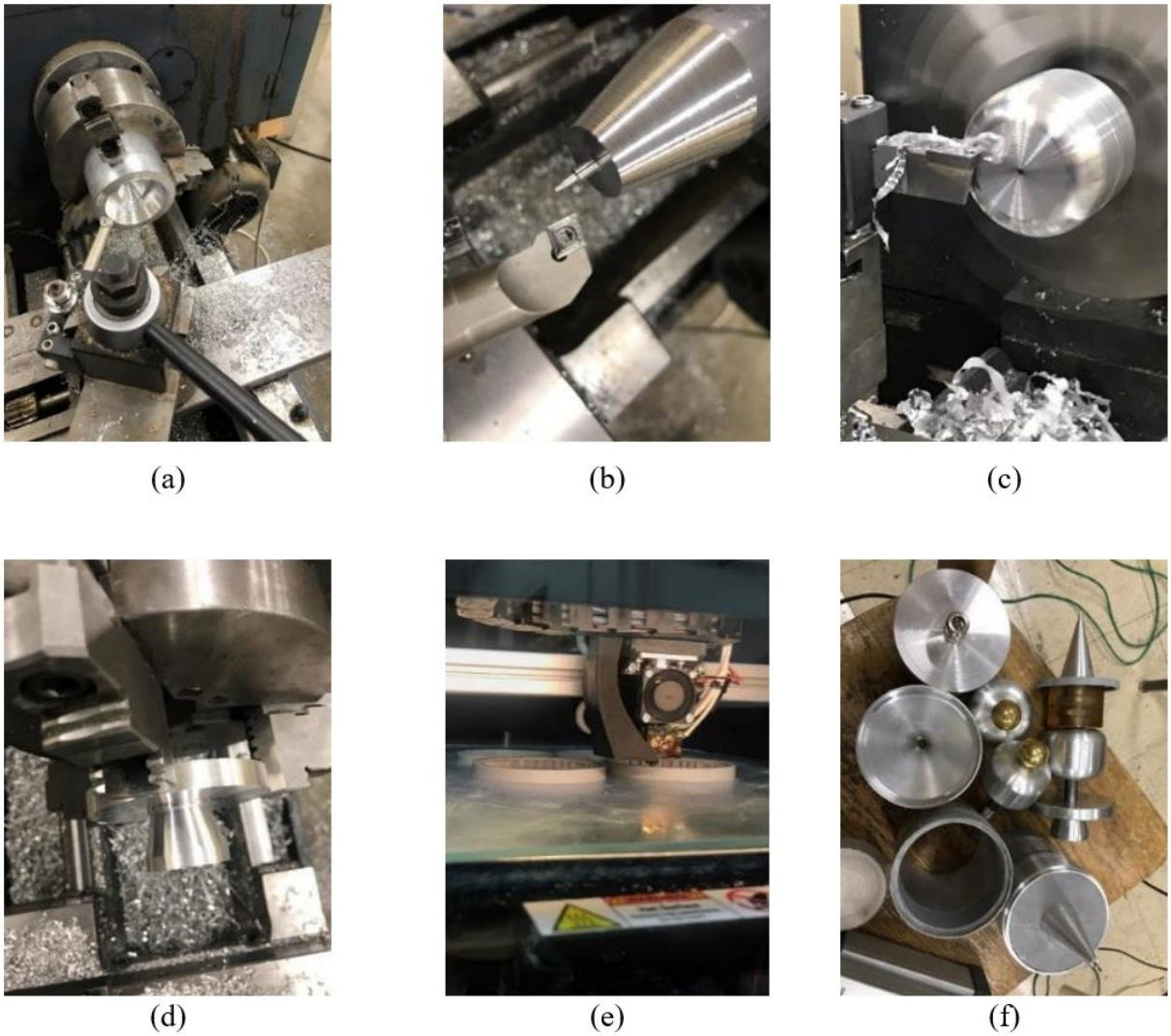

Figure 5.5 The preparation process of different parts of the testbed. a-b) Transmission line outer and inner conductors, (c) Coupling capacitor, (d) HV cap, (e) Supporting rim and insulation spacer, (f) Overall view of all prepared parts of the testbed.

Figure 5.5a and 5.5b demonstrate the outer and inner conductors of the transmission line with radiuses about 38mm and 15.5mm, respectively. The height of the transmission line is 80mm; the transmission line dimension will discuss with more details in the following paragraphs. Figure 5.5c represents the coupling capacitor with a 29mm radius, 30mm height, and 12mm radius of round edges. In addition, Figures 5.5d and 5.5e indicate HV cap and insulating parts, respectively. The radius of the HV cap is about 44mm, and its height is 30mm. The inner radius of the spacer, which isolates the HV cap from the grounding wall, is 38mm, and its thickness is 6mm. The inner and outer radiuses of the supporting rim are according to the transmission line conductors sizes. Moreover, Figure 5.5f shows the overall view of the prepared parts. As seen in this figure, the HV cap connects to the coupling capacitor through a coupler and PD sources bolts between the coupling capacitor and center conductor of the transmission line.

5.3 Transmission Line Preparation

Transmission lines are widely used in the measurement circuits of transient and high-frequency phenomena. Various transmission lines work as waveguiding structures that provide paths for signals to travel with minimal reflection and impedance mismatch. In individual PD pulse measurement, it is important to connect the PD source to a measurement device without external disturbances. A transmission line with impedance matched with all the measurement apparatus (e.g., connectors, coaxial cables) and a DAQ system is designed to ensure the noise-free condition.

5.3.1 Design [54]

There are different types of transmission line designs that are mostly used in radio frequency circuits. The most common type of transmission line uses widely everywhere is a

coaxial cable. As seen in Figure 5.6a, a coaxial cable comprises a center conductor and an outer conductor (some cables have an extra shielding layer) attached by a layer of dielectric material (e.g., polyethylene). Coaxial cables are available in a wide range of frequencies and suitable for various measuring circuits. These cables consist of layers of conductors that improve the shielding. The coaxial configuration provides a uniform area for propagating electric and magnetic fields within the transmission line, which are isolated from external disturbances. The most important parameter that should always be considered in designing a coaxial transmission line is its characteristic impedance. Many measurement circuits are designed for 50Ω impedance (e.g., Oscilloscopes), and it is critical to design a transmission line with a 50Ω impedance for perfect impedance matching and avoid reflection and attenuation of the original signal.

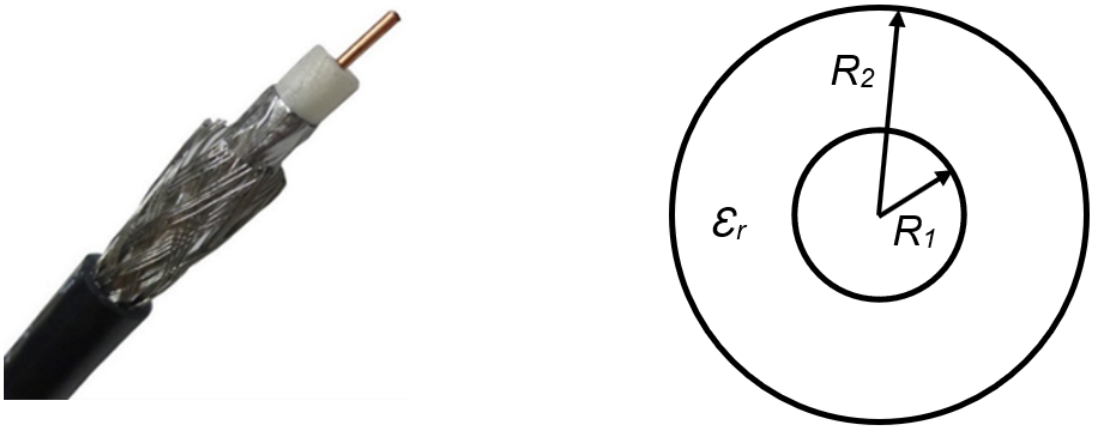

Figure 5.6 Schematics of a cylindrical shape coaxial transmission lines

As mentioned, the cylindrical coaxial cables depending on their applications, can be designed with different impedances, different materials, and bandwidths, but their characteristic impedances (Z_0) are obtained approximately through the following Equation [55].

$$Z_0 = \frac{1}{2\pi}\sqrt{\frac{\mu}{\varepsilon}} ln\left(\frac{R_2}{R_1}\right) \approx \frac{60}{\sqrt{\varepsilon_r}} ln\left(\frac{R_2}{R_1}\right) \quad (5.1)$$

Where μ and ε are dielectric permeability and permittivity, respectively, also, R_2 is an outer conductor radius, and R_1 is the radius of the inner conductor. As it is clearly shown in Equation (5.1), the changing of coaxial cable conductors' radiuses determines its characteristics impedance. Therefore, applying a cylindrical shape coaxial transmission line to measure the PD pulses would be difficult because most of the PD measuring testbeds are connected to the DAQ systems through a flat ground plate. In this case, if the center conductor of the transmission line is considered as that flat ground conductor (i.e., R1≈1.5-2 cm), the dimension of the PD testbed's transmission line would be significantly bigger than the size of the connecting cable and provides the termination issues.

An alternative method has been recommended in [24], [25] is a conical shape coaxial transmission line. As illustrated in Figure 5.2, the best configuration for terminating the PD source to the measuring circuit is using a conical transmission line. The upper surface of the conical transmission line provides enough planner surface for the PD source installation (e.g., the needle-plane configuration which simulates PD at sharp tips). The tapered diameter of the conical transmission line enables proper PD signal termination to RF connectors such as N-type and UHF connectors at the end of the testbed. The schematic of a conical shape coaxial transmission line is presented in Figure 5.7.

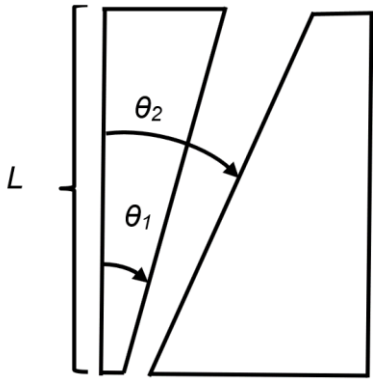

Figure 5.7 Schematics of a conical shape coaxial transmission lines.

Same as cylindrical shape coaxial transmission line, the characteristics impedance of a conical transmission line depends on the dimension of that and calculates by the following [55].

$$Z_0 = \frac{60}{\sqrt{\varepsilon_r}} ln\left(\frac{tan(1/2\,\theta_2)}{tan(1/2\,\theta_1)}\right) \tag{5.2}$$

Where θ_1 and θ_2 are the angles of the center and outer conductors of the transmission line, respectively. Also, ε_r is the relative permittivity of insulation between inner and outer conductors of the transmission line.

5.3.2 Finite Element Analysis Simulation

A numerical analysis is performed to design the conical transmission line while accounting for the manufacturing limitations. The main purpose of the numerical analysis is to examine the effect of the transmission line dimensions on its matching characteristics. The COMSOL Multiphysics' *Radio Frequency (RF)* module has been employed to simulate the requirements of a conical transmission line. The RF module has some physics interfaces to simulate traveling electromagnetic waves along a transmission line in both frequency and time domains. The

simulations were performed in both 2D axisymmetric and 3D dimensions. The geometry of the designed transmission line is presented in Figure 5.8. The 2D axisymmetric simulations are suitable for saving the memories during the parametric simulations for finding the optimal dimensions which meet both manufacturing and bandwidth limitations. Also, 3D simulations provide the advantages for observing the electromagnetic field propagations along the designed transmission line [54]. This feature can help us determine the best location for mounting sensors.

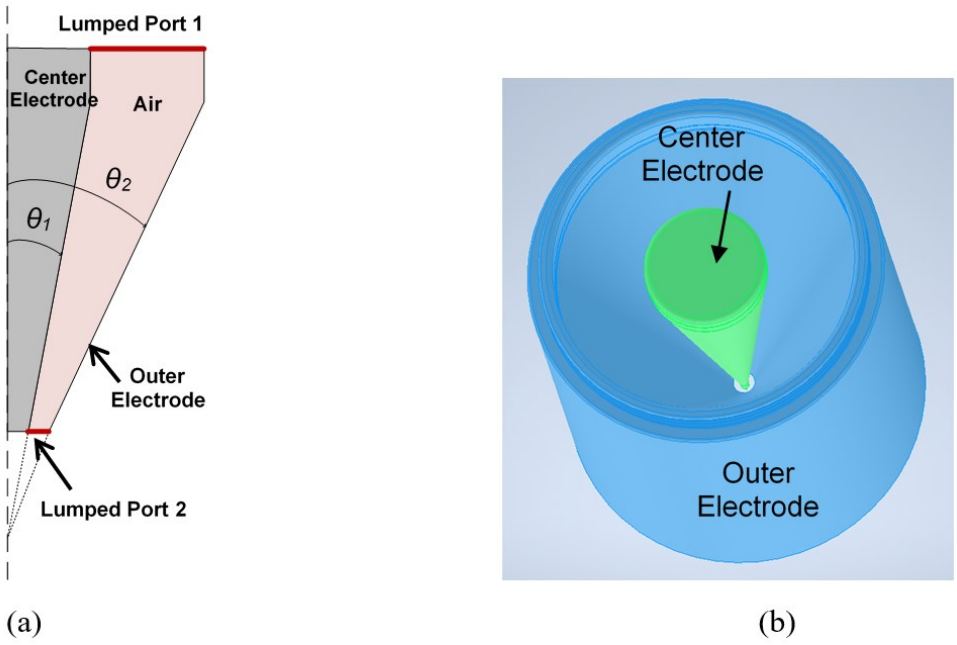

Figure 5.8 Sketch view of conical transmission line. (a) 2D axisymmetric, (b) 3D view [54].

As mentioned earlier, to achieve the optimized dimensions for our conical transmission line, which meets both manufacturing and impedance matching criteria, we performed a parametric simulation in 2D axisymmetric. The parametric simulation only includes the inner conductor angle (θ_1) and the transmission line (L). Indeed, understanding of these parameters is

enough for forming a conical transmission line because the outer conductor angle (θ_1) can be calculated by replacing 50Ω instead of Z_0 in Equation (5.2).

$$\theta_2 = 2 \times tan^{-1}(e^{\frac{5\sqrt{\varepsilon_r}}{6}} tan(\frac{1}{2}\theta_1)) \quad (5.3)$$

The values of step changes for the corresponding parameters in parametric sweep simulation are shown in Table 5.1

Table 5.1 The step changes of frequency, θ_1, and L in parametric sweep simulation.

Frequency (MHz)	θ_1 (deg)	L (mm)
0.1:5:6000	10:5:20	80:30:140

According to Table 5.1, the frequency changes from 100 kHz to 6 GHz by steps of 5 MHz. Similarly, θ_1 adjusts between 10 and 20 degrees by step of 5 degrees, and L values change between 80mm and 140 mm by step of 30 mm. The main reason for selecting the corresponding values and steps for θ_1 and L is the existing limitation for the diameter of our lathe machine, which is about 90mm. Also, according to our experience during simulation, there was no significant difference among smother steps for adjusting the corresponding parameters. In addition, to apply a voltage and current excitations to the transmission line, a coaxial *Lumped Port* node was used to figure out the input and output terminals with an impedance equal to 50Ω (red line on top and bottom of the transmission line in Figure 5.8a).

5.3.2.1 Frequency-domain Simulations

Figure 5.9 shows the simulation results of a parametric sweep in the COMSOL *RF* module. S-parameters such as S11 and S21 were employed to measure reflections and losses along the

transmission line. S11 is the forward reflection coefficient (input match) at port 1, and S21 is the forward transmission coefficient (gain or loss) from port 1 to port 2 when port 2 terminated in a perfect match. The port 1 and port 2 concept will be discussed later in this section.

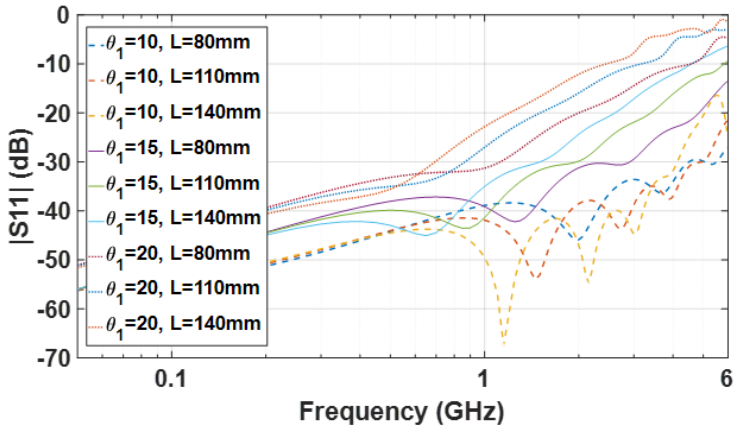

(a)

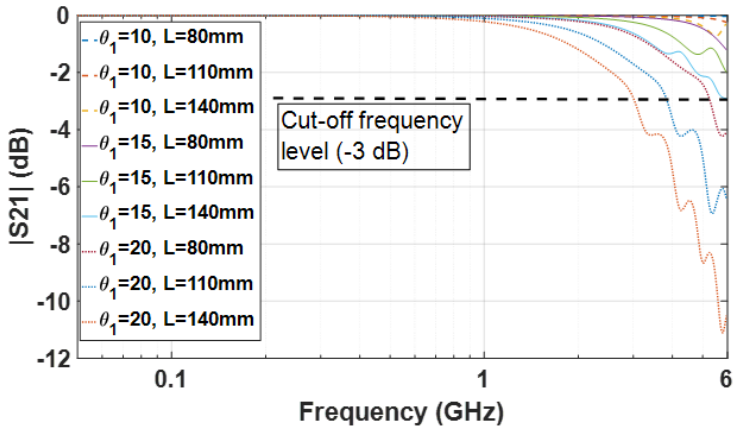

(b)

Figure 5.9 The frequency response of conical transmission lines. (a) S11: reflection coefficient, (b) S21: forward transmission.

Generally, the S11 values below -10dB and S21 values higher than -3dB can be assumed as acceptable criteria for a transmission line and determine the bandwidth. According to Figure 5.9a, it can be overly concluded increase of both angle and length of a conical transmission line

increase the amount of reflection (S11). For example, the transmission line with θ_1=20^o and L=140mm reaches the -10dB level at f=3GHz, while the transmission line with θ_1=10^o and L=80mm does not reach -10dB by 6GHz (i.e., around -22dB). Similarly, this is true in the case of attenuation along the transmission line (S21). According to Figure 5.9b, the transmission line with θ_1=20^o and L=140mm has a lower cut-off frequency f=3GHz among the other cases. However, as the reported individual PD pulses have a rise time in the range of hundreds of ps or slower, it seems all the assumed cases satisfy the PD measurement requirements. Therefore, the machining limitation should only be considered to select the right for our transmission line. Consequently, the conical transmission line with θ_1 = 15^o, θ_2 = 33.7$_o$, and L = 80 mm specifications that provide low reflection and high cut-off frequency (higher than 6 GHz) has been selected.

5.3.2.2 Time-Domain Simulations

As mentioned, one of the most important reasons for the design of transmission lines and understanding their S-parameters is the precise measurement of transient phenomena like PD. In this section, the effect of conical transmission line specifications (angle and length) changes on its timing response has been investigated. Figure 5.10 shows the responses of considered transmission lines in previous parametric simulation to two double-exponential pulses that represent individual PD pulses. The pulse has rising times equal to 500 ps and 1 ns.

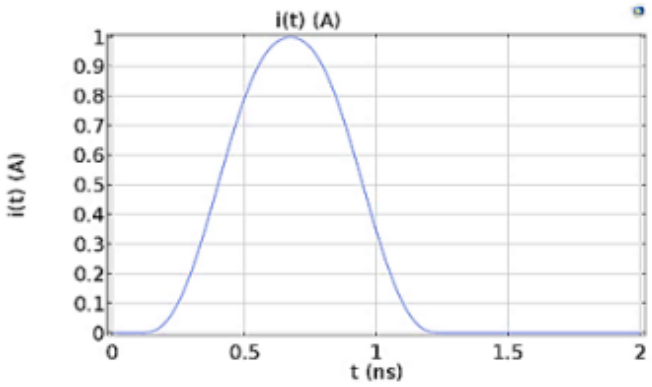

(a)

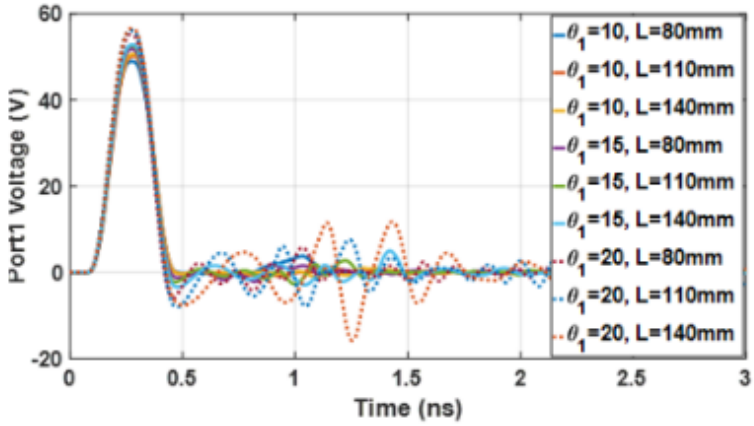

(b)

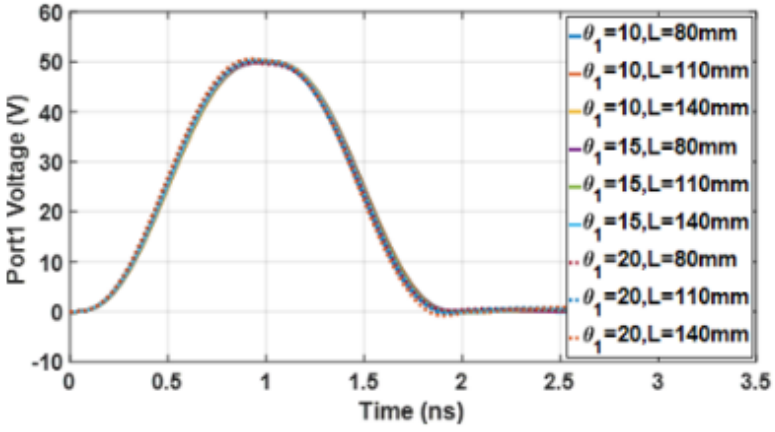

(c)

Figure 5.10 The time-domain response of designed transmission lines. (a) Example of applied pulse, (b) response to 500ps rise-time pulse, (c) response to 1ns rise-time pulse.

According to Figure 5.10b, all the assumed transmission lines in the parametric sweep simulation could propagate the 500ps rise-time pulse with tiny reflections and attenuation. In this mean, the transmission with θ_1=20° and L=140mm, which had lower frequency response, has higher reflection values around 1.75ns. It should be mentioned because of length changes among the cases; the reflection time is different among waveforms. In contrast, by applying a signal two times slower, all the assumed cases in parametric simulation present similar responses.

As an example, for better understanding the effect of a non-suitable transmission line on the measurement circuits of individual PD circuit, Figure 5.11 shows the response of a transmission line with a bandwidth about 200 MHz to a signal a fast double exponential pulse with rising time about 500ps. In this case, the waveshape of the traveling signal disturbs due to a mismatch of impedance among the transmission line and other parts of the circuit.

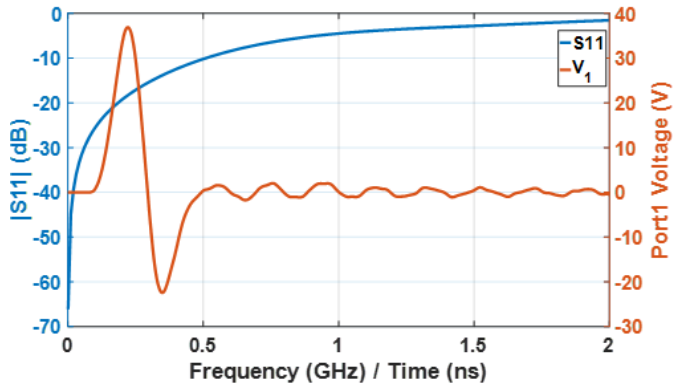

Figure 5.11 The response of a short bandwidth transmission line to a 500ps rise-time pulse.

5.3.2.3 3-D Simulation

For a good image of the electromagnetic wave propagation, the 3D model of the transmission line was simulated in COMSOL. Figure 5.12a demonstrates the direction of the power signal traveling downward the transmission line (blue color arrow), electric field (red color arrows), and magnetic fields (green color arrows). Accordingly, it is concluded from Figure 5.12a that the electric and magnetic fields in our designed transmission line are transverse waves. TEM is a mode of wave where their oscillations are perpendicular to the propagation direction. Also, the magnetic flux density (H) within the gap between the conductors that are filled by air has been displayed in both Figure 5.12a and 5.12b. The end of the transmission line, where terminates to connectors, has the highest intensity. Therefore, that area could be a suitable place for mounting loop sensors (e.g., B-dot). Figure 5.12b shows the electric field (red arrows) and magnetic field (green arrows) directions and surface current density at the sampling frequency of 1GHz.

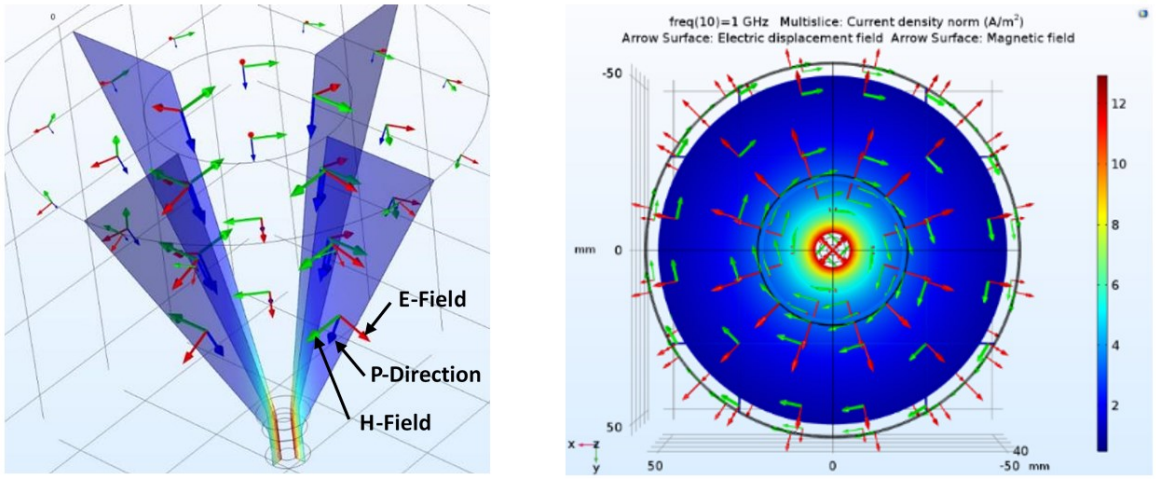

(a) (b)

Figure 5.12 3D simulation of the conical transmission line in the COMSOL. (a) Side view of signal propagation. (b) Top view of electric and magnetic fields at 1GHz.

5.3.3 Frequency Response Measurement of Manufactured Transmission line

After finding the right angle and length of the conical transmission line, it was manufactured, as shown in Figure 5.5. To measure the s-parameters of the manufactured transmission line, two conical transmission lines are connected back to back such that both ends are connected to a network analyzer. Figure 5.13 shows the connected transmission lines and the frequency response measurement circuit. As shown in Figure 5.13a, the two identical transmission lines are connected reversely to provide an even 50Ω waveguide. Both ends of assembled transmission lines are connected to the N-type connectors.

(a) (b)

Figure 5.13 Frequency Response measurement of the manufactured transmission line. a) Preparation of transmission line. (b) Test circuit connection. Note: The graphs shown on the screen of the NA are mere examples.

Also, as demonstrated in Figure 5.13b, the KEYSIGHT FieldFox Analyzer N9917A is used to measure the frequency response of the transmission line. Generally, the network analyzers are equipped by two ports, commonly called Port1 and Port 2, and connect to the test object. Depending on the measurement, both of Port1 and Port2 connectors can be connected to the test object or either of those can be connected. After that, a specific amount of power with various frequencies is injected into the test object, and the values of the reflected signal and transferred one to the other port are measured to calculate the frequency response of a test object. The measured parameters are commonly called S-parameters and present in the frequency range. Therefore, S11 is the forward reflection coefficient (input match) at port 1, and S21 is the forward transmission coefficient (gain/loss) from port 1 to port 2 when port 2 terminated in a perfect match.

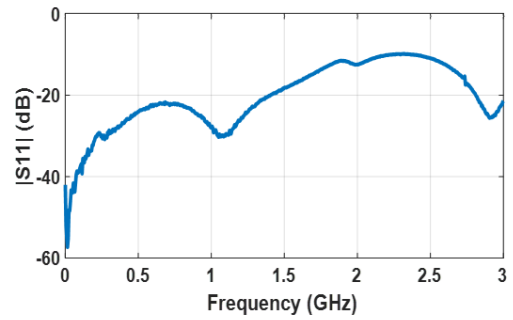

(a)

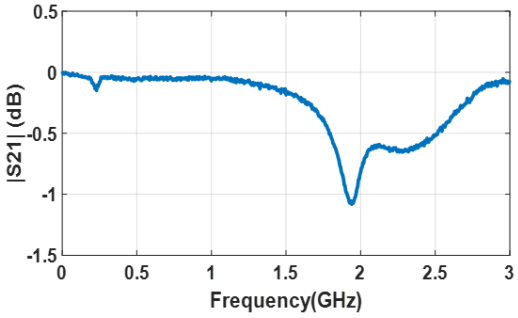

(b)

Figure 5.14 The frequency responses of the manufactured transmission line. (a) Reflection coefficient S11, (b) Attenuation coefficient S21.

However, we connected both ends of our transmission line to the network analyzer's Port1 and Port2 to find its reflection (S11) and attenuation (S21) parameters. The results of the frequency response measurement are presented in Figure 5.14. As shown in Figure 5.14a, the designed conical transmission line reflection is less than -10dB up to 2.2GHz. Moreover, the cut-off frequency (-3dB level) of S21 of the transmission line in Figure 5.14b is higher than 3 GHz. The obtained results are not exactly following the simulation results in Figure 5.9 due to the differences between the ideal assumptions of the simulation (purely 50 Ω coaxial lumped port) and the actual experimental setup. However, measurements shown in Figure 5.14 suggest that the designed transmission line has a sufficiently wide bandwidth and low reflections and attenuations, thus suitable for individual pulse measurements of PDs with dominant frequencies lower than 2.2 GHz.

5.4 Summary

This Chapter presented the design requirements of corresponding testbeds for the analysis of individual PD pulses. First, all IEC 60270 requirements for PD measurement circuit are taken into account and designed. Subsequently, the detailed dimensions of the testbed are determined through FEA simulation using Comsol Multiphysics. In addition, a 50 Ω coaxial TL that provides a reflection-free path for PD pulse-induced current and electromagnetic waves is designed and constructed. Finally, the designed testbed ensures a PD-free environment up to 20 kV and is equipped with a transmission line with a bandwidth of 2.2 GHz. The designed transmission line provides a low-loss and low-reflection path for the propagation of individual PD pulses.

CHAPTER VI

ELECTROMAGNETIC FIELD D-DOT AND B-DOT SENSORS PREPARATION

6.1 Motivation

The obtained results of the experiments performed in Chapter IV confirm the necessitate of utilizing the high frequency sensors to precise recording of the individual PD waveshapes. Non-conventional electromagnetic field sensors are a set of inductive (e.g., loop antenna) or capacitive (e.g., monopole antenna) coupling sensors that capture electromagnetic waves and react to a very fast transient phenomenon in the HF/VHF/UHF ranges. To clarify, non-conventional electromagnetic field sensors are not installed within the current path of PDs, unlike the conventional PD sensors that directly measure PD current. This chapter aims to present the requirement of electromagnetic field sensors design for PD application. Indeed, two differentiating type non-conventional electromagnetic field sensors, D-dots and B-dots, are developed in this Chapter to respectively measure the electric and magnetic fields radiated by the individual PD pulses.

6.2 Design of D-dot and B-dot Sensors

The D-dots and B-dots are capacitive and inductive coupling electromagnetic field sensors, respectively, with a low price, simple design, compact size, and very high frequency response ranges [56]. Also, convenience in the calibration process of the D-dot and B-dot sensors and their sensitivities comparable with the existing electromagnetic sensors make them more suitable for

the measurement of transient voltages and currents. Using the D-dot and B-dot sensors to measure pulses with pico-seconds rising times in pulsed power applications have been reported in [36], [56].

6.2.1 D-dot Design

Figure 6.1 presents the schematic of D-dot mounted on the designed transmission line and its equivalent circuit regarding the provided model in [36], [56]. As shown in Figure 6.1a, the D-dot sensor is capacitively coupled via $C_{D\text{-}dot}$ and C_{par} with the center conductor and the shielding of the transmission line, respectively. The parasitic capacitances (C_{par}) in Figure 6.1b are parallel with the characteristic impedances of connecting cable (Z_{cable}). Therefore, induced voltage by the discharge current of individual PD ($V(i_{PD})$) is calculated by Equation (6.1) [36].

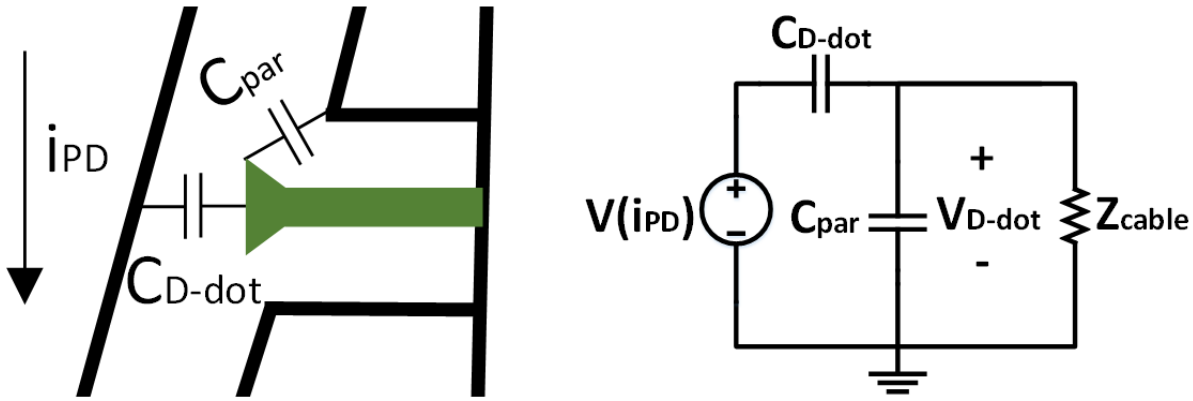

Figure 6.1 Specification of D-dot sensor. (a) Schematic of D-dot mounted within a conical transmission line. (b) Equivalent circuit of D-dot sensors.

$$V(i_{PD}) = \left(\frac{C_{Ddot} + C_{par}}{C_{D-dot}}\right) V_{Ddot} + \frac{1}{Z_{cable} C_{Ddot}} \int_0^t V_{Ddot} dt \qquad (6.1)$$

Consequently, by converting Equation (6.1) into the frequency domain, the transfer function of the D-dot sensor ($H_{D\text{-}dot}(j\omega)$) is obtained as in Equation (6.2) [36].

$$H_{D-dot}(j\omega) = \frac{V_{Ddot}(j\omega)}{V_{iPD}(j\omega)} = \frac{j\omega C_{Ddot} Z_{cable}}{j\omega\left(C_{Ddot} + C_{par}\right) + 1} \tag{6.2}$$

Equation (6.2) shows that the D-dot sensor operates as a differentiating sensor for frequencies that satisfy $j\omega(C_{Ddot} + C_{par}) \ll 1$. On the other hand, the sensor operates in a proportional mode (i.e., self-integrating mode) for frequencies that satisfy $j\omega(C_{Ddot} + C_{par}) \gg 1$. Generally, the size of the sensor tip (flat head area) and the distance of the sensor from the center conductor of the transmission line (location) determines the value of the $C_{D\text{-}dot}$. Accordingly, the $C_{D\text{-}dot}$ of Equation (6.2) determines the sensitivity and upper-band frequency of differentiating mode.

6.2.2 B-dot Design

According to the obtained results in Figure 5.12, to utilize high-intensity magnetic fields occurring at the bottom end of the conical transmission line, where it is terminated to an N-type connector, the B-dot sensor was placed near the bottom. Figure 6.2 represents the schematic of the B-dot sensor at the bottom of the designed transmission line and its equivalent circuit based on the provided model in [36], [56]. As shown in Figure 6.2, the model of B-dot consists of a mutual inductance *M* between the sensors and the center conductor of the transmission line and a self-inductance *L* of the sensor. Also, Figure 6.2b shows the equivalent circuit of the B-dot sensor in which the *L* connects in parallel with the characteristic impedance of the connecting cable. Therefore, the induced PD pulse discharge current can be calculated through Equation (6.3) [56].

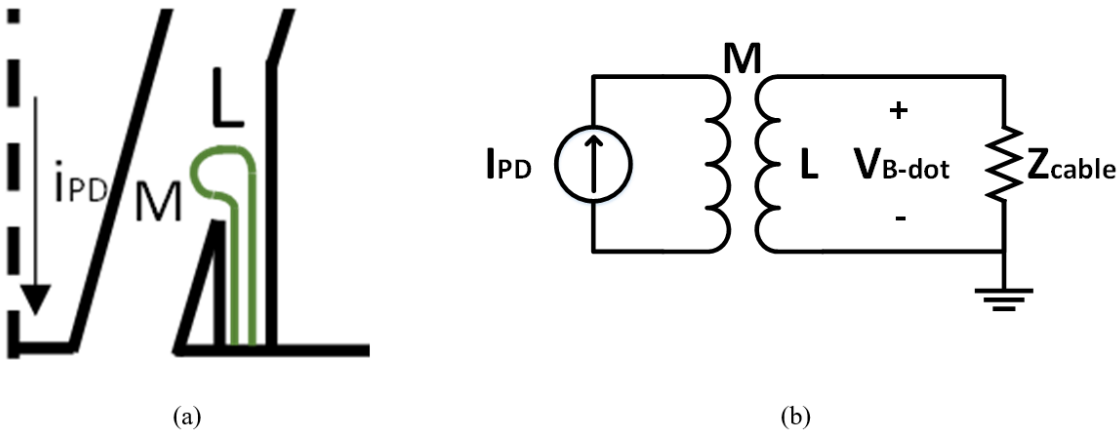

(a) (b)

Figure 6.2 Specification of B-dot sensor. (a) Schematic of B-dot mounted at the bottom of the designed conical transmission line. (b) Equivalent circuit of B-dot sensors.

$$I_{PD} = \frac{1}{M}\left(\frac{L}{Z_{cable}}V_{Bdot} + \int_0^t V_{Bdot}dt\right) \tag{6.3}$$

Subsequently, the transfer function of the B-dot sensor is modeled as follows [56].

$$H_{Bdot}(j\omega) = \frac{V_{Bdot}(j\omega)}{I_{PD}(j\omega)} = \frac{j\omega M}{j\omega\frac{L}{Z_{cable}} + 1} \tag{6.4}$$

Equation (6.4) shows that the B-dot sensor performs in a differentiating mode at frequencies that satisfy $j\omega\frac{L}{Z_{cable}} \ll 1$. On the other hand, it works in a proportional mode for frequencies that satisfy $j\omega\frac{L}{Z_{cable}} \gg 1$. The value of *M* in Equation (6.2) is a function of the distance between the B-dot loop and the center conductor of the transmission line. Also, the size of the B-dot loop and wire thickness determine the value of *L*. By adjusting the *M* and *L* values, the sensitivity and upper-band frequency of the differentiating mode can be controlled. However,

it should be noted; the sensors should be operated in either of the two modes (differentiating or proportional) within a given bandwidth to enable consistency in the distinguishing process of signals.

6.3 Finite Element Analysis Simulation

6.3.1 D-dot Sensor Simulation

According to Figure 6.3, which demonstrates the direction of electric and magnetic fields, we mounted our sensors around the designed transmission line. As shown in Figure 6.3, the D-dot sensor mounted on the sidewall of the shielding conductor of the transmission line. This position resulted in the propagated electric fields caused by traveling PD discharge current touch the D-dot sensor perpendicularly.

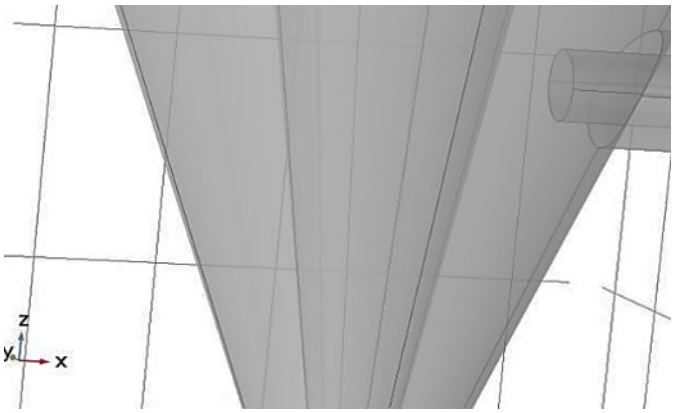

Figure 6.3 Location of D-dot sensor around the transmission line in simulation.

Referring to equations (6.1) and (6.2), the location and size of a D-dot sensor affect the characteristics, *e.g.,* its sensitivity through changing the coupling capacitance and parasitic capacitance. To achieve this goal, we performed a parametric simulation in the *RF* module of COMSOL to find an optimized dimension for making a D-dot sensor. Figure 6.4 presents the

results of the parametric simulation. The parametric simulation considers three radiuses R = 1.5, 3, and 4.5 mm for the head size of the D-dot sensor and three lengths L = 8, 11, and 14 mm, which determines the distance between the sensor and center conductor of the transmission line. Indeed, changes of both radius and length of the D-dot sensor affect the $C_{D\text{-}dot}$ and C_{par} values in equations (6.1) and (6.2) through the fundamental Equation (6.5) for calculating the capacitance.

$$C = \frac{\varepsilon A}{d} \tag{6.5}$$

C is the capacitance, ε is the permittivity; A is the area, and d is the distance between conductors.

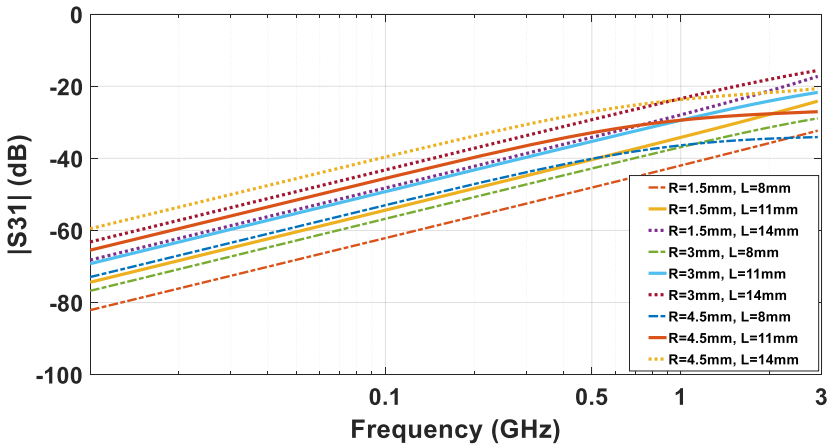

Figure 6.4 Results of location and size changes of the D-dot sensor on its frequency response.

As shown in Figure 6.4, the increase of either radius or length of the D-dot sensor improves its sensitivity. This improvement is more obvious by changing sensor length, which brings the sensor closer to the center conductor of the transmission line. For instance, incrimination of D-dot length from 8 mm to 14 mm (*i.e.,* bringing the sensor 6 mm closer) results in 20 dB improvement in the

frequency response of the D-dot sensor. In addition, although the increase of *R* between 1.5 and 3 mm (dashed lines) with the length of the sensor equal 8 mm improves the sensitivity of D-dot, it significantly causes a transition between differentiating and proportional modes. As seen in Figure 6.4, the slope of the D-dot sensor graph with a radius equal 4.5 mm is not increasing linearly by 3 GHz. The slope of D-dot response with a 4.5 mm radius is constant for the frequency above 1 GHz, which means the sensors work in proportional mode.

Moreover, figure 6.5 gives more information about the principal of D-dot sensor operation. As shown in that figure, the head of the D-dot sensor exposes the electric field arrows radiated by the center conductor of the transmission line. It is clear that mounting the D-dot sensor closer to the center conductor and making the head of that larger improve its sensitivity. The only concern is just a transition among differentiating and proportional modes, which can be different by design.

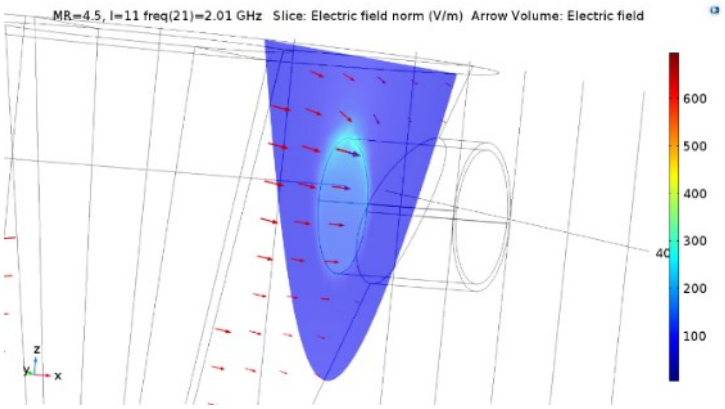

Figure 6.5 Example of the D-dot sensor exposed to the radiated electric field at f= 2GHz.

6.3.2 B-dot Sensor Simulation

To examine the output of the B-dot sensor regarding the mathematical model presented in equations (6.3) and (6.4), we performed a couple of parametric simulations in the COMSOL. The

parametric simulation includes the investigation of the number of B-dot loops and its location on the sensitivity of the sensor. Figure the view of the investigated B-dot sensor with adjustable loops. Also, the distance between the B-dot and center conductor of the transmission line control by adjusting the height of the sensor. As the transmission line is the conical shape; thus, the increase of the sensor length brings it closer to the center conductor of the transmission line.

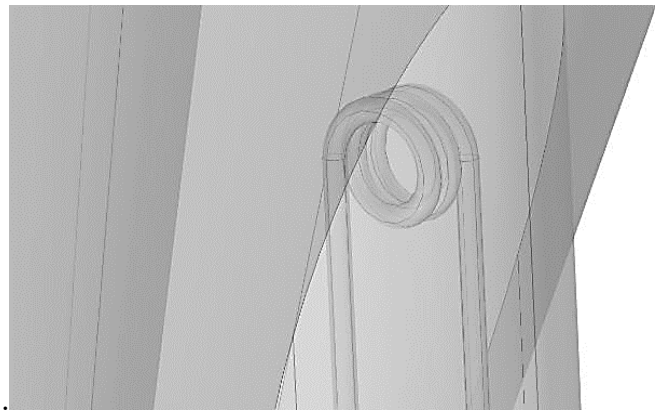

Figure 6.6 A typical view of the multi-loop B-dot sensor in COMSOL simulation.

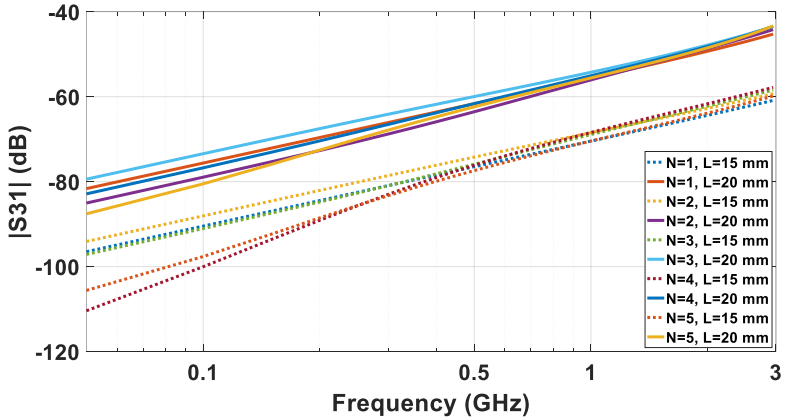

Figure 6.7 The results of the number of loop and distance changes on the frequency response of the B-dot sensor in parametric simulation in COMSOL.

The results of the parametric simulation are presented in Figure 6.7. As shown in the figure, a decrease of distance between the B-dot and center conductor of the transmission line improves the sensitivity of the sensor. For example, an increase of the sensor height from 15 mm to 20 mm when B-dot has a single loop causes the 15 dB improvement in B-dot sensitivity. In contrast, an increase in the number of loops has no significant effect on the sensitivity of B-dot. In addition, it can be observed that the sensitivity of simulated B-dot sensors is very low. It is related to the low intensity of radiated magnetic fields along the transmission line compared to electric fields. Therefore, instead of increasing the number of B-dot sensor loop, it is better to put the sensor closer to the center conductor of the transmission line, specifically, areas with more intensity such as the end of the transmission line. It can also be concluded in equation (6.3). According to equation (6.3), in the differentiating mode of the value of mutual inductance (M) determines the sensitivity of the B-dot sensor. Therefore, the value of M is a function of the distance between the sensor and the center conductor of the transmission line.

The magnetic field radiated around the sensor is plotted in Figure 6.8 to understand the B-dot sensor operation. Depending on the distance between the sensor and center conductor of the transmission line, the electric field with various intensity passes through the B-dot sensor. The size of the arrows in this figure represent the intensity of magnetic fields. The figure also includes the information of electric field intensity around the B-dot. The exposure of electric fields with a B-dot sensor conductor causes noise of dc to offset in the output response of the B-dot sensor. In cases this disturbance is too high, the suitable electrostatic shielding should be considered. Application of electrostatic shielding avoids the exposures of electric field arrows with the B-dot sensor's conductor while the magnetic fields can pass through the sensor loop.

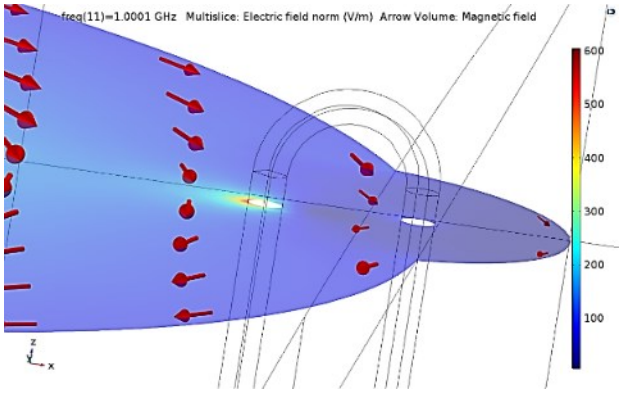

Figure 6.8 The direction of magnetic fields around the designed B-dot sensor.

According to the obtained results from Figure 6.7, the increase in the number of B-dot loop has no significance in its sensitivity while decreasing the distance can improve it better. Therefore, we change the B-dot sensor shape to meet both of them because of the previous simulation. The new face of the B-dot sensor is provided in Figure 6.9. This new style of the sensor provides advantages such as simplicity in design (*i.e.,* this is not as complicated as making a sensor with multiple loops), and higher mutual inductance because of its closer distance with the center conductor of the transmission line.

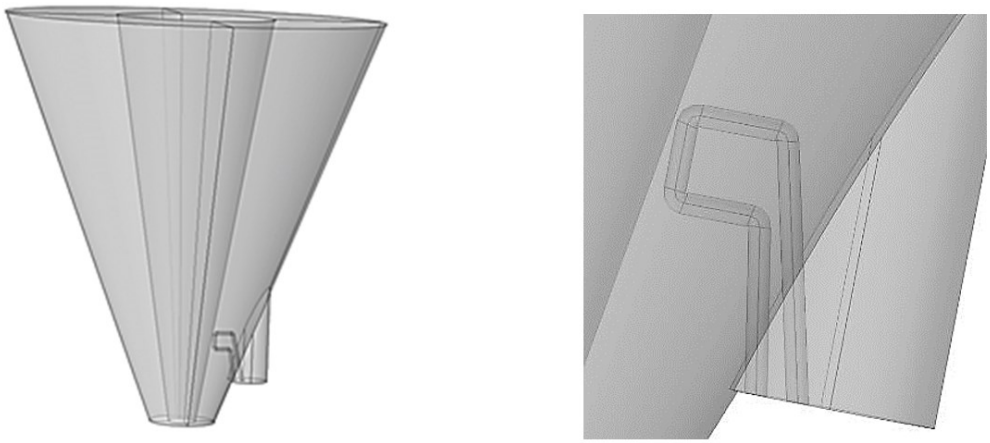

Figure 6.9 The position of a single loop B-dot sensor at the bottom of the transmission line.

The new B-dot looks like a square shape loop. To find the optimized size for the B-dot loop, we investigated a parametric simulation on the size of the loop and B-dot sensitivity. In this simulation, the distance between the B-dot and center conductors of the transmission line is kept constant. Indeed, the purpose of the test is to find the effect of B-dot's self-inductance changes on its frequency response. The result of the simulation is presented in Figure 6.10.

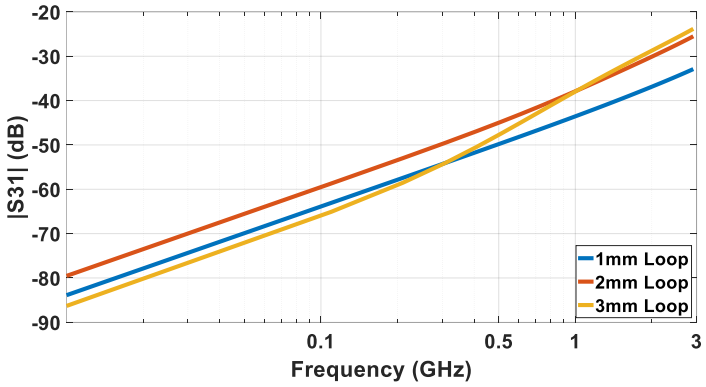

Figure 6.10 The results of B-dot loop size changes on its sensitivity.

As illustrated in Figure 6.10, the change of the B-dot sensor loop provides no more significant improvement in its sensitivity. This fact is in co0mpliance with results obtained from equation (6.4), which express the differentiating and proportional modes of B-dot sensor. In the differentiating mode, the output of the B-dot is mostly a function of mutual inductance (M) between the sensor and center conductors of the transmission line. In contrast, the self-inductance mostly affects the sensor's output when it works in the proportional mode. Therefore, it is acceptable that there is no significant difference in the graphs in Figure 6.10. Moreover, it can be obtained from Figure 6.10 that by the increase of the size of the B-dot loop from 2mm to 3 mm,

the slop of B-dot frequency response is not linear more. It can be considered a reason for the initiation of transition between differentiating and proportional working modes of B-dot.

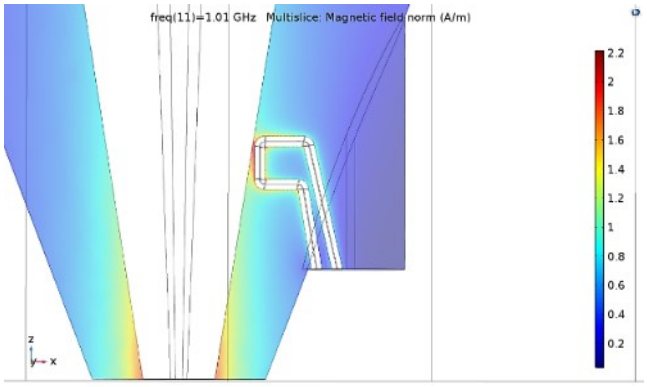

Figure 6.11 The surface plot of magnetic field norm distribution along with the B-dot sensor

Furthermore, the surface plot results of magnetic field distribution along the transmission line, and the B-dot sensor is presented in Figure 6.11. according to the results, the highest magnetic field exists at the bottom of the transmission line, where connects to N-type. Mounting the sensor at that point is not practically possible. Thus, we put the sensors as close as that position; however, the simulation result shown the highest magnetic field norms find around the conductor of B-dot.

6.4 Manufacturing of D-dot and B-dot sensor.

According to the obtained results from the finite element analysis simulation in the previous section, we manufactured two types of D-dot and B-dot sensors, as seen in Figure 6.12. As shown in the figure, the D-dot sensor is made by cutting a screw. Indeed, the screw includes a cone-shaped head, which provides a suitable size for the head of the D-dot sensor. The screw is

also soldered to a BNC type connector which can be connected to the DAQ system. Similarly, the B-dot sensor is made by forming a braided wire, which is shaped like a square loop.

Figure 6.12 Photos of manufactured non-conventional D-dot and B-dot magnetic field sensors

The B-dot sensor conductor also soldered to a BNC connector. The ease in the manufacturing of the D-dot and B-dot sensor allows us to investigate the sensors' outputs experimentally too. The presented sensors in Figure 6.12 represent the finalized size of sensors.

However, because of some difficulty and limitation on the practical mounting of made sensors around the transmission line, a couple of experimental investigation was performed to obtain the best location for the installation of sensors. Figure 6.13 presents the developed transmission line for experimental localizing of D-dot and B-dot sensors. As it is found in this figure, we provided a couple of holes in different locations and sizes. The purpose of the different locations is to adjust the distance between the sensor and transmission line. Similarly, the purpose of drilling different size of holes is to utilize sensors with various sizes. However, we briefly point to some limitations and difficulties during the placement of sensors around the transmission line.

Figure 6.13 Investigation of D-dot and B-dot locations around the transmission line.

First, the small hole sizes are provided to mount the SMA type connectors presented in Figure 4.4. Due to the short length of that connector, it can only be mounted on the top position of the transmission line, which is far from the center conductor of the transmission line and consequently decreases the sensitivity. Connecting the screw to the SMA type connector also makes the process of soldering very difficult. Therefore, the best size for the connector is the BNC type. As the head of the screw is equal to the diameter of BNC, they can be attached before mounting around the transmission line. In addition, because of terminating the transmission line to the connector at the end, the B-dot sensor should be mounted next to it or the side of the shielding conductor of the transmission line. The problem with the side shielding wall of the transmission line is its thickness, which requires a longer b-dot sensor to reach the center conductor of the transmission line. Therefore, we mount the B-dot at the bottom of the transmission line next to the N-type connector. The finalized location of sensors is shown in Figure 6.14. As shown, two B-dot sensors mounted at the bottom of the transmission line because of removing the unwanted common model in the sensor's output.

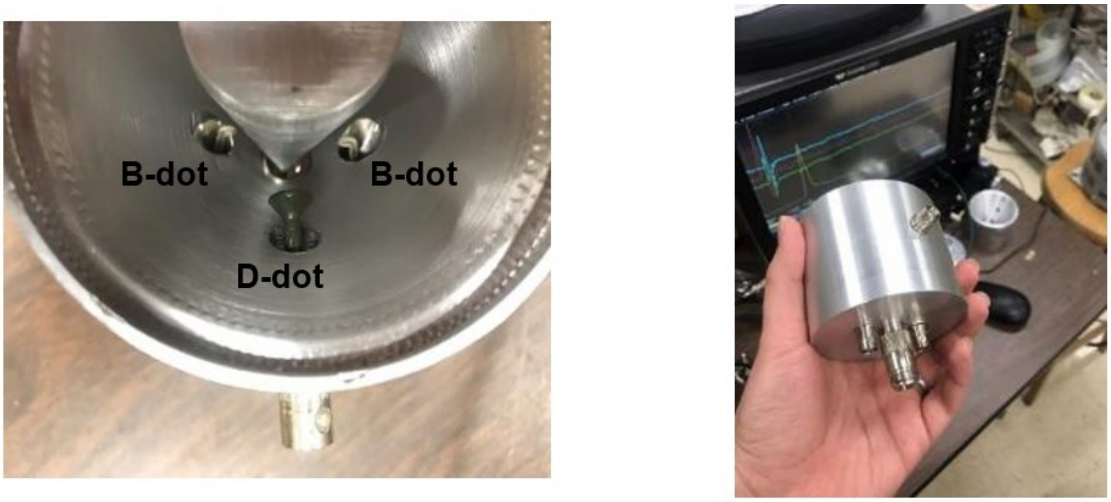

Figure 6.14 The final placement of D-dot and B-dot sensors around the transmission line.

6.5 Frequency Response of D-dot and B-dot Sensors

Like the transmission line, we performed a frequency measurement with a network analyzer to find the frequency responses of designed D-dot and B-dot sensors. Figure 6.15 presents the prepared test setup to measure the frequency responses of D-dot and B-dot sensors.

Figure 6.15 Frequency response measurement of D-dot and B-dot.

As shown in Figure 6.15, the test setup for measuring the sensor frequency responses is identical to the test setup of the transmission line except that one end of the transmission line is connected to a 50 Ω load. Here, Port 1 of the network analyzer is connected to the transmission line to excite power into the transmission line, while Port 2 measures the frequency responses of the D-dot and B-dot sensors individually. Figure 6.16 shows the frequency response of designed D-dot and B-dot sensors.

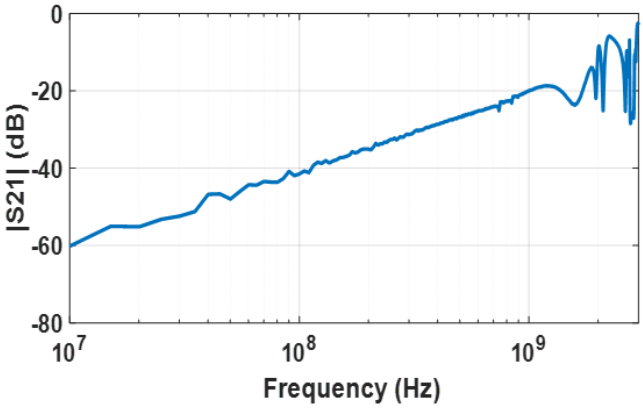

(a)

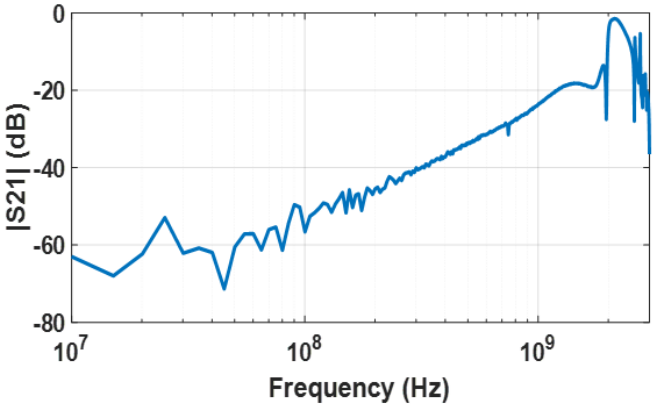

(b)

Figure 6.16 The frequency responses of designed magnetic field sensors. (a) D-dot, (b) B-dot.

As stated previously, the differentiating mode refers to regions in which the sensitivity of the D-dot and B-dot sensors change linearly in log scale while the proportional mode indicates constant sensitivity (e.g., shunt resistors and HFCTs). According to the purpose of this work, we are interested in using the D-dot and B-dot sensors, mostly in differentiating modes. The main reason is the simplicity in designing these types of sensors in differentiating modes for frequencies below 1GHz, which more applicable for the measurement of individual PD pulses. However, according to Figure 6.16, the D-dot and B-dot sensors operate in a differentiating mode up to 1.2 and 1.4 GHz, respectively, and convert to proportional mode after that. In other words, the sensitivity of the sensors is a function of the frequency components of the observed signal. It improves with the increase of the frequency within the differentiating mode regions of Figure 6.16. Therefore, this confirms that the designed D-dot and B-dot sensors can measure individual PD pulses with rising times on the range of hundreds of picoseconds (*i.e.,* <1.2 GHz). Indeed, the frequency component and the amplitude of PD signals determine the sensitivity of the sensors according to this figure. In general, if the PD pulse has frequency components in the differentiating mode, the outputs of the sensors are the derivative of that. In general, measurement accuracies of the D-dot and B-dot sensors decrease within the transition between two modes, due to the complexity of extracting original signals from sensor outputs [36], [56]. Therefore, it is recommended to operate sensors in either mode, but preferably in the differentiating mode due to simpler design. Moreover, it should be noted that the low SNR causes the oscillations of the B-dot response below 0.1 GHz in Figure 6.16b [56].

6.6 Summary

This chapter discussed the requirements of electromagnetic D-dot and B-dot sensors designs for individual PD pulse measurements. D-dot and B-dot are capacitive and inductive coupling electromagnetic sensors, mostly designed to work in derivative mode. Also, the sensitivity and frequency responses of both D-dot and B-dot are a function of their dimensions and locations from the origin. Therefore, a comprehensive numerical simulation was performed in this Chapter to find a good estimation of the location and dimension of corresponding sensors. After that, the sensors are constructed, and their location is determined according to both FEA simulation and experimental results. Finally, the frequency responses of both D-dot and B-dot sensors were measured through a VNA device, and the results demonstrated both sensors are operating in the differentiating modes for frequencies below 1.2 GHz. This range of frequency is more enough for individual PD waveshape investigations.

CHAPTER VII

INDIVIDUAL PARTIAL DISCHARGE WAVESHAPE MEASUREMENT

7.1 Motivation

This Chapter aims to measure the individual PD pulses using the designed and manufactured testbed and electromagnetic D-dot and B-dot sensors. All PD pulses are simultaneously measured with the 50 Ω input channel of the oscilloscope, which is considered as the reference to verify the outputs of D-dot and B-dot sensors. Initially, to start the experiment in this dissertation, we provided four types of PD defects. The DC and AC PD measurement was performed on the provided samples. In addition, the experiment in this Chapter aims to study the performance of D-dot and B-dot concerning various types of PDs. Indeed, various types of PDs comprise different discharge mechanisms, and we expect to observe discriminated responses from the sensors for each PD defect. This step also helps to compare the performance of D-dot and B-dot sensors with the reference sensor.

7.2 Partial Discharge Samples Preparations

Four different PD sources, as shown in Figure 7.1, are provided to be installed between the coupling capacitor and the center conductor of the conical transmission line.

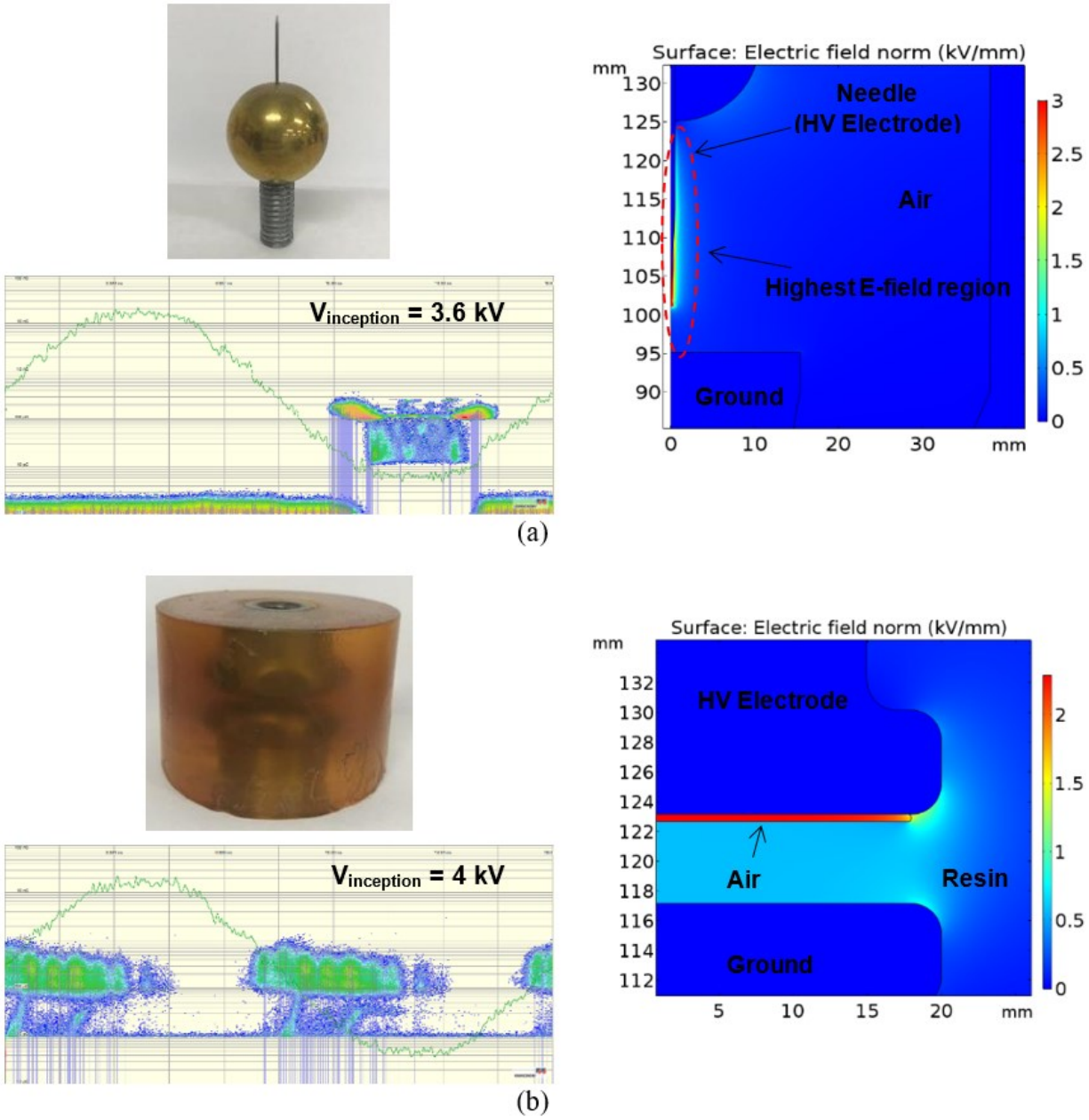

Figure 7.1 General view, phase-resolved partial discharge pattern, and finite element analysis specifications of prepared individual PD sources. (a) Corona discharge, (b) Cavity discharge, (c) Surface discharge, (d) Floating potential discharge sources.

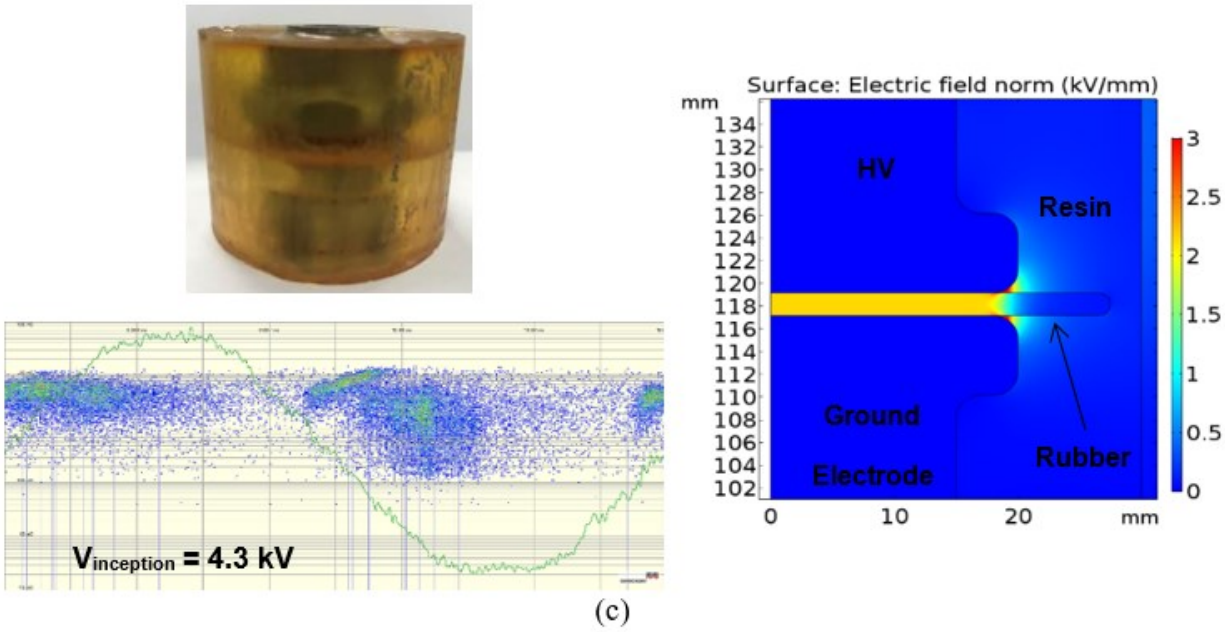

(c)

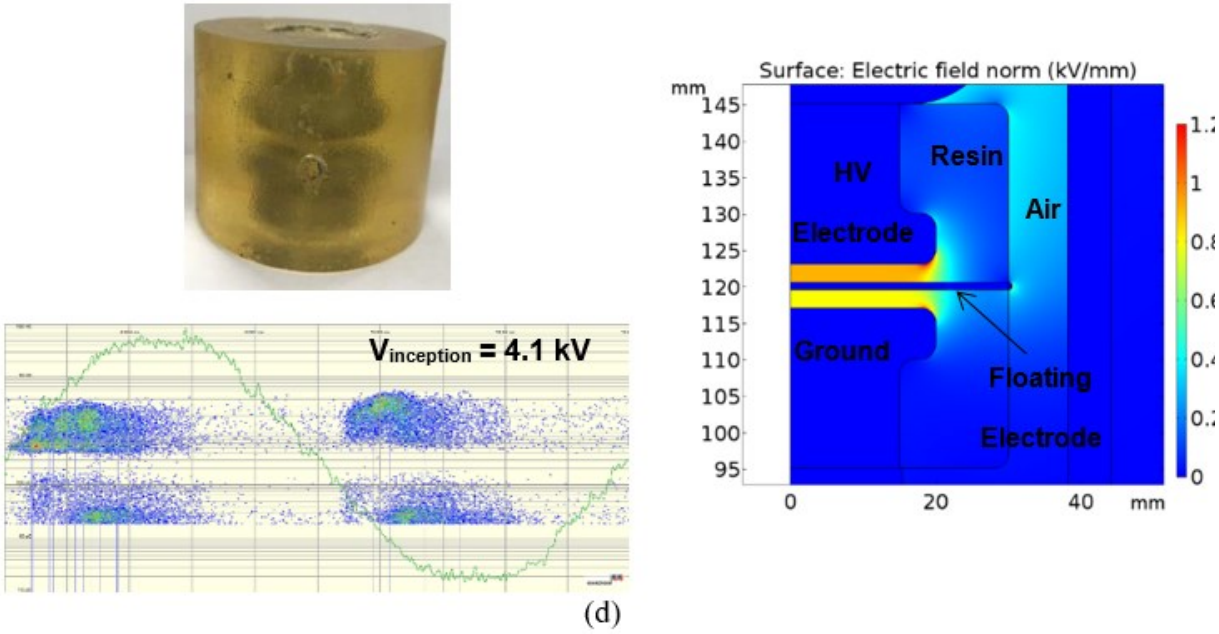

(d)

Figure 7.1 (continued)

As shown, Figure 7.1 includes the photos of four prepared PD sources and their AC PRPD patterns were measured with Omicron MPD 600 and their FEM electrostatic simulations in the COMSOL Multiphysics. Figure 7.1a illustrates a Corona discharge PD source. The Corona source includes a needle attached to a bolt connected to either a coupling capacitor or transmission line center conductor. Attachment of the Corona source to the coupling capacitor (HV side) results in PD signals in the negative cycle of applied AC voltage in PRPD patterns, commonly called negative Corona. In opposite, attachment of that to the transmission line (ground side) results in the PD signal in the positive cycle of applied AC voltage in the PRPD patterns, which commonly called positive Corona. Moreover, the results of electrostatic simulation in COMSOL show the most intensive electric fields are observed at the tip of the needle, which results in the ionization of air molecules and Corona occurrences.

Figure 7.1b shows the cavity discharge PD sample; this is made by providing a thin layer of air near one of the conductors surrounded by resin. Also, the measured PRPD pattern proves the validity of cavity discharge, and results of FEM simulation in COMSOL represent the highest electric field with the cavity is filled by air, which increases the risk of PD in that region.

Figure 7.1c demonstrates the provided surface discharge PD sample; in this sample, a thin layer of silicon rubber is surrounded by two conductors, which are molded in resin. The measured PRPD pattern in AC stress confirms the occurrence of surface discharge PDs. Also, the results of electrostatic simulation in COMSOL denotes the areas with higher electric field intensities where the space between the conductors and silicon rubber are increased. That area is filled by the resin whose insulation strength is lower than the silicon rubber, and the increase of electric fields across it results in the surface discharge. The information about the last PD source is presented in Figure 7.1d, which is shown as a floating potential discharge PD source. The floating potential PD is

related to the conductors which are not physically connected to either HV or ground sides in the HV apparatus. To simulate this type of PD, a piece of a metal rod is mounted between the two molded conductors within the resin. Similarly, the results of PRPD measurement and FEM simulation confirms the validity of this PD source.

7.3 Comparison of D-dot and B-dot Outputs with Reference Pulse

In this section, PD pulses occurring in the corresponding dielectric samples are measured. Figure 7.2 represents the experimental PD test setup for measuring the PD pulses to examine the performance of the designed testbed, which includes the 2.2 GHz bandwidth transmission line and the non-conventional sensors. The experimental setup includes a 200 kV DC Haefely Multi Test Set, a Haefely capacitive voltage divider, a 24 kV AC pole-mount transformer, and the designed PD testbed. Also, the figure denotes a way that test samples are tightened to the coupling capacitor and transmission line inside the testbed. In addition, all the PD signals, including reference, D-dot, and B-dot outputs, were measured by the LeCroy 806Zi-B (6 GHz - 4×40 GS/s) oscilloscope.

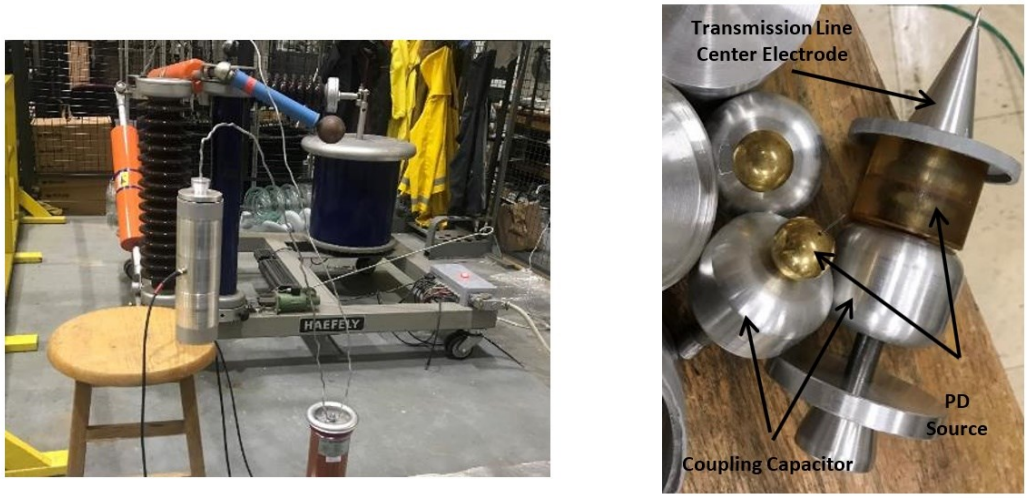

Figure 7.2 Experimental partial discharge measurement test setup.

During the experiment in this dissertation, we captured thousands of AC and DC PD pulses to investigate the time and frequency characteristics. Figure 7.3 illustrates a typical example of the captured cavity discharge by the corresponding sensors to compare the performance of D-dot and B-dot sensors with the reference pulse.

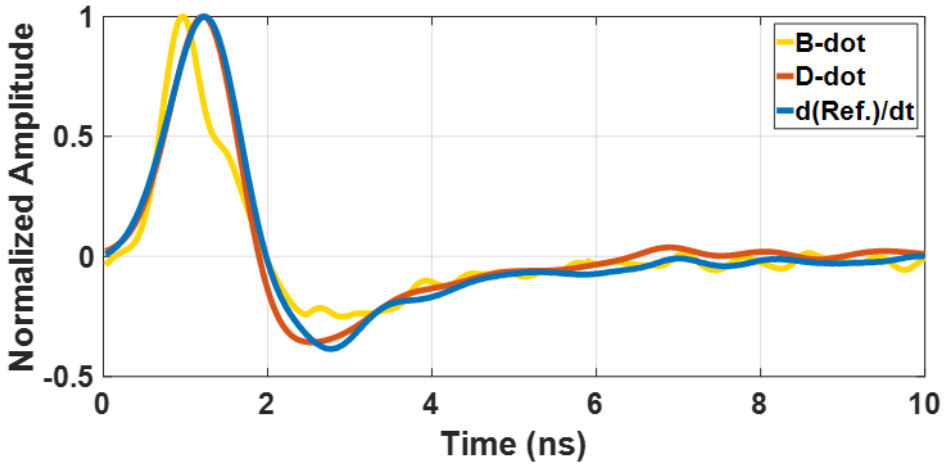

(a)

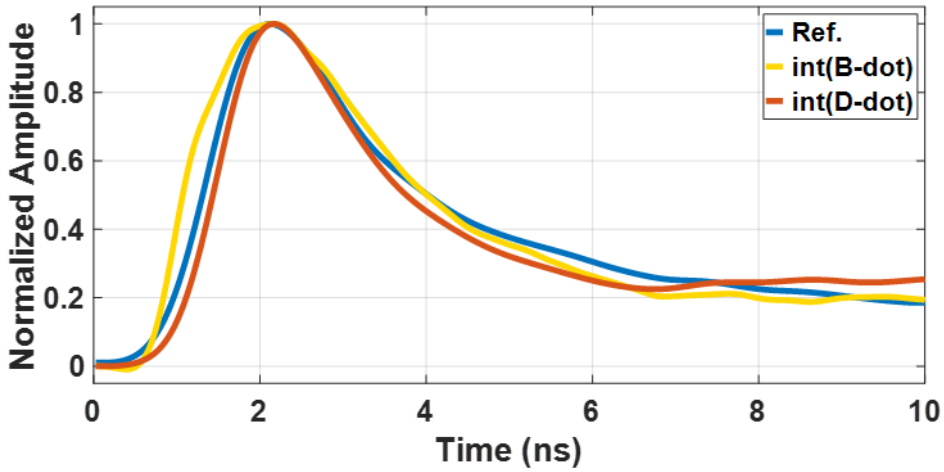

(b)

Figure 7.3 The measured results of a cavity PD pulse. (a) Test setup, (b) electromagnetic sensor (B-dot and D-dot) responses, (c) electromagnetic sensor response compared to the reference pulse.

In this work, the input 50 Ω resistance of the oscilloscope is considered a reference signal for the triggering and calibration of both D-dot and B-dot sensors. However, Figure 7.3a shows the normalized output of the B-dot and D-dot sensors and the differentiation of the reference pulse, measured by the 50 Ω input channel of an oscilloscope. The figure clearly shows that the output signals of both electromagnetic sensors differentiate PD pulses that are double exponential functions. Accordingly, the integration of the electromagnetic sensor outputs results in the reference PD waveform in the time domain. Figure 7.3b compares the normalized integration of D-dot and B-dot output signals with the reference pulse. As shown, the outputs of the D-dot and B-dot sensors fit well with the reference pulse, which contains rise time, decay time, 50% pulse width, and 20% pulse width. Beyond 10 ns, the integrated signals deviate from the reference PD pulse due to the low SNR of the non-conventional sensors caused by the low di/dt of the PD pulse. Table 1 presents statistical data comparing the integrated signals of D-dot and B-dot sensor measurements for 100 reference PD pulses. The table compares four characteristics of a double exponential waveform: rising time (Tr), decay time (Td), 50%, and 20% pulse widths (PW50 and PW20, respectively).

Table 7.1 D-dot and B-dot pulse characteristics vs reference pulse.

	Reference		D-dot		B-dot	
	Mean	σ	Mean (% error)	σ (% error)	Mean (% error)	σ (% error)
Tr	1.08	0.20	0.99 (% 8)	0.18 (% 10)	0.94 (% 13)	0.21 (% 5)
Td	3.83	0.74	3.61 (% 6)	0.64 (% 13)	4.52 (% 18)	1.02 (% 38)
PW50	2.72	0.59	2.19 (% 19)	0.64 (% 13)	3.45 (% 27)	1.12 (% 90)
PW20	6.53	1.21	5.45 (% 16)	1.87 (% 54)	5.94 (% 9)	2.35 (% 94)

- All values are in nanoseconds (ns)

As shown in the table, averages and standard deviations of both D-dot and B-dot sensor measurements agree with those of the reference PD pulses in the time domain. The low standard deviation among the recorded data for each sensor and the low error percentage of the D-dot and B-dot outputs compared to that of the reference confirms that the design is suitable for the individual PD pulse investigations. Furthermore, the average Fast Fourier Transform (FFT) analysis on 100 PD pulses is provided to compare the frequency spectra of the designed D-dot and B-dot sensors to those of the reference, as shown in Figure 7.4. The FFT results show correlations among the three sensors: 50 Ω input resistance of oscilloscope, D-dot, and B-dot. According to the results, the FFT response of the B-dot sensor begins to deviate from the reference signal at frequencies above 900 MHz. The substantial discrepancy shown in the high frequency range is mainly due to the high-frequency E-fields that cause disturbances in the response of the B-dot sensor. Electrostatic shielding or analog filtering could be applied [36] to suppress these disturbances. However, since the dominant frequency component of PD pulses are below 900 MHz, no filter was designed for the B-dot measurements in this work. Comparing sensor performances in frequency domain shows that the differentiating mode (dotted lines) provides more accurate DC PD pulse analysis.

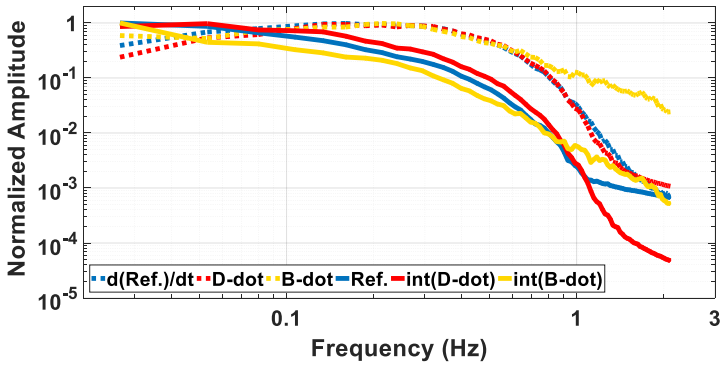

Figure 7.4 The frequency-domain comparison of D-dot and B-dot sensors outputs and their numerical integrations with reference.

The relatively poor performance of the B-dot sensor in the integrating mode (solid lines) is due to the integration of the high frequency noise of the sensor caused by E-field disturbances. Figure 7.4 also shows that, in general, the performance of the D-dot (E-field) sensor is better than that of the B-dot sensor in case of cavity discharge measurement. Hence, if timing parameters are not of interest, the differentiating mode should be used for PD analysis through the D-dot and B-dot sensors since it does not introduce numerical integration errors.

Therefore, to analyze the D-dot and B-dot response, we need to characterize their outputs' time parameters similar to Figure 2.16, which describes the time characteristics of a double exponential PD pulse. Figure 7.5 shows the general waveshape of D-dot and B-dot sensors. As shown in the figure, we denote the length of first and second cycles with T_1 and T_2, respectively. Duration of first and second cycles of D-dot or B-dot outputs refers to the time to peak and decay time of PD signal (i.e., double exponential waveform). Moreover, we measure the maximum (Max) and minimum (Min) of each waveform to inform the intensity of the captured PD signal.

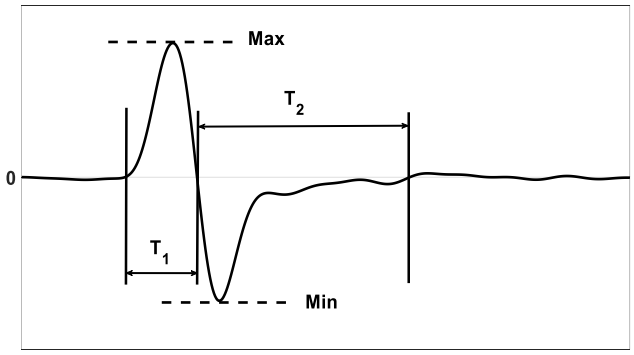

Figure 7.5 Time characteristics of D-dot and B-dot Output.

7.4 Investigation of Various Partial Discharge Mechanisms

In this section, we examine the discharge mechanism of various types of PDs. In general, the induced current of PD discharge results by forming electron avalanches and drifting of ions through the PD source. Therefore, investigation of various PD induced current pulses leads to find the existing discrimination among PD defects. Also, this information can be useful to classify and distinguish various types of PDs. However, in the following, we provide the discharge mechanisms of all the prepared PD sources in this work. The corresponding PD pulses were selected among the pulses with the highest occurrences. Also, some of these pulses are common among both AC and DC voltages, and some are only related to either of those or, in some cases, only observed under a specific polarity of DC voltage.

7.3.1 Cavity Discharge

Cavity discharge includes various types of discharge mechanisms such as Streamer-like, Townsend-like, and Pitting (corona-like) in which the time characteristics mainly depend on the existence of free electrons and the geometry of the voids [6]. According to the reported results in [6], the main characteristics of Streamer-like discharges are t_r values in the range of hundreds of ps and t_d values in the range of ns. In contrast, Townsend-like discharges include slow discharges with t_r values in the range of tens of ns, which follow the rate of electron avalanche formation and result in slow decaying time. Moreover, Pitting discharges exhibit t_r values comparable to the streamers with slower t_d caused by microscale crystals with sharp edges on the void surface. Figure 7.6 displays examples of typical measured AC and DC cavity discharge waveshapes in this study in both time and frequency domains.

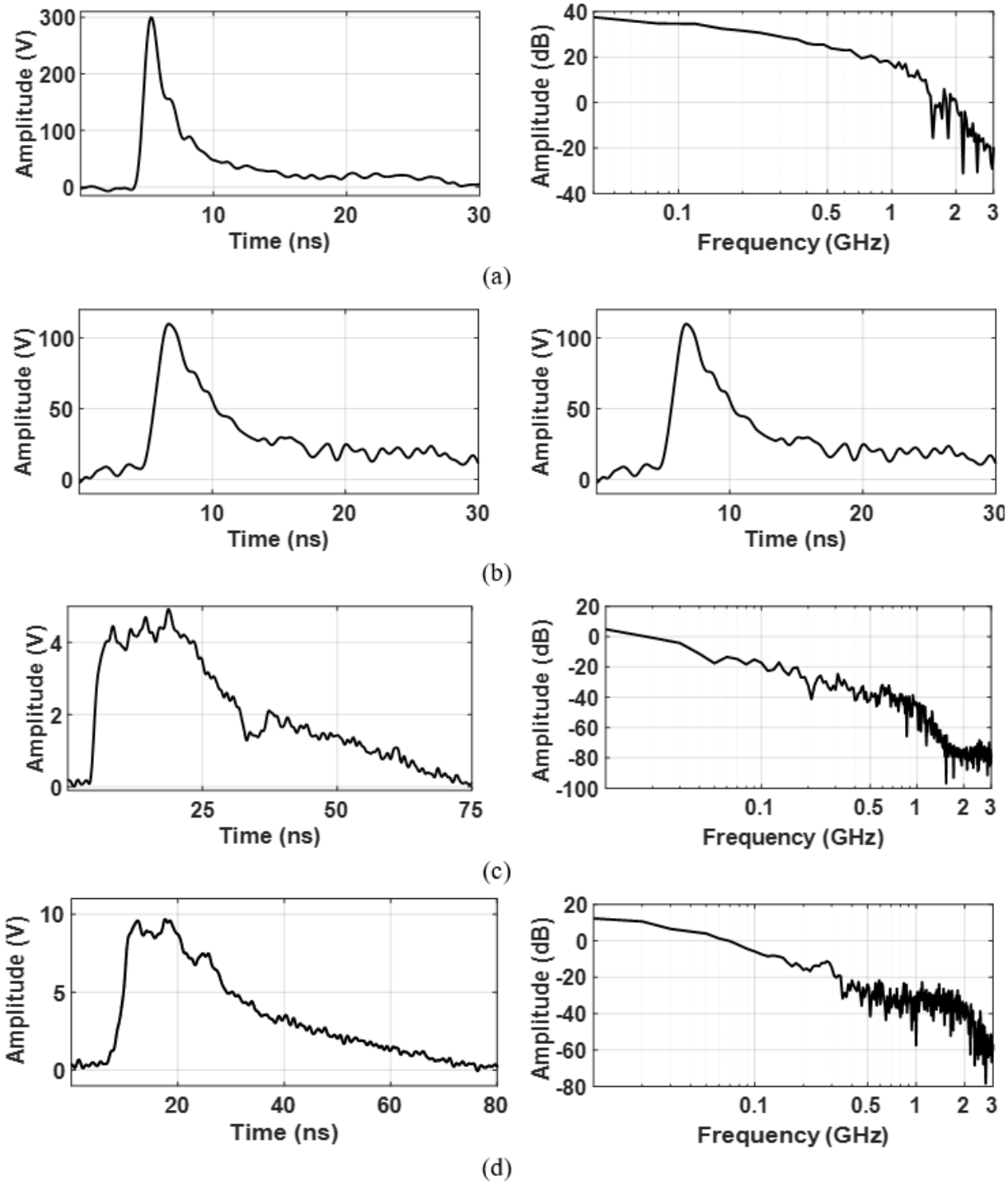

Figure 7.6 Examples of AC and DC cavity discharge waveforms in both time and frequency domains are measured by the 50 Ω input resistance of the oscilloscope. Waveform (a) and (b) are common among AC and DC; (c) positive DC, (d) negative DC.

Figure 7.6a shows the streamer-like pulse with fast t_r (< 1 ns) and t_d and short $t_{20\%}$, these types of pulses also present a significant amplitude (in the range between -20 dB to 40 dB) for frequency spectrums up to 1.5 GHz. Figure 7.6b represents the Townsend-like discharge with longer t_r, t_d, and $t_{20\%}$ than streamer-like pulses related to the delay in the initiation of electron avalanches and discharge channel formations. These pulses are common among both AC and DC measured pulses, except their amplitudes that are smaller in the case of DC PDs. Although the amplitude of frequency components pulses depends on the strength of discharge, these types of pulse have amplitudes higher than -20 dB for frequency below 1 GHz.

Besides the amplitude differences among cavity discharge pulses measured under AC and DC voltages, there are some varieties in the waveshapes of cavity discharge pulses captured with both polarities of DC, as shown in Figure 7.6c and 7.6d. These pulses include longer decay and pulse widths than those of AC, described by Pitting pulses. Consequently, these pulses have lower frequency components. According to Figure 7.6c and 7.6d, they have amplitudes of more than -20 dB for frequencies below 0.1 GHz and 0.3 GHz, respectively. In addition, it should be emphasized the inception voltage of PD pulses under both AC and DC stresses were not equal. For AC measurements, the inception voltage is 4.3 kV, and about 20,000 cavity discharge pulses were recorded.

In contrast, for DC measurement, because of a long delay between consequent PD pulses (no PD observed for about an hour waiting), the pulses were measured separately by steadily ramping up of the voltage until a cavity discharge was recorded. This process was continued until 1500 pulses were measured for each polarity of DC voltage. Averagely, the inception voltage cavity discharge for the same PD source was between 11 kV to 16 kV. Despite utilizing higher

voltage amplitude in DC application, the recorded pulses have lower amplitude than pulses measured in AC.

7.3.2 Surface Discharge PD Measurement

Generally, Surface discharge refers to the discharges resulted from discontinuities among the insulation media. Typically, Surface discharges are observed within the interface between two different insulation media (e.g., gas and solid media), where the electric field intensity exceeds the breakdown voltage of either corresponding insulation media. Figure 7.7 illustrates typical examples of Surface discharge waveforms captured in this work under AC and DC stresses.

It should be emphasized the recorded surface discharge pulse under DC stress have significantly lower amplitude pulses accompanied by longer pulse widths in cases such as waveshapes c and d.

As shown in Figure 7.7a, the Surface discharges similar to cavity discharges include streamer-like discharges, mostly observed in AC voltages with a frequency spectrum of more than -20 dB below 2.3 GHz. Figure 7.7b represents a captured Townsend-like discharge, which occurs commonly under both AC and DC stresses. These types of pulses have frequencies of more than -20 dB for frequency below 1.8 GHz. It should be noted that the captured pulses under DC show smaller amplitudes and longer pulse widths than AC-induced pulses. A possible reason for the differences is the slower rate of charge accumulation and distribution among the Surface discharges under DC. Also, the superimposed pulses resulting from unstable ionization processes, which show pulses with longer pulse widths, as shown in Figure 7.7c, are frequently recorded among the captured pulses under DC stresses.

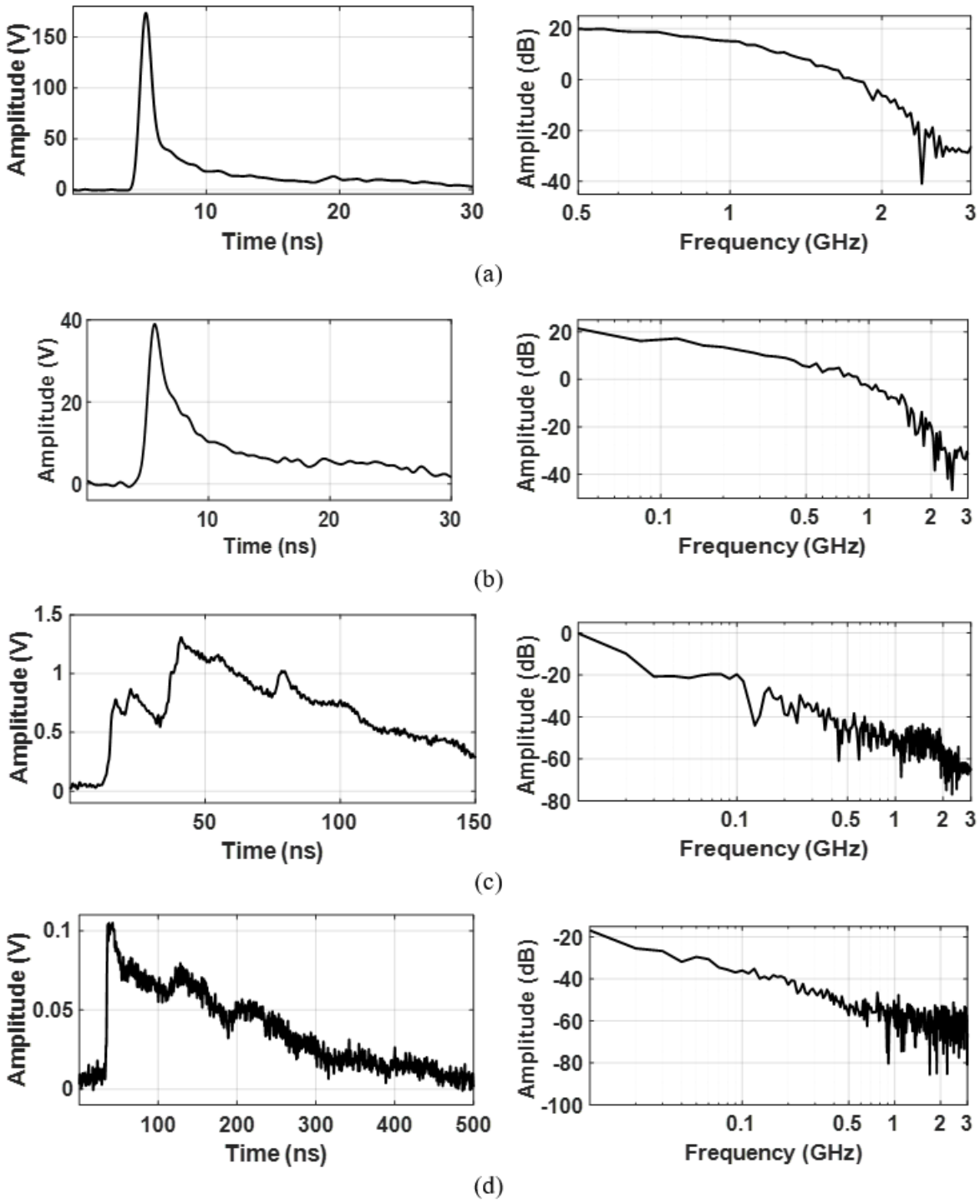

Figure 7.7 Examples of AC and DC surface discharge waveforms measured by 50 Ω input channel of oscilloscope in both time and frequency domains. (a) and (b) common within both AC and DC pulses. (c) and (d) observed just for DC pulses.

Moreover, Figure 7.7d demonstrates a pulse with fast rise time and slow decaying time on the range of hundreds of ns that is mostly similar to the pitting discharges. The presented pulses in Figures 7.7c and 7.7d have a low-frequency spectrum by 0.1 MHz. The inception voltage of Surface discharge pulses under AC stress is 4 kV while it is 7.6 kV under DC voltages. The repetition rate of Surface discharge pulses in DC was about 1.5 minutes averagely while it decreased to 3 seconds when the applied voltage increased to 14 kV. Despite utilizing higher voltage amplitude in DC application, the recorded pulses have lower amplitude than pulses measured in AC.

7.3.3 Corona Discharge PD Measurement

Corona discharges are caused by the ionization of particles around the sharp corners of conductors, which involves high-intensity electric fields. As the sharp edges can be located on either energized or ground conductors, we arbitrarily named the captured corona pulses when the sharp points exist on the HV conductor as negative corona discharges (NCOD), and when it is found around the ground conductor as positive corona discharge (PCOD). The main reason for this type of denomination is for the observation of strong corona discharge pulses on the negative cycle in AC voltage when the needle is connected to the HV conductor side. However, Figure 7.8a shows an example of the measured corona discharge pulses, common among both AC and DC stresses, and have a frequency spectrum of more than -20 dB below 0.5 MHz.

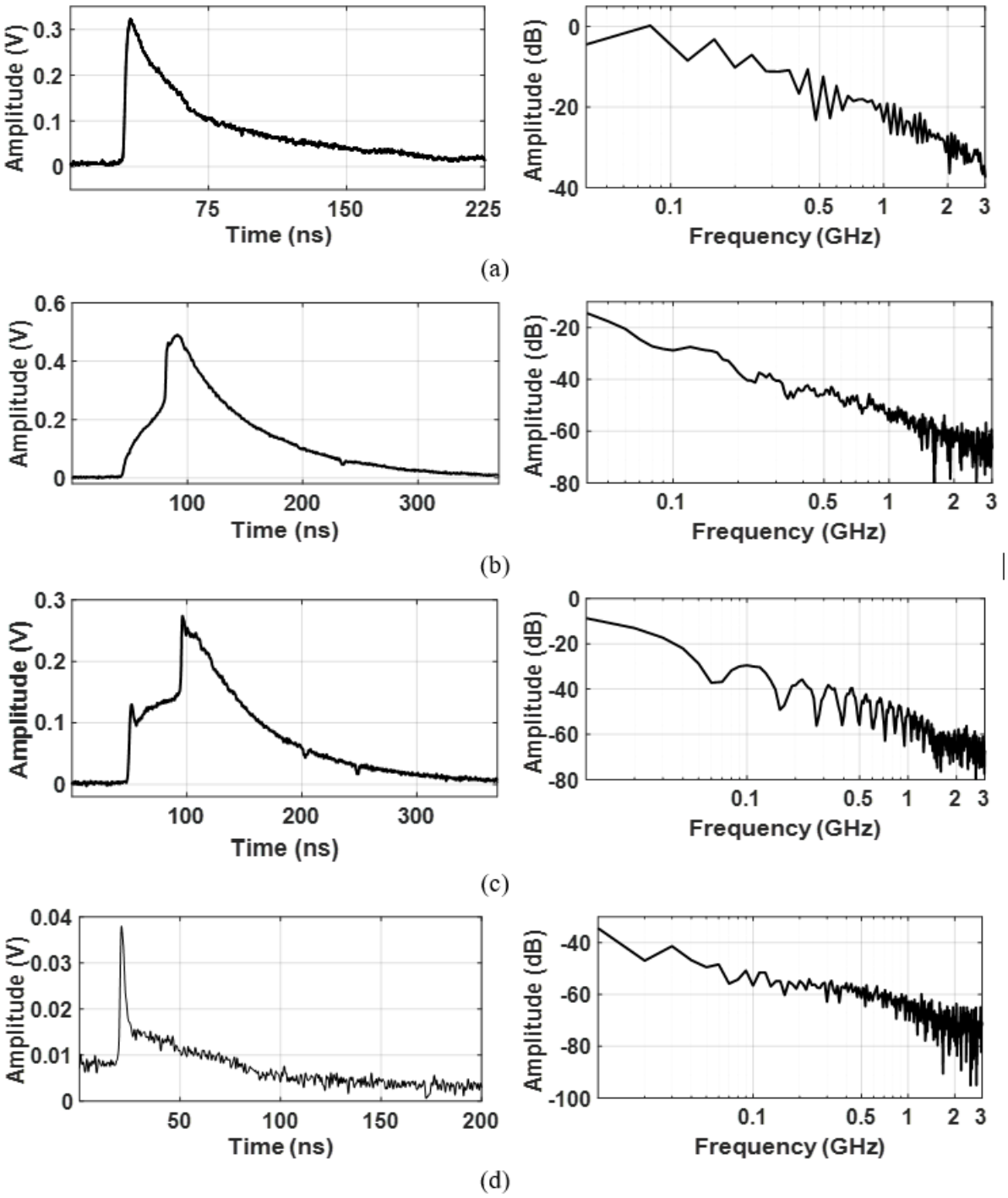

Figure 7.8 Examples of corona discharge waveforms under AC and DC stress in both time and frequency domains are measured by the 50 Ω input channel of the oscilloscope. (a) common among AC and DC pulses, (b) and (c) mostly observed in positive DC, (d) mostly observed in negative DC.

There is no significant difference between AC and DC corona discharge pulses except their amplitudes. Also, there have been some differences among NCOD and PCOD pulse widths in the same stress, which can be related to the ionization initiation around the needle because of voltage polarities. In addition to Figure 7.8a, which represents a common waveshape of a DC corona discharge, two more types of waveshapes were captured for corona discharges under DC(+). As shown in Figure 7.8b and 7.8c, these pulses have longer rise times than AC pulses with a significant frequency spectrum below 0.1 GHz. A reason for the longer rise time, specifically in Figure 7.8c, is the superposition of subsequent unstable ionization mechanisms.

Furthermore, Figure 7.8d demonstrate a type of corona discharge pulse which is mostly observed in the case of DC(-) and characterized by a waveshape with fast rise and decaying time, as well as long pulse width but not on the order of regular corona discharges, these types of pulses, have a very low-frequency spectrum which required an accurate measuring system with high signal to noise ratio. In addition, the inception voltage of recoded corona discharge pulses under AC is 3.6 kV while it is around 7.8 under DC stresses. Also, the corona discharge pulses were presented a repetition rate comparable with that of AC stresses which 1k pulses were recorded within 4 minutes. An interesting trend was observed during the DC corona discharge measurement. By increasing DC voltage from 7.8 kV to 6.8 kV, the amplitude of corona discharge pulses was decreased while their repetition rate was increased by 6 times. That was a repetitive trend which observed a couple of time by changes of voltage during some random intervals.

7.3.4 Floating Potential Discharge PD Measurement

Floating potential discharges are a type of discharges caused by the existence of suspended particles within an insulator. Figure 7.9 presents the examples of recorded floating potential discharge pulses in this work.

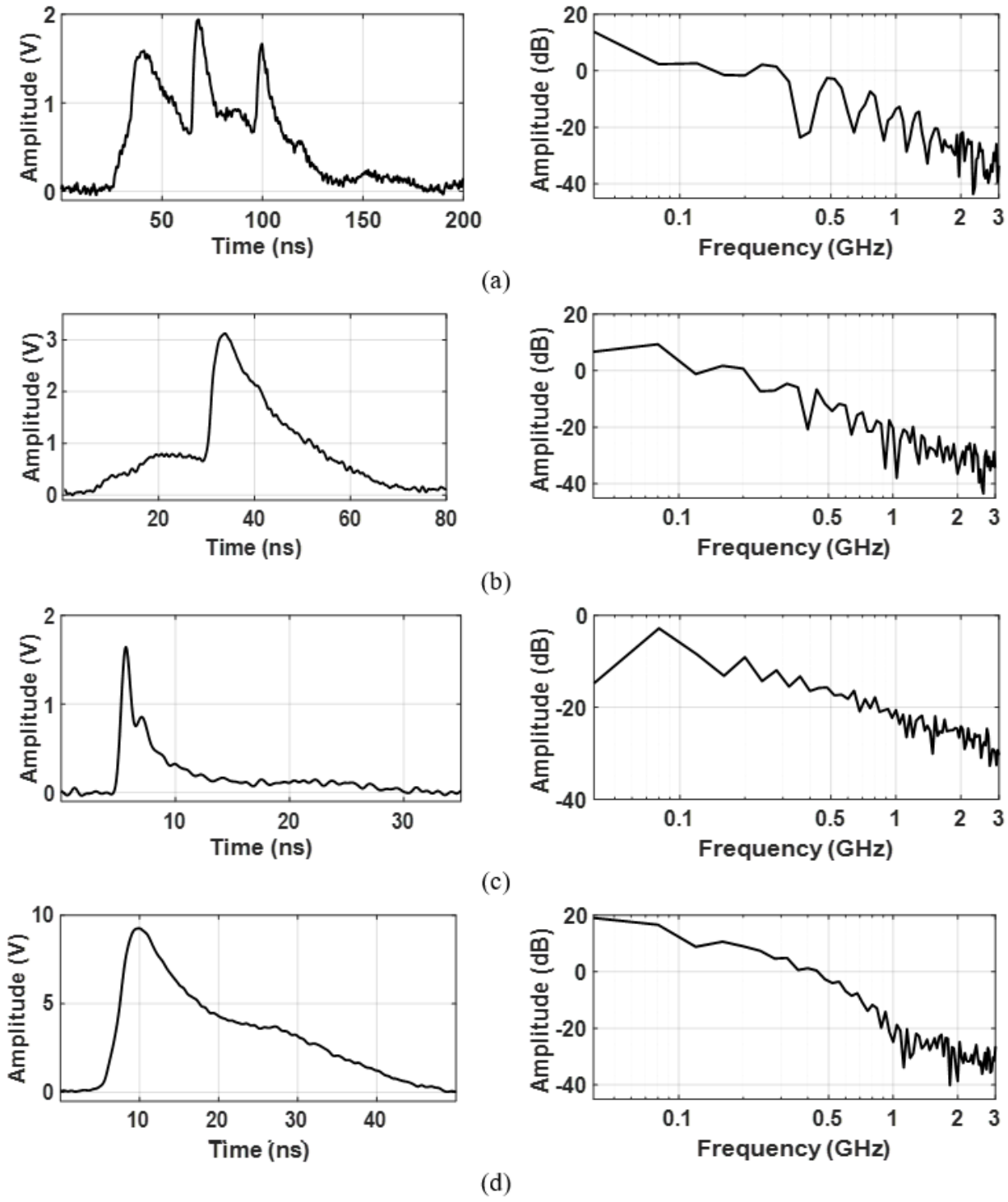

Figure 7.9 Examples of AC and DC floating potential discharge waveforms in both time and frequency domains are measured by the 50 Ω input channel of the oscilloscope. a-c) mostly common among AC and positive DC and rarely observed for negative DC, (d) more common among AC and negative DC.

More scattering among the floating potential discharge waveshapes under both AC and DC stresses than other types of PDs in this work. However, according to Figure 7.9a, the superposition of consequent unstable ionization channels is common among all AC and DC voltages with frequency spectrums more than -20 dB below 1.2 GHz. Figures 7.9b and 7.9c also show examples of floating potential discharge pulses comprised of slow and fast rise time. There were scattered among the amplitudes of these pulses and expectedly, the low amplitude pulses recorded under DC stresses. The captured signal in Figure 7.9d suggests a transition from a slow to fast rise time discharges, which is very similar to the transition among nonconductive streamer filament and conductive spark channel reported in [20]. However, the presented waveshapes in Figure 7.9b to 7.9d have frequency spectrums more than -20 dB below 0.7 GHz.

Furthermore, the inception voltage of floating potential discharge pulses under AC voltage stress is 4.1 kV. In the case of DC floating potential discharge pulses, because of quite a slow repetition rate (more than an hour), we used the ramp-up voltage method explained in section A (cavity discharge) to measure more floating potential discharge pulses. The results of floating potential discharge measurements under DC voltage stress presented a large variation among 5 kV to 13 kV for the inception of floating potential discharge pulses.

7.5 Summary

In this chapter, four common types of individual PD pulses, such as a cavity, surface, corona, and floating potential discharges, were investigated under AC and DC stress. First, to verify the performance of D-dot and B-dot sensors, their outputs were compared by the signal captured by the 50 Ω input channel of the oscilloscope. The comparison results of the D-dot and

B-dot sensor outputs with the reference PD pulse showed close agreements in both time and frequency domains for the cavity discharges. The findings suggest that the 50 Ω input channel of the oscilloscope, as well as the electromagnetic field non-conventional sensors (D-dot and B-dot), are suitable for studying pulse characteristics, including rising time, decay time, 50% pulse width, and 20% pulse width measured through transmission line where wave propagation characteristics are known. It can be used for investigating PD characteristics at the source and allow for further development of systems intended for onsite applications.

Also, another investigation was performed on the prepared PD sources to find their discharge mechanisms through analysis of some typical PD waveshapes in time and frequency domains. The discharge mechanism analysis presented various types of ionization processes, such as the fast rise and decay times, the products of photo-ionization (Streamer-like), and the slow rise and decay times that are products of gradual initiation electron avalanches (Townsend-like). In addition, some rhythmic pulses were products of superposition among multiple fast and slow unstable ionization mechanisms. Moreover, there was various type of waveshapes which only recorded under DC stresses which are emphasized the importance of DC PD measurement.

CHAPTER VIII

QUANTITATIVE ANALYSIS OF INDIVIDUAL PARTIAL DISCHARGE PULSES

8.1 Motivation

This Chapter targets to perform a quantitative study to extract meaningful information from the captured PD data. The results lead to finding methods to classify and distinguish various PD defects through their waveshapes. Moreover, as there is no limitation for utilizing the designed testbed and sensors in the AC application, we performed all the experiments for both AC and DC stresses. The AC individual PD pulse measurement enables us to compare the AC and DC PDs and classify the AC PDs according to their PD waveshapes instead of the well-known PRPD.

8.2 Time Domain Analysis

In this section, we quantify the time characteristics of the provided PD source waveforms. The quantified study compares the results of thousands of PD pulses were measured under AC, positive DC, and negative DC. The corresponding pulses were captured through all of the D-dot, B-dot, and 50 Ω channel of the oscilloscope to compare the performances of either of the sensors. To compare the results, the relative frequency histogram method, which represents the ratio of pulses within specific time characteristics, is selected. To quantify the PDs measured by the oscilloscope, we extracted the rise time (t_r), decay time(t_d), 50% pulse width ($t_{50\%}$), 20% pulse width ($t_{20\%}$), and the amplitude of each of the pulses according to the concepts introduced in Figure 2.16. Also, for clearer comparison, the histograms are plotted in lines instead of bar charts, and

some of those are log scaled to cover the scattered amplitude and time differences by some orders. Similarly, in the case of D-dot and B-dot sensors outputs quantification, we just extracted the introduced parameters in Figure 7.5 to find the trend of PDs changes under different voltage stresses. The corresponding parameters include Max and Min of each pulse and its first and second cycle length (T_1 and T_2).

8.2.1 Partial Discharge Pulses Measured by the 50 Ω Input channel of Oscilloscope

8.2.1.1 Rise Time

The histogram diagram of rise time characteristics of captured PD pulse under AC, DC(+), and DC(-) are presented in Figure 8.1. The blue, red and yellow color lines represents the AC, DC(+), and DC(-) results, respectively.

Figure 8.1a, which compares the t_r histogram of cavity discharge, presents a close agreement among the t_r of cavity discharges under AC, DC(+), and DC(-). t_r values shorter than 1 ns correspond to the Streamer-like and above 1 ns to Townsend-like discharges under both AC and DC stresses. The results of comparing Surface discharge pulses in Figure 8.1b suggest that most Surface discharge pulses were measured under AC stresses have t_r shorter than 1 ns. In contrast, values are scattered up to 40 ns for pulses were generated by DC(+) and DC(-) stresses. Also, the results of NCOD discharges in Figure 8.1c demonstrate that the t_r of pulses were generated under AC stresses is less than 5 ns while it is between 1 and 2 ns for DC(+)-induced pulses. In addition, the t_r values of DC(-) are divided into three groups of fast (2 to 4 ns), intermediate (10 to 20 ns), and slow (40 to 70 ns). Contrarily, the results of PCOD in Figure 8.1d show the values among 0.8 to 4 ns for AC-induced pulses, and 1.5 to 10.5 ns for DC(+) as well as three groups of fast (2 to 3 ns), intermediate (7 to 30 ns), and slow (50 to 80 ns) pulses under DC(-).

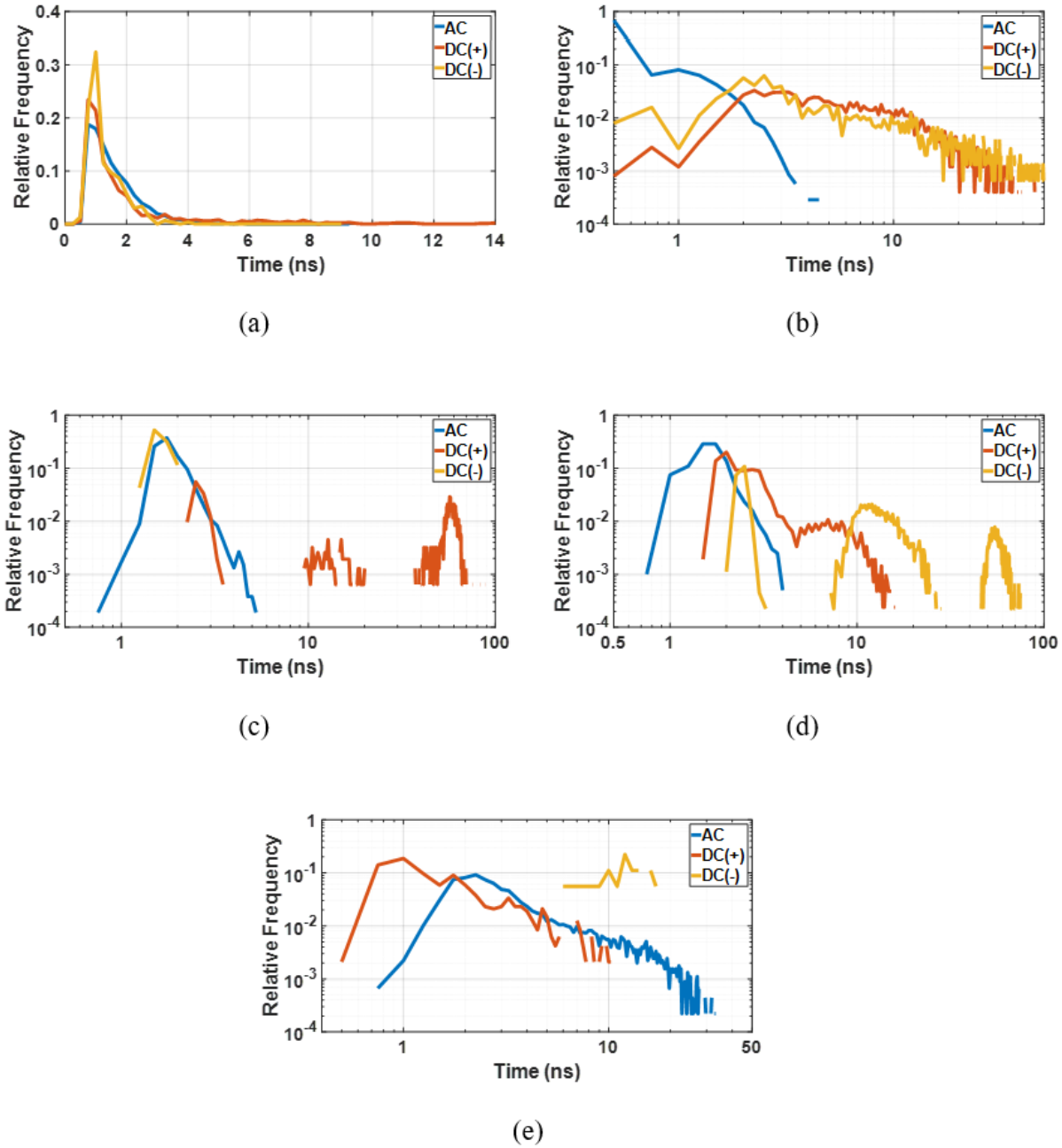

Figure 8.1 Comparison of rise time changes of various PD sources were measured by 50 Ω input channel of the oscilloscope. (a) cavity discharge, (b) surface discharge, (c) negative corona discharge, (d) positive corona discharge, (e) floating potential discharge.

Finally, the floating potential discharge results in Figure 1e show scattered data for both AC and DC(+)-induced pulses with the highest concentration of values lower than 5 ns. The results suggest that the t_r values of DC(+)-induced pulses are shorter than those of the AC-induced pulses. Also, DC(-) results show the distribution t_r between 6 and 17 ns. The rise time parameter results are summarized in Table 8.1 for ease on comparison of PD defects.

Table 8.1 Rise time (in ns) parameters of PD sources were measured by 50 Ω input channel of oscilloscope under both AC and DC voltage stresses.

	Cavity discharge	Surface discharge	Negative corona discharge	Positive corona discharge	Floating potential discharge
AC	0.5 – 4	0.5 - 5	0.8 – 5.5	2 - 3	1 - 15
Positive DC	0.5 – 3	0.5 - 20	2 – 4 10 – 20 40 - 80	1.5 - 17	0.5 - 10
Negative DC	0.5 – 3	0.5 - 20	1.2 - 2	2 – 3 8 – 30 45 - 80	6 - 17

8.2.1.2 Decay Time

Figure 8.2 denotes the results of decay time changes in the histogram diagram for all captured PD pulses under AC, DC(+), and DC(-). The blue, red, and yellow color lines represent the AC, DC(+), and DC(-) results. According to Figure 8.2a, the t_d distribution of cavity discharges under AC ranges up to 20 ns, but are mostly concentrated around 3 to 5 ns. Also, both DC(+) and DC(-) results represent less than 10 ns. Therefore, it is concluded that fast ionization processes accompany most of the recorded cavity discharge pulses. Similarly, the results of Surface discharges in Figure 8.2b show a range of up to 20 ns for the AC-induced pulses with t_d being

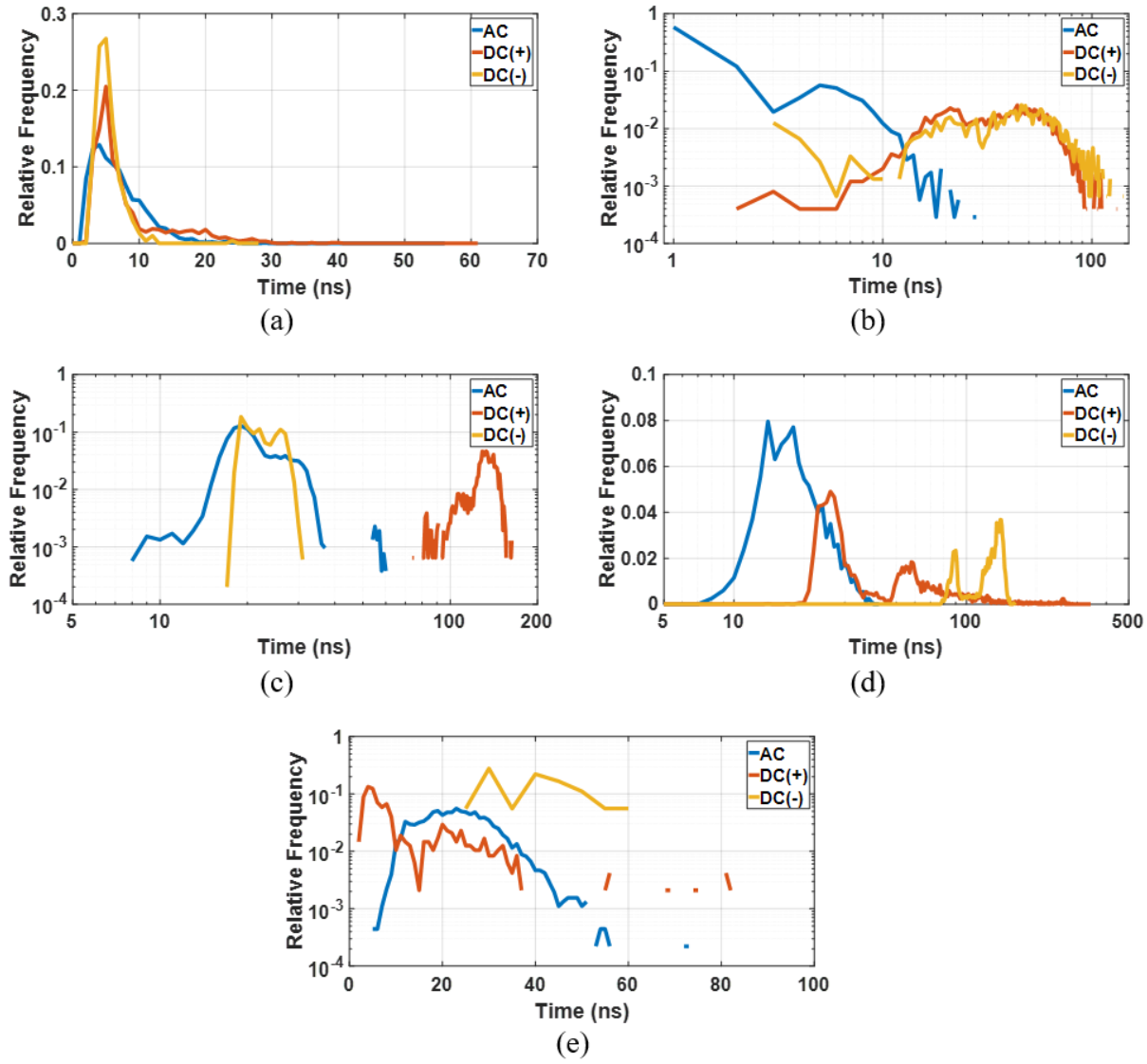

Figure 8.2 Comparison of decay time changes of various PD sources were measured by the 50 Ω input channel of the oscilloscope. (a) cavity discharge, (b) surface discharge, (c) negative corona discharge, (d) positive corona discharge, (e) floating potential discharge.

mostly shorter than 3 ns. In contrast, the Surface discharge pulses were generated under both DC(+) and DC(-) have t_d distributed between 10 and 100 ns. The results of NCOD in Figure 8.2c show two groups of data for AC-induced pulses less than 40 ns, which are the majority pulses and other around 60 ns. The DC(+) data shows pulses are scattered between 80 and 150 ns while the

DC(-)-induced pulses are concentrated around 17 to 30 ns. Contrarily, the PCOD results in Figure8.2d display most AC pulses are distributed between 30 and 60 ns. The DC(+) data are widely scattered up to 300 ns while the DC(-) pulses are mostly around 80 to 150 ns. Lastly, the results of measured floating potential discharges in Figure 8.2e demonstrate the floating potential discharge pulses were generated under AC stresses have t_d below 40 ns that are concentrated around 20 ns. Similarly, DC (+)-induced pulses represent fast decay pulses that are mostly shorter than 10 ns. The results of DC(-)-induced pulses show t_d distributed between 25 and 60 ns. Also, the decay time parameter results are summarized in Table 8.2.

Table 8.2 Decay time (in ns) parameters of PD sources were measured by 50 Ω input channel of oscilloscope under both AC and DC voltage stresses.

	Cavity discharge	Surface discharge	Negative corona discharge	Positive corona discharge	Floating potential discharge
AC	1 - 30	1 - 30	8 - 60	30 - 60	5 - 60
Positive DC	2 - 10	2 - 100	80 - 150	20 - 300	1 - 40
Negative DC	2 - 10	3 - 100	18 - 30	80 - 200	27 - 65

8.2.1.3 Pulse Width of 20% Level

The results of 20% pulse width time characteristics of captured PD pulse under AC, DC(+), and DC(-) are presented in Figure 8.3. The blue, red and yellow color lines represents the AC, DC(+), and DC(-) results, respectively.

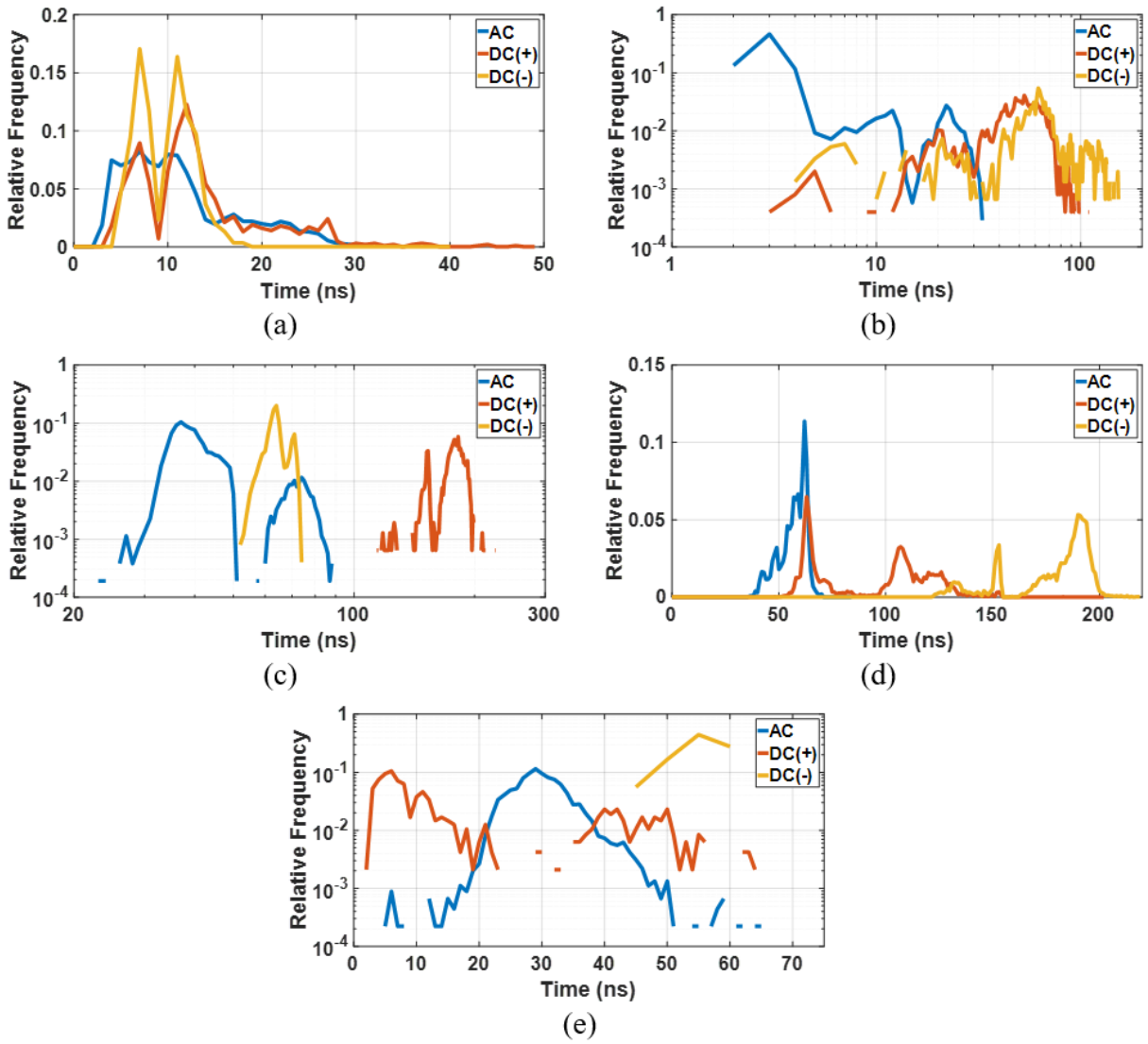

Figure 8.3 Compare 20% pulse width time changes of various PD sources were measured by the 50 Ω input channel of the oscilloscope. (a) cavity discharge, (b) surface discharge, (c) negative corona discharge, (d) positive corona discharge, (e) floating potential discharge.

According to Figure 8.3a, the DC-induced pulses are divided into two groups with a higher concentration around 8 and 10.5 ns while the AC-induced pulses are evenly distributed in this range. Also, some pulses are distributed between 15 ns and 30 ns that are common among AC and DC(+). The results suggest that the cavity discharge pulses in AC are mostly the Streamer-like

discharges. The results of Surface discharge pulses in Figure 8.3b represent faster pulses in AC than in DC. In AC, most $t_{20\%}$ are shorter than 5 ns, although there are some extended up to 30 ns. Also, DC(+) and DC(-) results show a widely scattered pattern up to 100 ns, which are likely caused by the superposition of pulses. Figure 8.3c shows the NCOD pulses under AC split into two groups ranging from 25 to 50 ns and 60 to 90 ns. Also, there is a wide scattering for DC(+) NCOD pulses that are distributed between 100 to 250 ns. In contrast, DC(-) pulses behave similarly to that of AC and have $t_{20\%}$ in the range of 50 to 75 ns. The histogram data of Figure 8.3d shows PCOD results under AC have pulse widths around 65 to 85 ns. The DC(+) results show a wide distribution of pulses between 50 and 150 ns which are divided into two groups, around 70 ns, and 110 ns. The obtained results of floating potential discharge in Figure 8.3e show that the AC-induced pulse has a longer $t_{20\%}$ than DC(+)-induced pulses. The widths of the AC-induced pulse are scattered between 10 and 50 ns, while those of the DC(+)-induced pulses are below 20 ns. The DC(-) pulses represent relatively longer pulses on the range of 45 to 80 ns. The pulse width parameter results are summarized in Table 8.3.

Table 8.3 Pulse width (in ns) parameters of PD sources were measured by 50 Ω input channel of oscilloscope under both AC and DC voltage stresses.

	Cavity discharge	Surface discharge	Negative corona discharge	Positive corona discharge	Floating potential discharge
AC	2 - 30	2 - 35	25 - 90	40 - 70	5 - 65
Positive DC	3 - 30	3 – 6 9 - 150	110 - 225	50 - 160	2 – 20 35 - 65
Negative DC	4 - 18	3 - 100	50 -75	140 - 200	45 - 60

8.2.1.4 Amplitude

The amplitude distribution of captured PD pulses are shown in Figure 8.4. The blue, red and yellow color lines represents the AC, DC(+), and DC(-) results, respectively.

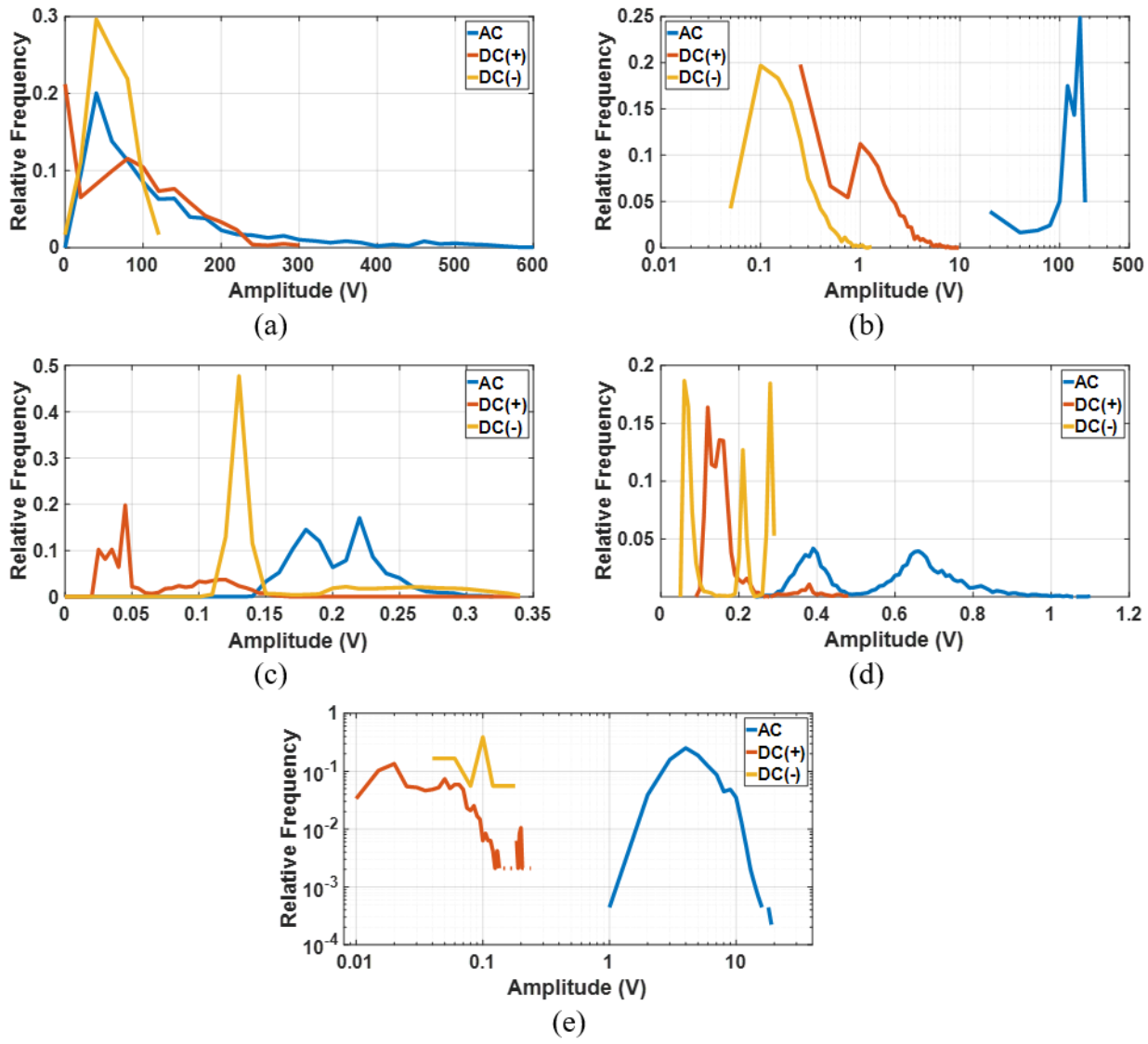

Figure 8.4 Comparison of amplitude of various PD sources were measured by the 50 Ω input channel of the oscilloscope. (a) cavity discharge, (b) surface discharge, (c) negative corona discharge, (d) positive corona discharge, (e) floating potential discharge.

Due to the Figure 8.4a, the cavity pulses are accompanied with strong discharges up to 600 V. However, most of the pulses occurred with discharge amplitudes below 250 V. Similarly, among the pulses captured under DC(+) stresses, we found the discharges with 300 V amplitude which mostly concentrated below 250 V. the DC(-) pulses are also represented with strong pulses with amplitudes below 120 V which are mostly occurred with 50 V peaks. It is impossible to confidently determine the discharge mechanisms of PD defects according to the PD pulse amplitudes, but generally, Streamer-like discharges supplemented with higher amplitude discharges. It is actually in agreement with previous results were obtained by analyzing cavity discharge time characteristics in this work. The results of Surface discharge pulses amplitudes in Figure 8.4b denote a significant difference among the amplitude of AC and DC pulses by some orders. The surface discharge pulses in AC include PD pulses with strong amplitudes around 150 V. In contract, the DC(+) and DC(-) voltages generate PD pulses up to 10 V and 1 V which are mostly concentrated around 0.5 V and 0.1 V, respectively.

Moreover, the expressed results in Figure 8.4c and 8.4d illustrate the amplitude of corona discharge pulses slightly differ between AC and DC stresses. In NCOD, the AC results in PDs with amplitudes between 150 mV and 300 mV. Similarly, DC(-) causes the corona discharges around 130 mV while the DC(+) generates NCODs with 50 mV strengths. Moreover, in the case of PCODs, stronger corona discharges have been observed rather than NCOD. The pulses captured under AC occurred mostly around 400 mV and 700 mV. Contrarily, the DC(+) pulses are detected with amplitudes mostly about 150 mV and DC (-) pulses were scattered between 50 mV to 250 mV. A reason for such wide scattering in pulse measured under DC(-) is the presented superimposed pulses in Figure 7.8c. Lastly, the results of floating potential discharges in Figure 8.4e confirms the differences among the strength of AC and DC PD pulses. The AC voltage

provides the floating particle discharge pulses with amplitudes between 1V to 20V, which are highly occurred with 4V. In the case of DC PD, pulses with amplitudes lower 300mv are captured. Table 8.4 is summarized the amplitude of PD pulses were extracted from Figure 8.13 under both AC and DC voltage stresses.

Table 8.4 Amplitude (in V) values of PD sources were measured by 50 Ω input channel of oscilloscope under both AC and DC voltage stresses.

	Cavity discharge	Surface discharge	Negative corona discharge	Positive corona discharge	Floating potential discharge
AC	< 600	20 - 200	0.1 – 0.3	0.3 - 1	1 -20
Positive DC	< 300	0.25 - 10	0.1 – 0.35	0.1 – 0.4	0.01 – 0.3
Negative DC	< 120	0.05 – 1.5	0.02 – 0.15	0.05 – 0.3	0.04 – 0.2

8.2.2 Partial Discharge Pulses Measured by D-dot Sensor

8.2.2.1 Positive Peak Amplitude (Maximum)

The histogram diagram of positive peak amplitude of captured PD pulse with D-dot sensor under AC, DC(+), and DC(-) are shown in Figure 8.5. The blue, red and yellow color lines represents the AC, DC(+), and DC(-) results, respectively. Similar to the obtained results from the 50 Ω input channel of the oscilloscope in Figure 8.4, D-dot sensor outputs show the same trends. In cavity and corona discharges, there are no large differences between the intensities of both AC and DC induced pulses. Except for those AC PD pulses in Figure 8.5a, which refers to strong streamer-like discharges. Contrarily, the surface and floating potential discharge pulses in AC have higher amplitudes than those of DC. Table 8.5 summarizes the positive peak amplitude of PD pulses extracted from Figure 8.5 under both AC and DC voltage stresses. It should be noted that we just provide the ranges with more than 1% of relative frequency.

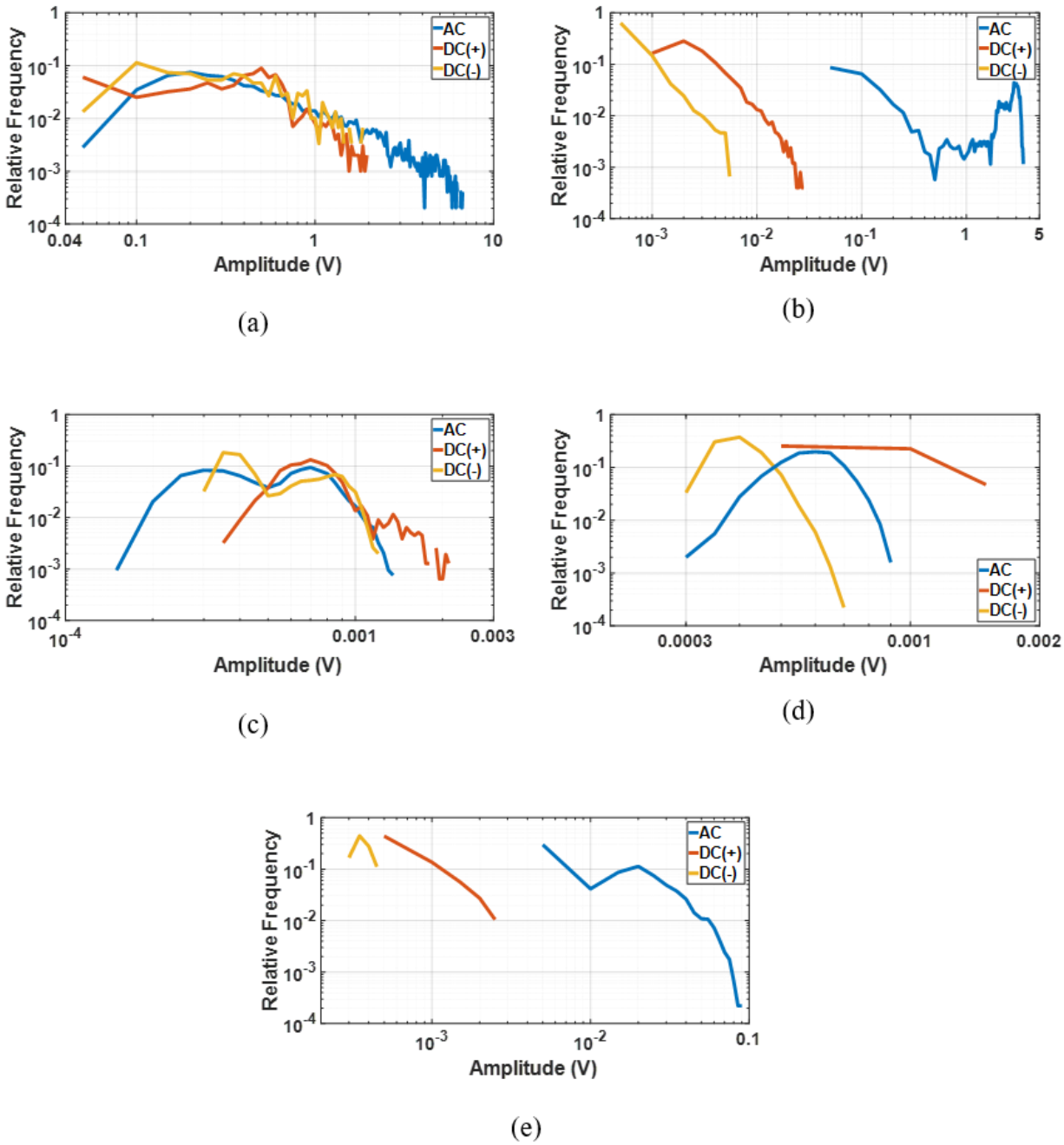

Figure 8.5 Comparison of the positive peak amplitude of various PD sources were measured by the D-dot sensor. (a) cavity discharge, (b) surface discharge, (c) negative corona discharge, (d) positive corona discharge, (e) floating potential discharge.

Table 8.5 Positive Peak Amplitude (in V) values of PD sources were measured by D-dot sensor under both AC and DC voltage stresses.

	Cavity discharge	Surface discharge	Negative corona discharge	Positive corona discharge	Floating potential discharge
AC	0.07 - 1	0.05 – 0.25 2 - 3.5	< 0.001	0.0003 – 0.001	0.005 – 0.06
Positive DC	0.05 – 0.9	0.001 - 0.012	< 0.001	< 0.0015	0.0005 – 0.0025
Negative DC	0.05 – 1.2	< 0.003	< 0.001	< 0.0007	< 0.00045

- The table data shows the ranges with more than 1% relative frequency.

8.2.2.2 Negative Peak Amplitude (Minimum)

The results of the negative peak amplitude investigation of induced PD pulses with D-dot sensor under AC, DC(+), and DC(-) are shown in Figure 8.6. The blue, red, and yellow color lines represent the AC, DC(+), and DC(-) results. As seen in the figure, the surface and floating particle PD pulses in AC result in a higher negative peak than DC pulses. Also, there is no significant discrimination among cavity and corona discharges. There are some cavity discharges with the lower relative frequency with amplitudes about -10 V, which refers to those strong Streamer-like discharges which are observed in reference results, too.

Table 8.6 Negative Peak Amplitude (value in V) values of PD sources were measured by D-dot sensor under both AC and DC voltage stresses.

	Cavity discharge	Surface discharge	Negative corona discharge	Positive corona discharge	Floating potential discharge
AC	0.07 - 1	0.07 – 0.2 1.5 - 3	< 0.0018	<0.003	0.004 – 0.03
Positive DC	0.07 – 0.8	0.001 – 0.008	< 0.0007	< 0.0012	< 0.0009
Negative DC	0.2 - 2	0.001 – 0.006	< 0.0035 < 0.0012	< 0.0008	< 0.001

- The table data shows the ranges with more than 1% relative frequency.

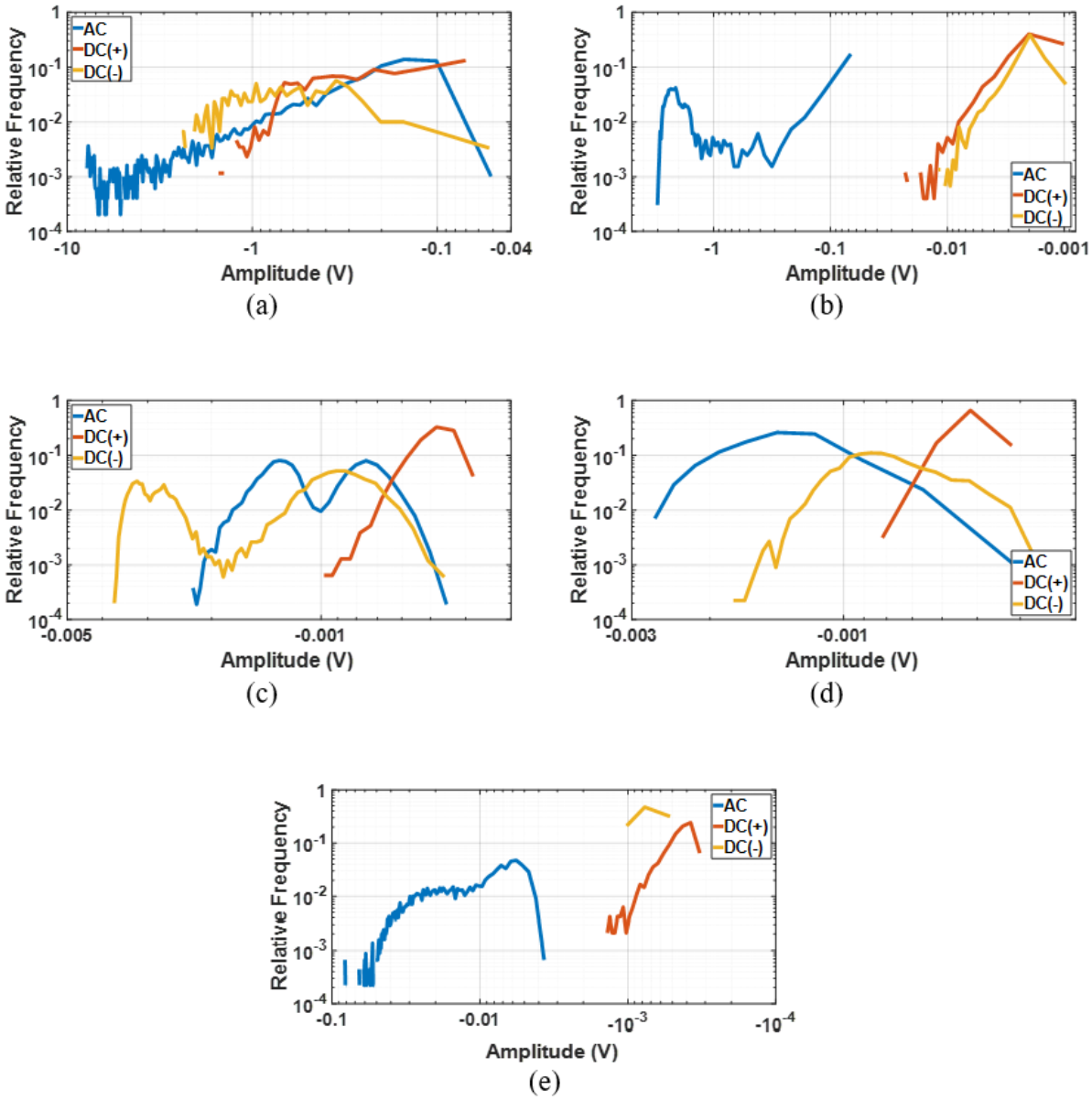

Figure 8.6 Comparison of the negative peak amplitude of various PD sources were measured by the D-dot sensor. (a) cavity discharge, (b) surface discharge, (c) negative corona discharge, (d) positive corona discharge, (e) floating potential discharge.

In addition, Table 8.6 summarizes the distribution of negative peak amplitude of individual PD pulses were recorded under AC and DC voltage stresses. It should be noted we just provide the ranges with more than 1% of relative frequency.

8.2.2.3 First Peak Length (T_1)

The histogram results of T_1 value (time length of first peak in sensor's output) of PD signals were measured by the D-dot sensor under AC and DC voltage stresses are demonstrated in Figure 8.7. The blue, red and yellow color lines represents the AC, DC(+), and DC(-) results, respectively.

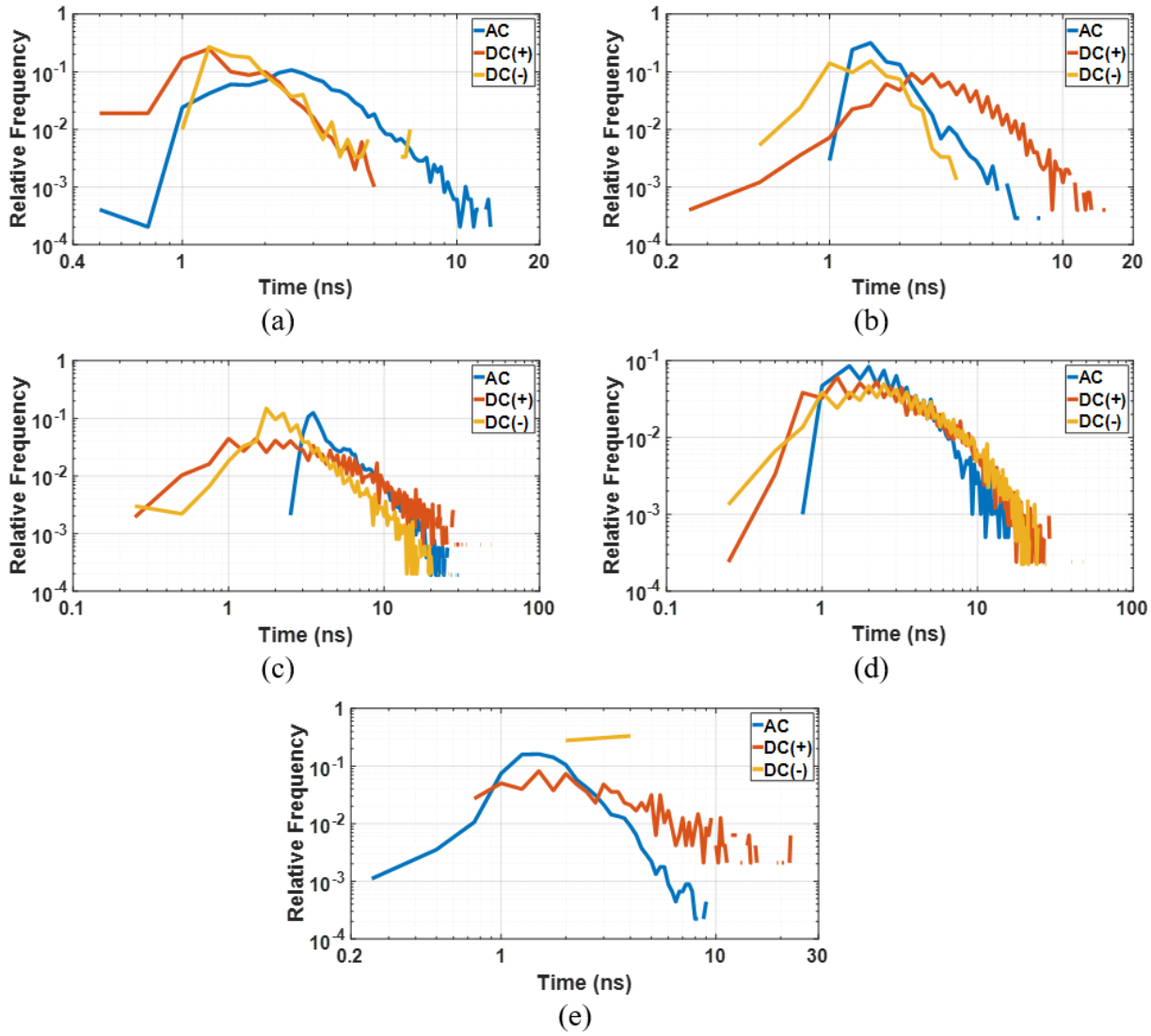

Figure 8.7 Comparison of the T_1 value of various PD sources were measured by the D-dot sensor. a) cavity discharge, (b) surface discharge, (c) negative corona discharge, (d) positive corona discharge, (e) floating potential discharge.

In general, the T_1 can be assumed in equal to rising time in case of time characteristics of double exponential waveforms, which are measured by the 50 Ω input channel of the oscilloscope. In other words, it determines the rate of the ionization process. So, the trend of T_1 changes for most of the PD sources is such as the rise time trend in Figure 8.1. There are some differences in the case of corona discharges that are related to the frequency spectrum of these pulses and the low SNR value of the D-dot sensor on those ranges. However, there is still an acceptable correlation between the trends of individual PD pulses were measured by D-dot and 50 Ω input channel of the oscilloscope. Table 8.7 summarizes the scattering of the individual PD pulses' T_1 values under AC and DC stresses. It should be noted we just provide the ranges with more than 1% of relative frequency.

Table 8.7 T_1 (in ns) values of PD sources measured by D-dot sensor under both AC and DC voltage stresses.

	Cavity discharge	Surface discharge	Negative corona discharge	Positive corona discharge	Floating potential discharge
AC	0.9 - 5	1 - 3	2.7 - 9	0.9 - 7	0.75 - 4
Positive DC	0.5 - 3	1 - 7	0.5 - 9	0.6 - 9	0.75 - 10
Negative DC	1 - 3	0.6 – 2.5	0.7 - 5	0.6 - 9	2 - 4

- The table data shows the ranges with more than 1% relative frequency.

8.2.2.4 Second Peak Length (T_2)

The T_2 value (time length of the second peak in the sensor's output) of induced PD pulses under both AC and DC stresses are shown in Figure 8.8. The blue, red, and yellow color lines represent the AC, DC(+), and DC(-) results. The time T2 is assumed as the length of the decreasing rate of the ionization process within the PD source.

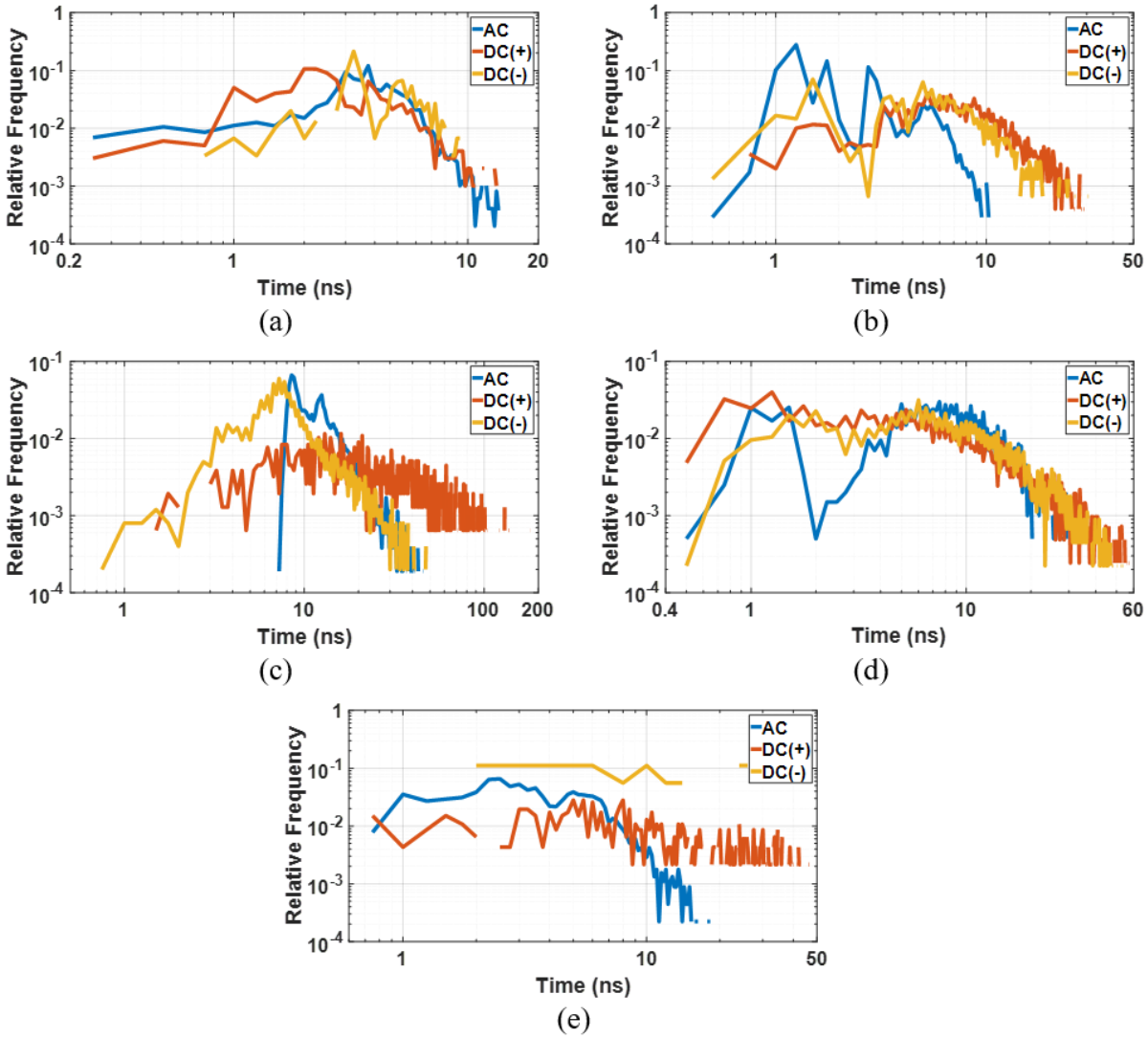

Figure 8.8 Comparison of the T_2 value of various PD sources were measured by the D-dot sensor. a) cavity discharge, (b) surface discharge, (c) negative corona discharge, (d) positive corona discharge, (e) floating potential discharge.

According to Figure 8.8, T_2 includes the values of less than 1 ns in most types of PDs. It is referring to the types of inducing PD waveshapes in which the ionization processes are resulted by electrons drops suddenly, and the discharge current were continued by drifting of ions. Similarly, T_2 can be considered equal with a 50% pulse width of a signal and, in some cases, the decay time

of the PD signal. Table 8.8 summarizes the T_2 of PD pulses were extracted from Figure 8.8 under both AC and DC voltage stresses.

Table 8.8 T_2 (in ns) values of PD sources were measured by D-dot sensor under both AC and DC voltage stresses.

	Cavity discharge	Surface discharge	Negative corona discharge	Positive corona discharge	Floating potential discharge
AC	0.4 - 7	0.85 - 6.5	8 - 17	0.9 – 1.7 4.5 - 12	0.8 - 8
Positive DC	0.8 - 6	1.2 - 12	-----	0.6 - 9	0.8 - 10
Negative DC	1.5 - 8	0.85 – 10	3 - 10	1 - 10	2 - 15

- The table data shows the ranges with more than 1% relative frequency.

8.4.3 Partial Discharge Pulses Measured by B-dot Sensor

8.4.3.1 Positive Peak Amplitude (Maximum)

The histogram diagram of positive peak amplitude of captured PD pulse with B-dot sensor under AC, DC(+), and DC(-) are shown in Figure 8.9. The blue, red and yellow color lines represents the AC, DC(+), and DC(-) results, respectively.

As seen in Figure 8.9, the B-dot sensor performance in the case of cavity and surface discharges are accompanied by the stronger discharges is better than corona and floating potential discharges. The analysis of cavity discharges in Figure 8.9a denotes the same positive peak amplitude pulses for AC and DC pulses and those intensive streamer-like discharges, which are only observed under AC stresses. Moreover, in the case of surface discharge in Figure 8.9b, the AC induced pulses are distinguishable from those of DC. However, the B-dot sensor performs with low sensitivity in the case of corona discharges, and we only were enabled to distinguish AC positive corona discharges from those of noises. As we explain later, this issue is related to the

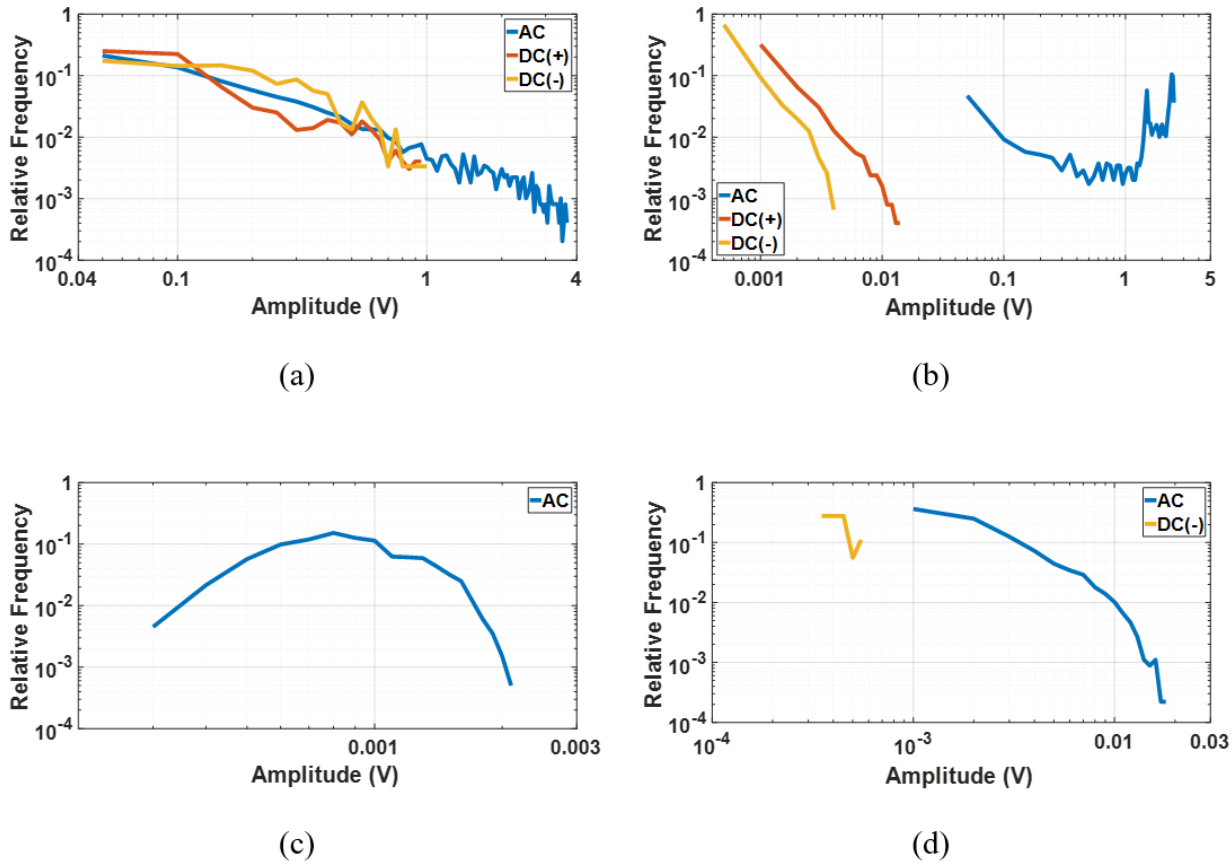

Figure 8.9 Comparison of the positive peak amplitude of various PD sources were measured by the B-dot sensor. (a) cavity discharge, (b) surface discharge, (c) positive corona discharge, (d) floating potential discharge.

frequency range of corona discharges where locate in the spectrums that the designed B-dot sensor has low SNR (see Figure 6.16b). Similarly, in floating potential discharge, it was impossible to distinguish DC(+) pulses from those of disturbances. By the way, the resulted data confirms the stronger PD discharges in AC rather than DC. The distribution range of positive peak amplitude of PD pulses were captured by the B-dot sensor under AC and DC stresses are presented in Table 8.9. It should be noted we just provide the ranges with more than 1% of relative frequency.

Table 8.9 Positive Peak Amplitude (in V) values of PD sources were measured by B-dot sensor under both AC and DC voltage stresses.

	Cavity discharge	Surface discharge	Negative corona discharge	Positive corona discharge	Floating potential discharge
AC	0.05 – 0.7	0.05 – 0.1 1.5 – 2.5	-------	< 0.002	0.001 – 0.01
Positive DC	0.05 – 0.6	0.001 – 0.005	-------	-------	-------
Negative DC	0.05 – 0.6	< 0.0025	-------	-------	< 0.0006

- The table data shows the ranges with more than 1% relative frequency.

8.4.3.2 Negative Peak Amplitude (Minimum)

The histogram results of negative peak amplitude of B-dot outputs in case of individual PD pulse measurement under AC and DC voltage stresses are demonstrated in Figure 8.10. in this figure, the blue, red and yellow color lines represents the AC, DC(+), and DC(-) results, respectively.

Table 8.10 Negative Peak Amplitude (*absolute value* in V) values of PD sources were measured by B-dot sensor under both AC and DC voltage stresses.

	Cavity discharge	Surface discharge	Negative corona discharge	Positive corona discharge	Floating potential discharge
AC	0.04 – 0.6	0.07 – 0.2 1 - 2	-------	<0.0014	0.001 – 0.007
Positive DC	0.1 – 0.6	0.001 – 0.006	-------	-------	-------
Negative DC	0.07 – 0.8	< 0.004	-------	-------	< 0.0007

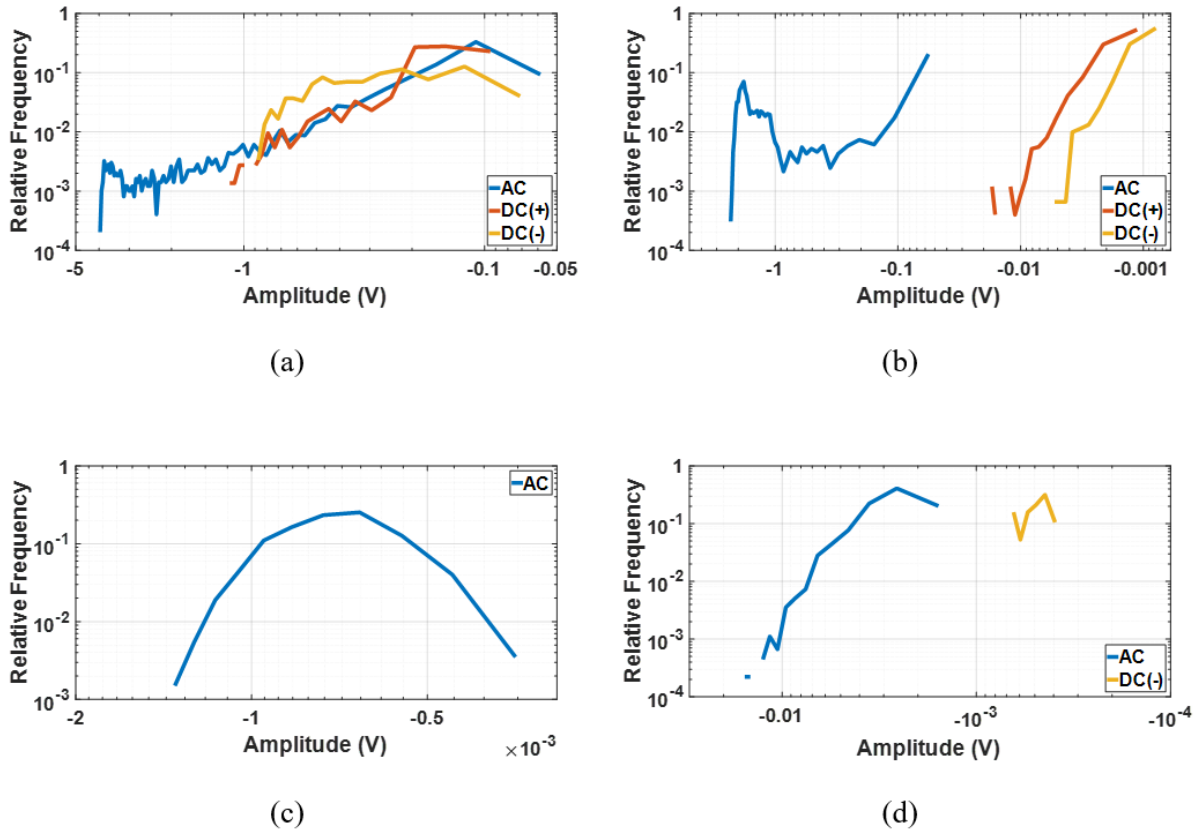

Figure 8.10 Comparison of the negative peak amplitude of various PD sources were measured by the B-dot sensor. (a) cavity discharge, (b) surface discharge, (c) positive corona discharge, (d) floating potential discharge

Due to Figure 8.10a, the cavity discharge provides the individual pulses with negative peaks about -4 V that are related to the strong Streamer-like discharges. For the individual PD pulses with a negative peak of less than -1 V, there is no difference between AC and DC induced PD pulses. The summary of the results in Figure 8.10 is shown in Table 8.10. It should be noted we just provide the ranges with more than 1% of relative frequency.

8.4.3.3 First Peak Length (T_1)

The histogram results of T_1 value of individual PD pulses were captured by B-dot sensor under AC and DC stresses are demonstrated in Figure 8.7. The blue, red and yellow color lines represents the AC, DC(+), and DC(-) results, respectively.

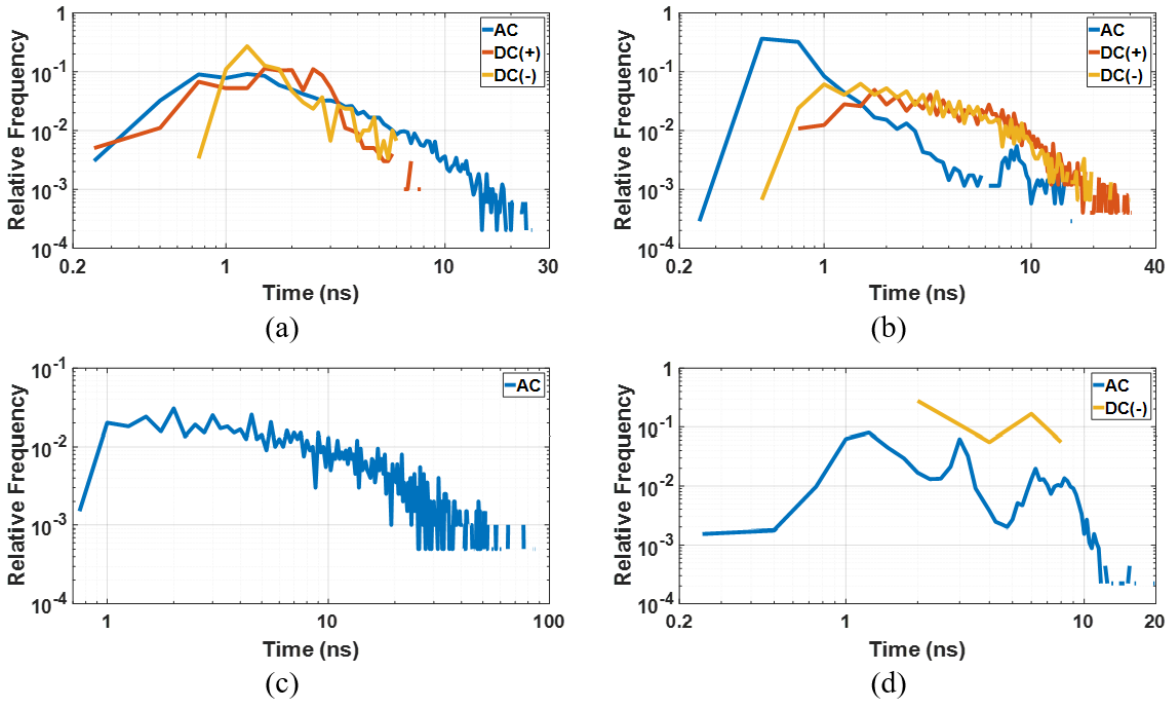

Figure 8.11 Comparison of the T_1 value of various PD sources were measured by the B-dot sensor. a) cavity discharge, (b) surface discharge, (c) positive corona discharge, (d) floating potential discharge.

As seen in Figure 8.11, there are some PD pulses by T1 values below 1 ns, were captured by B-dot sensors like those were captured by the D-dot sensor. The mentioned phenomenon is common among all cavity, surface, and floating potential discharges. According to Figure 8.11a, the DC(+) pulses are included in some fast ionized pulse during cavity discharge measurement. Similarly, the captured surface discharge pulses under DC(-) confirms the existence of these

pulses. The T_1 parameter results of the B-dot sensor are summarized in Table 8.11 for ease of comparison of PD defects. It should be noted we just provide the ranges with more than 1% of relative frequency.

Table 8.11 T_1 (in ns) values of PD sources were measured by B-dot sensor under both AC and DC voltage stresses.

	Cavity discharge	Surface discharge	Negative corona discharge	Positive corona discharge	Floating potential discharge
AC	0.35 - 6	0.35 – 3	-------	0.9 - 10	0.75 - 9
Positive DC	0.4 – 3.5	0.8 - 9	-------	-------	-------
Negative DC	0.8 - 4	0.7 – 7	-------	-------	2 - 8

- The table data shows the ranges with more than 1% relative frequency.

8.4.3.4 Second Peak Length (T_2)

Figure 8.12 denotes the results of T_2 changes in the histogram diagram for all captured PD pulses under AC, DC(+), and DC(-). The blue, red, and yellow color lines represent the AC, DC(+), and DC(-) results.

As shown in Figure 8.12, there is a good correlation among the T_2 parameter of cavity discharge pulses are recorded under both AC and DC stresses. Contrarily, in the case of surface discharge, the PD pulses in DC have longer T_2 parameter respect to the AC pulses. In Figure 8.12d, the T2 of AC floating potential discharges are scattered widely up to 75 ns while the DC (-) pulses are concentrated around 3 ns and 10 ns. The T_2 parameter results of the B-dot sensor are summarized in Table 8.12 for ease of comparison of PD defects. It should be noted we just provide the ranges with more than 1% of relative frequency.

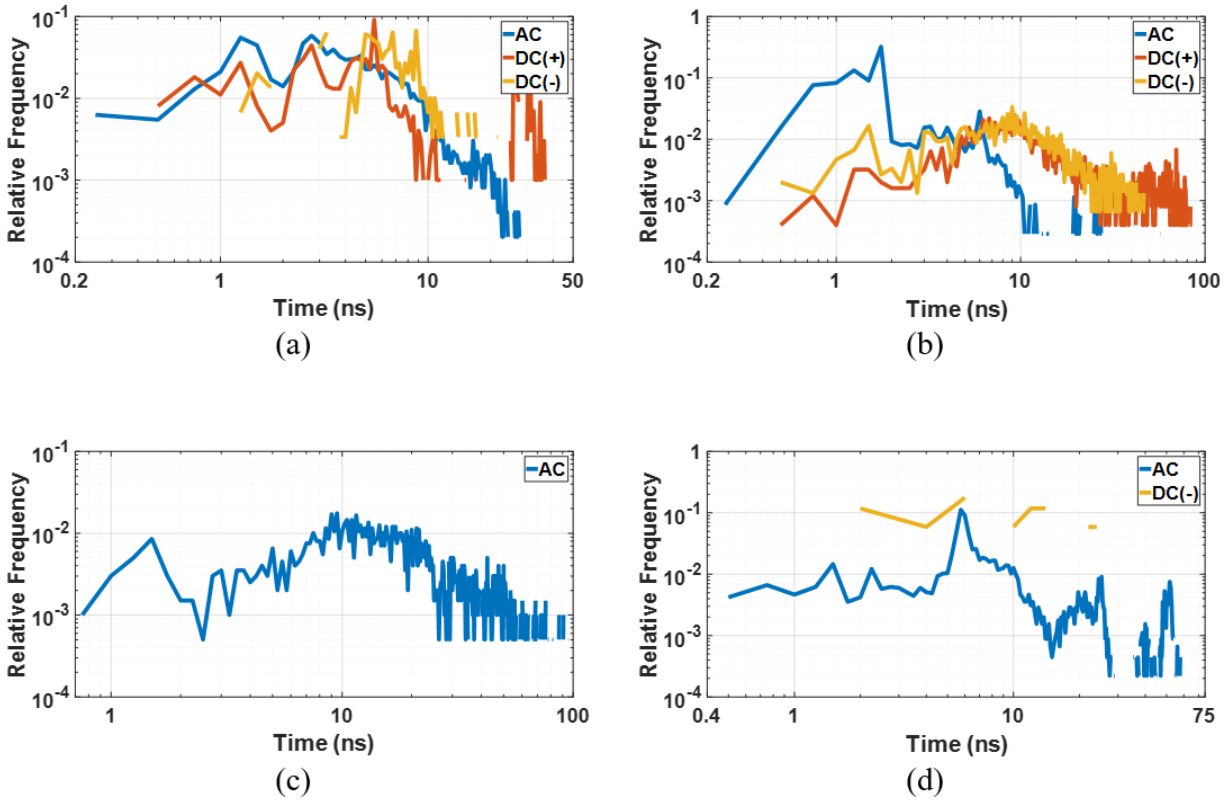

Figure 8.12 Comparison of the T2 value of various PD sources were measured by the D-dot sensor. a) cavity discharge, (b) surface discharge, (c) positive corona discharge, (e) floating potential discharge.

Table 8.12 T_2 (in ns) values of PD sources were measured by B-dot sensor under both AC and DC voltage stresses.

	Cavity discharge	Surface discharge	Negative corona discharge	Positive corona discharge	Floating potential discharge
AC	0.65 - 10	0.45 – 6.5	-------	8 - 20	5 - 10
Positive DC	0.5 – 6.5	5 - 11	-------	-------	-------
Negative DC	1.5 - 12	3 - 12	-------	-------	2 – 6 10 - 15

- The table data shows the ranges with more than 1% relative frequency.

8.3 Frequency Domain Analysis

The frequency spectrum analysis or FFT analysis of presented PD waveshapes are shown in Figures 8.13 to 8.15, separately, for all three sensors. The presented frequency spectrums include the average of all recorded signals for each type of PD in dB. The results of the FFT analysis on the individual PD pulses were captured by the 50 Ω input channel of the oscilloscope is shown in Figure 8.13.

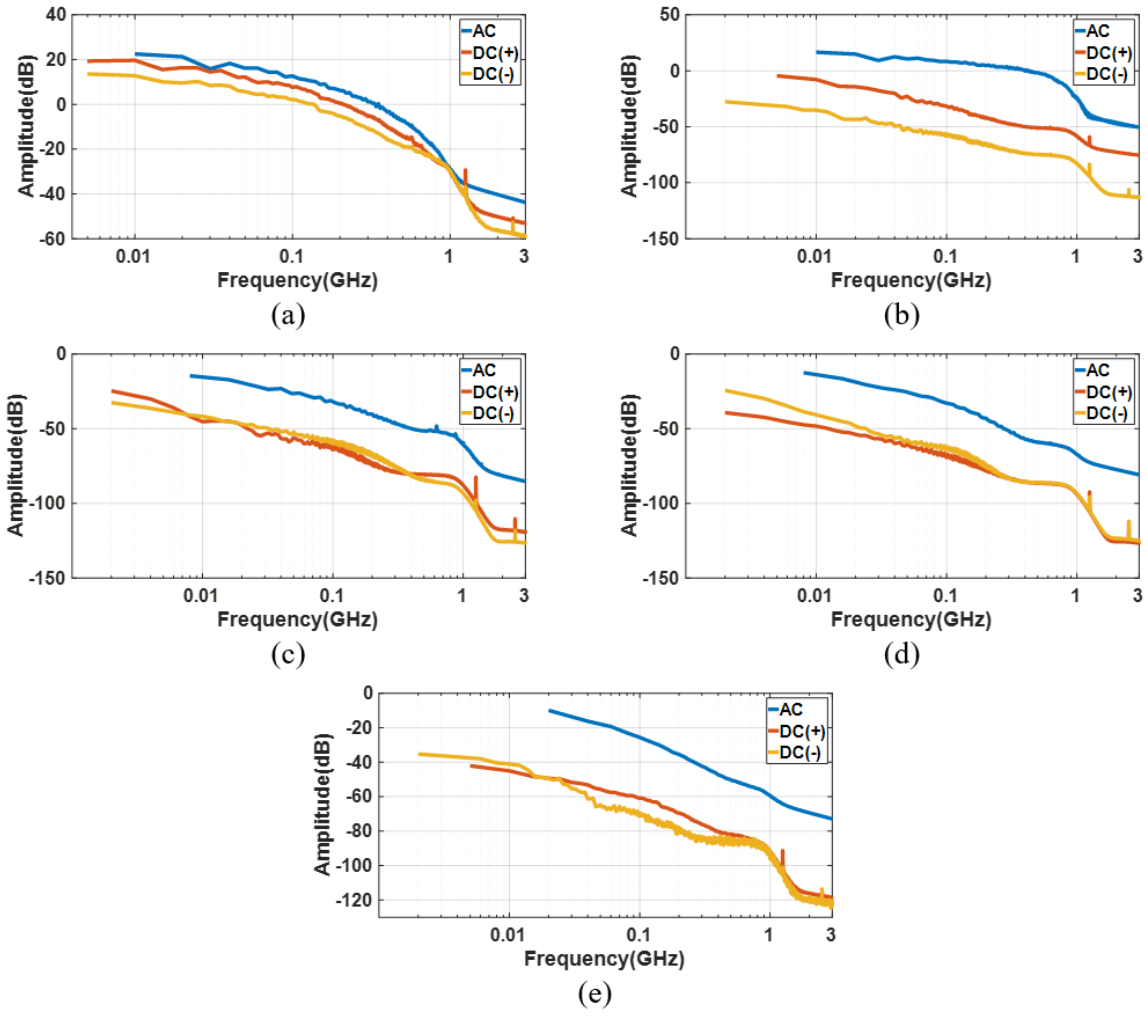

Figure 8.13 The frequency spectrum of individual PD pulses were measured with a 50 Ω input channel of oscilloscope under AC and DC voltage stresses. (a) cavity discharge, (b) surface discharge, (c) negative corona discharge, (d) positive corona discharge, (e) floating potential discharge.

The results depict AC PD pulses have a higher amplitude of respect to the DC-induced pulses. According to Figure 8.13a, the induced cavity discharge pulses under both AC and DC stresses have a relative frequency amplitude. Also, there is about 50 dB difference between the amplitude of cavity discharge pulses between 10 kHz to 1 GHz. In the case of Surface discharge PD, the amplitude of the frequency spectrum drop by 40 dB for both AC and DC voltage stresses. Also, it should be mentioned that the DC high frequency of Surface discharge PD pulse has a very low value below -40 dB, which complies with waveshapes are presented in Figures 8.7c and 8.7d. The outcomes of Figure 8.13c and 8.13d represent the AC -induced corona PDs have stronger high frequency components than DC-induced PD. In addition, it can be concluded that both polarities of DC have a similar frequency spectrum by 3 GHz.

Similarly, in a floating potential discharge pulse, the AC-induced pulse has a stronger frequency amplitude. Moreover, there is no difference between the frequency responses of DC(+) and DC(-) stresses. However, it is generally concluded from Figure 8.13 that DC PD pulses have lower amplitudes and frequency components concerning AC-induced PD pulses.

In addition, the results of the D-do sensor output FFT analysis are demonstrated in Figure 8.14. Generally, trends of recorded PD pulses in the frequency domain by D-dot sensors show close agreement with 50 Ω input channel of the oscilloscope. According to Figure 8.14a, the cavity discharge pulses under both AC and DC voltage stresses have equal amplitudes (i.e., a bit lower than pulses were measured by 50 Ω input channel of the oscilloscope) for long-range of frequencies. The recorded data shows all AC and DC induced pulses have amplitudes above -40 dB for frequency ranges about 800 MHz.

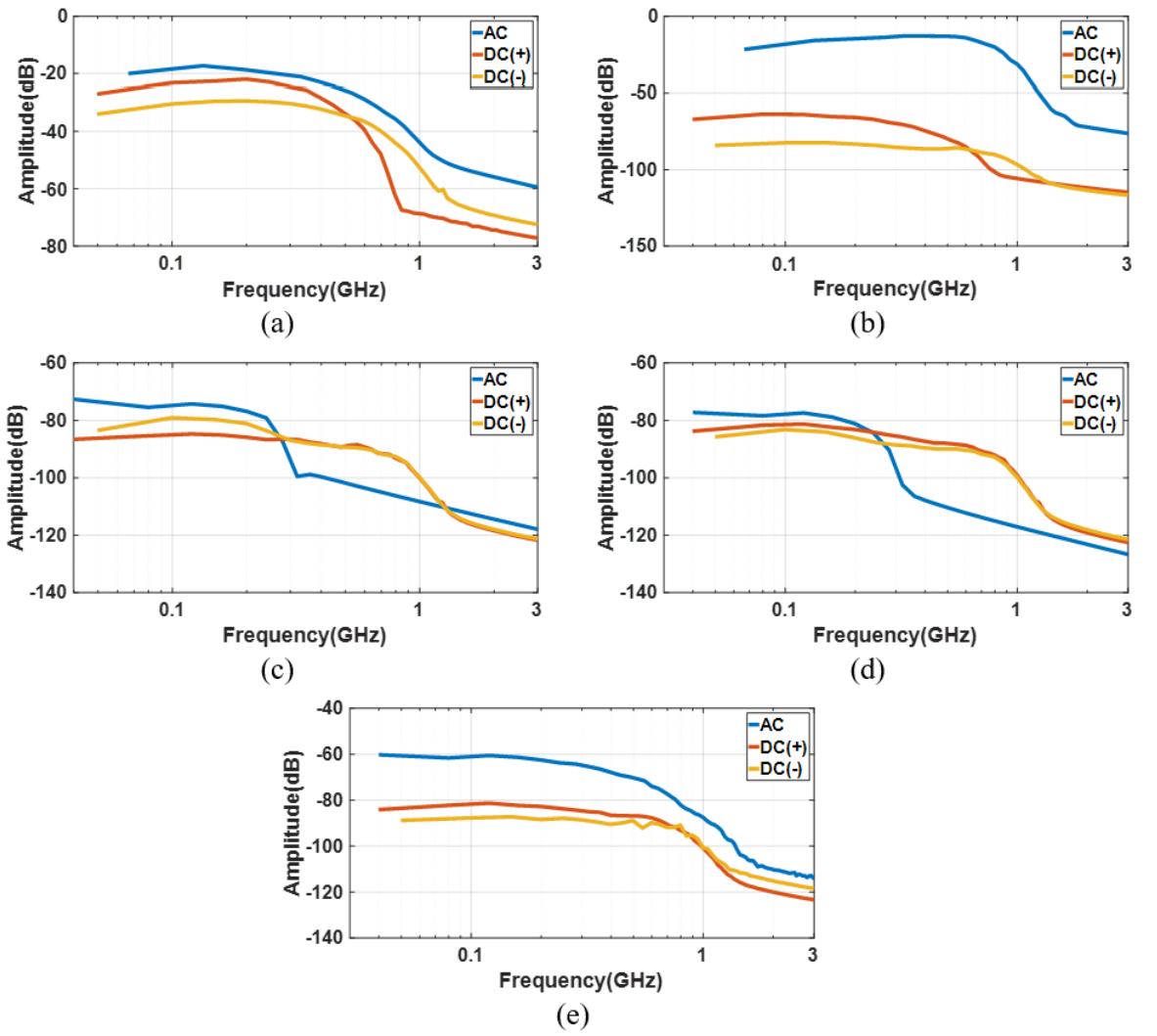

Figure 8.14 The frequency spectrum of individual PD pulses were measured with the D-dot sensor under AC and DC voltage stresses. (a) cavity discharge, (b) surface discharge, (c) negative corona discharge, (d) positive corona discharge, (e) floating potential discharge.

The comparison of surface discharges pulses in Figure 8.14b denotes the significant differences between AC and DC pulses. The surface discharge under AC has components higher -40 dB by 1 GHz. Contrarily, the DC pulses have low amplitudes between -50 dB to -100 dB for frequencies below 1 GHz. Moreover, it should be noted the DC induced pulses have lower

frequency components in the range of 2 MHz. The results of corona discharges represent the higher frequency components in the case of DC pulses. However, both AC and DC pulses have low amplitude for most ranges of frequency. It confirms when the PD signal has low amplitudes that should be difficult to distinguish corresponding pulses from external disturbances. Finally, in floating particle discharge, both AC and DC spectrums have the same trends with a 20 dB difference. The AC pulses have a higher amplitude.

Moreover, Figure 8.15 demonstrates the FFT results of PD pulses were measured by the B-dot sensor. Similarly, the FFT analysis of B-dot output represents a similar trend for all AC and DC voltage stresses. In this photo, the dotted yellow line shows the actual output of the B-dot sensor without utilizing digital filtration.

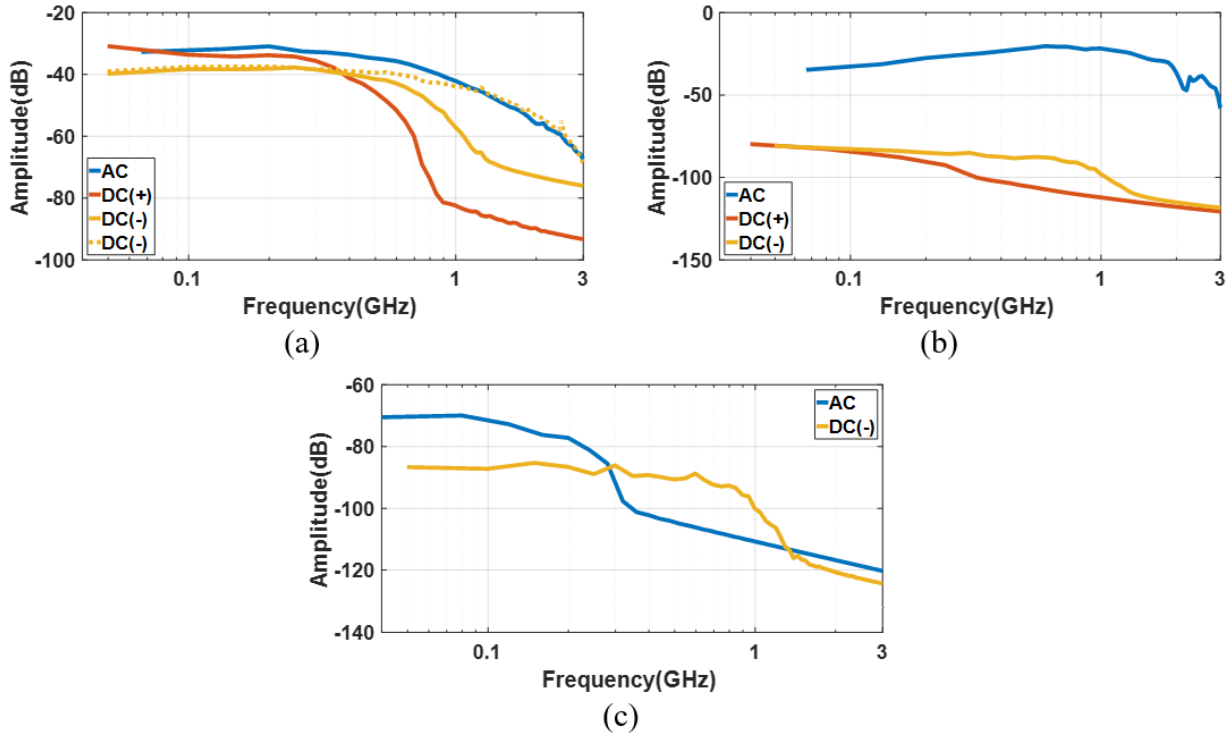

Figure 8.15 The frequency spectrum of individual PD pulses were measured with the B-dot sensor under AC and DC voltage stresses. (a) cavity discharge, (b) surface discharge, (c) floating potential discharge.

The digital filtration is an ability of the oscilloscope and was applied to the output of B-dot and D-dot sensors in some cases to improve the SNR value of their responses. Figure 8.15b also depicts the discriminations of surface discharge AC and DC PD pulses. According to this photo, the DC(-) pulses have a higher amplitude for longer frequencies. Lastly, Figure 8.15c shows the results of a floating particle discharge FFT analysis. As seen in the figure, the AC PD pulses have higher amplitudes than DC(-) for frequencies up to 200 MHz, and after that, because of applying, the filtration drops below -100 dB.

8.4 CLASSIFYING PARTIAL DISCHARGE PULSES

Understanding the PD discharge mechanisms and their waveform characteristics provide valuable information about each type of PD discharge. However, finding ways to distinguish the types of PDs has greater practical value. In Figures 8.16 to 8.18, we present results that could lead to developing methods of identifying PD pulses. In those figures, all types of PD under AC, DC(+), and DC(-) are clustered versus their amplitudes. Despite the scattering in the amplitude of PD discharges, which is linked to the strength of their discharge mechanisms, the PD pulses can be divided into several groups based on their timing characteristics. Figures show the scattered plot of all AC- and DC-induced pulse rise time, decay time, and 20% pulse width parameters versus their amplitudes. Also, the color scaled area represents the normalized density distribution (i.e., occurrence) of data, facilitating the identification of regions with the highest probabilities. As shown in Figure 8.16, scattered plots of rising time, decay time, and 20% pulse width versus their amplitudes resulted in easily identifiable clusters of AC PD pulses.

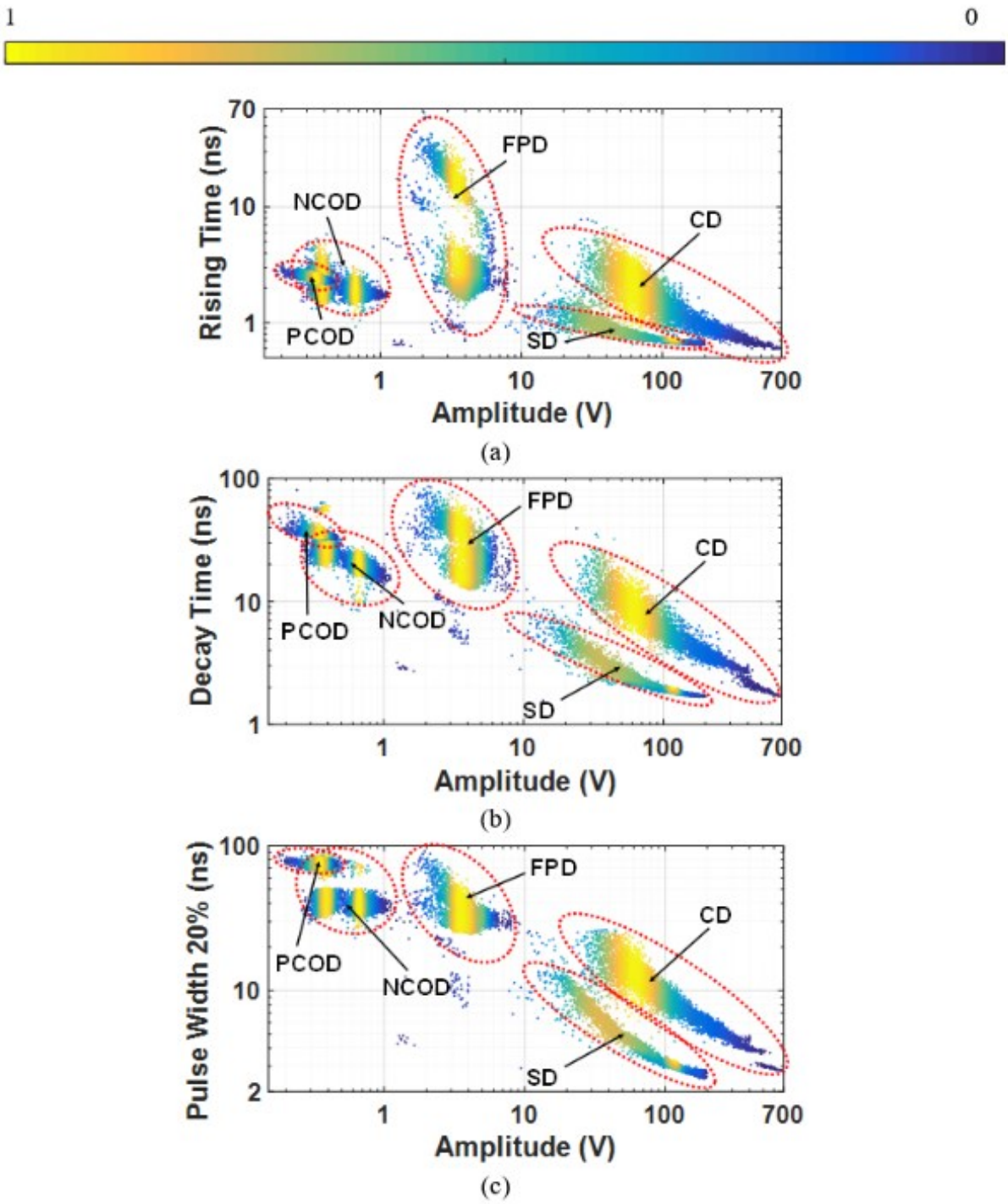

Figure 8.16 Normalized relative density clustering of partial discharge pulses were measured by 50 Ω input channel of oscilloscope under AC voltage stresses. CD, cavity discharge; SD, surface discharge; NCOD, negative corona discharge; PCOD, positive corona discharge; FPD, floating potential discharge.

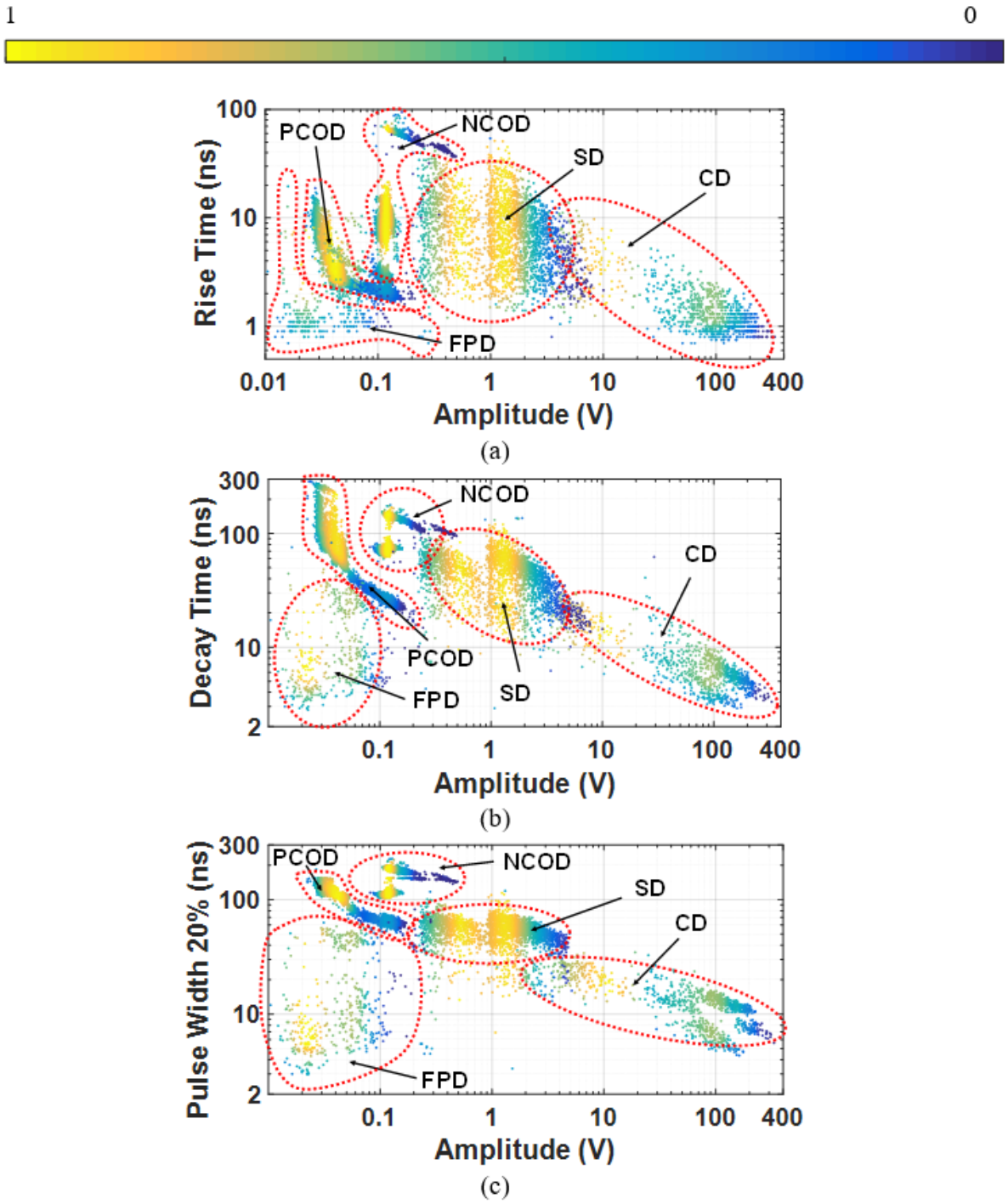

Figure 8.17 Normalized relative density clustering of partial discharge pulses were measured by 50 Ω input channel of oscilloscope under DC(+) voltage stresses. CD, cavity discharge; SD, surface discharge; NCOD, negative corona discharge; PCOD, positive corona discharge; FPD, floating potential discharge.

The cavity discharge and Surface discharge pulses both have high amplitude pulse, but their scattered timing parameters can distinguish them easily from each other. Due to the distinct ranges of amplitude for floating potential discharges and corona discharges, they can be distinguished. Although there are some overlaps in the amplitudes of NCOD and PCOD signals, they can be categorized by td and t20%. Similarly, in Figure 8.17, the normalized density plot of DC(+)-induced pulses shows different clusters for each type of PD without any significant overlaps among them.

As shown, due to the higher amplitudes, the cavity discharge and surface discharge are separated from the rest of the pulses and each other. As found earlier, the amplitude of DC-induced pulses is significantly smaller than that of AC. This significant difference among the amplitude of recorded PD signal could be related to the differences among the discharge mechanisms under AC and DC stress, because the reported inception voltages present the DC PD pulses have higher inception voltages than AC-induced pulses. However, the cavity discharge and surface discharge still have strong pulses as in AC due to their discharge mechanisms. Moreover, negative and positive corona discharges can be distinguished easily from themselves and the floating potential discharges in DC (+) regarding their various amplitude and scattered timing parameters. Furthermore, in the case of DC(-) voltages, as shown in Figure 8.18, cavity discharge pulses have larger amplitudes than other types of PDs, which can be utilized in distinguishing them from the rest of the PD types.

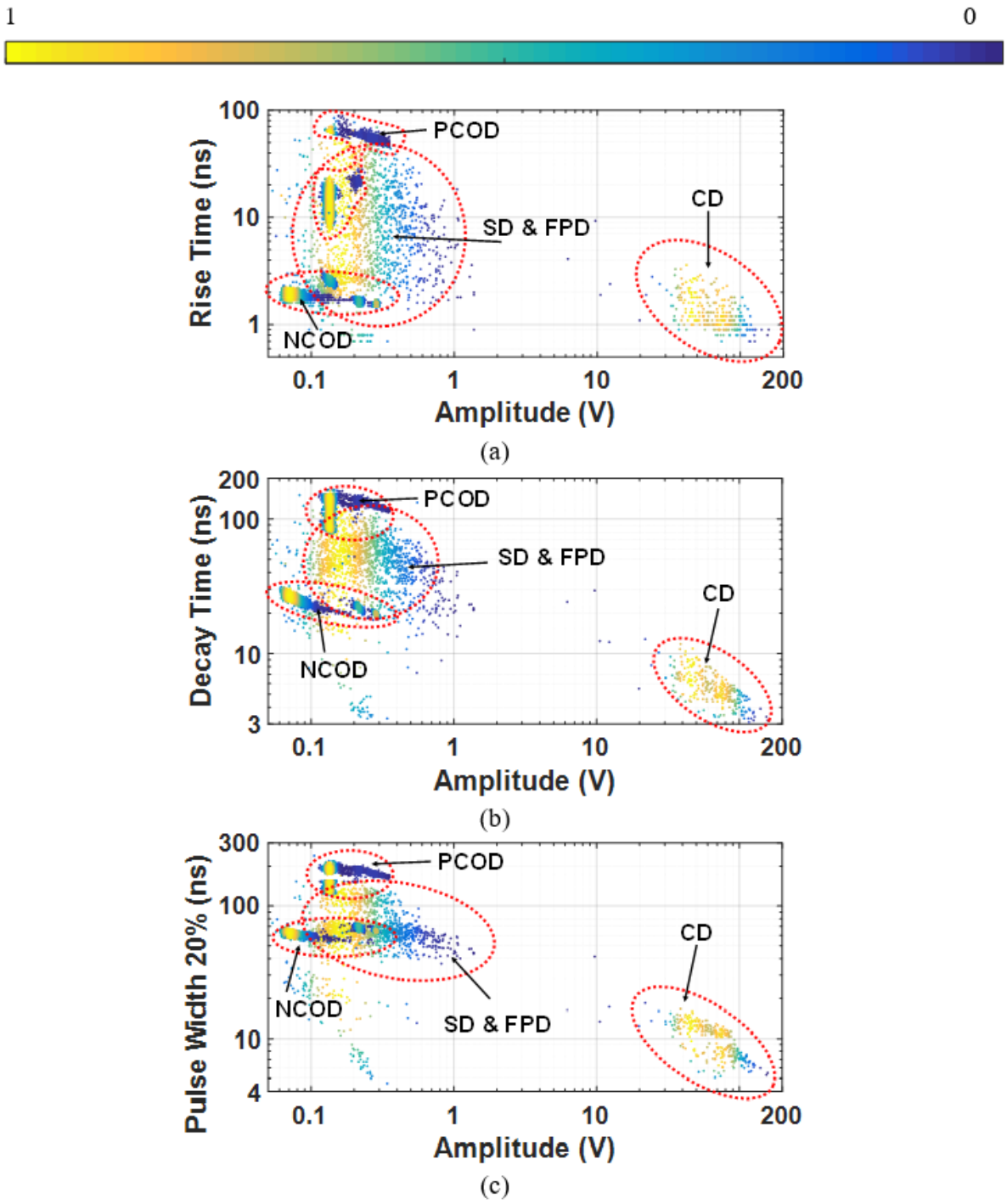

Figure 8.18 Normalized relative density clustering of partial discharge pulses were measured by 50 Ω input channel of oscilloscope under DC(-) voltage stresses. CD, cavity discharge; SD, surface discharge; NCOD, negative corona discharge; PCOD, positive corona discharge; FPD, floating potential discharge.

Nevertheless, due to the overlap of surface discharge and floating potential discharge signal amplitudes, they are not dissectible from each other. Although it seems difficult to distinguish surface discharge and floating potential discharge pulses in DC(-), they can be distinguished based on their main causes. That is, since floating potential discharges are mostly caused within liquids and gases, they can be separated from surface discharge sources. Moreover, the analysis of corona discharges represents that they can be easily distinguished from themselves and other PD sources utilizing their different timing characteristics.

8.5 Summary

This Chapter performed a comprehensive quantitative analysis of individual PD pulses under both AC and DC voltages. The comparison of PD waveshapes under AC and DC demonstrates an obvious difference related to their amplitudes, which were lower in DC stresses.

The time and frequency domains results of measured PD waveforms demonstrated an obvious difference among AC, DC(+), and DC(-) stresses. Time-domain results represented, except for cavity discharge pulses in AC and DC, which were different only in their amplitude most of the DC PD pulses accompanied by longer discharge lengths and lower amplitudes. Also, except for cavity and surface discharges, there was a clear disagreement among DC polarities discharges. Similarly, the results of frequency domain analysis presented except for cavity discharge pulses, the rest of the corresponding PD defects accompanied by higher frequency components under AC voltage stresses. Furthermore, the results of mapping the timing characteristics of PD waveforms measured by the 50 Ω input channel of an oscilloscope versus their amplitude lead to clustering various types of PD for either AC, positive DC, or negative DC.

CHAPTER IX

CONCLUSION

This dissertation focused on understanding the requirements for the precise measurement of individual PD pulses through design, simulation, and experimental investigations to identify various PD sources under both AC and DC voltage stresses through the analysis of their time and frequency domain characteristics.

A unique testbed was designed and constructed in compliance with IEC 60270 to avoid various limitations of PD pulse measurements. The testbed includes a high bandwidth transmission line, which provides an even 50 Ω path for propagating PD pulses by 2.2 GHz. It has been proven that the transmission lines with insufficient bandwidth cause attenuation and distortion of the original waveshape of individual PD pulses. Also, as the successful measurement of PD waveshapes requires high frequency sensors, two types of electromagnetic field sensors (D-dot and B -dot) were designed to absorb the propagated electromagnetic fields of PD through the transmission line. Moreover, the induced discharge current of PD activities was directly measured through the 50 Ω input channel of the oscilloscope, which was considered the reference signal for evaluating the D-dot and B-dot performance.

In general, the time domain results suggest that the developed D-dot and B-dot sensors capture the transients of individual PD pulses effectively. The two electromagnetic field sensors (D-dot and B-dot) were reliable for the measurements of PD waveshape time characteristics,

including rising time, decay time, 50% pulse width, and 20% pulse width. Moreover, for the statistical analysis of individual PD pulses, four well-known types of PD sources – corona, cavity, surface, and floating potential discharge sources – were prepared and utilized for investigating the corresponding waveshapes. Thousands of individual PD pulses were recorded under the AC, positive DC, and negative DC stresses. The comparison of time characteristics of recorded data showed obvious distinctions among the behaviors of AC and DC PDs. The differences are related to the various discharge mechanisms inside the insulating media, which result in the corresponding PD waveform characteristics. Based on the identified differences among the PD characteristics under both AC and DC stresses and based on the various discharge intensities among the PD types, we could classify various types of PDs solely using their waveshape parameters. One of the advantages of this method is its independence from the repetition rate information of PD pulses under DC stresses, which takes a long time to record. The other advantage of this mapping is that the identification of PD can be performed by utilizing the rise time, decay time, and pulse width of PD waveforms.

It has been shown in this dissertation that the precise measurement of PD waveshapes require a high bandwidth measurement circuits as well as high frequency sensors. The accurate measurement of individual PD waveshapes provides useful information such as discharge mechanisms and intensity of discharge. Consequently, the technologies developed in this dissertation enable the classification of various types of DC and AC PDs.

CHAPTER X

FUTURE WORK

As discussed in this dissertation, the sensitivity of D-dot and B-dot sensors depends on the design and location of sensors. Therefore, they can be designed in the future works to be more applicable for practical applications such as GIS substation PD measurements that deals with issues such as detecting mobile particle movements. One of the advantages of GIS systems is their coaxial designs, which provide a waveguide for traveling of PD signals. Also, the performance of the designed sensors can be evaluated in case of dealing with other types of insulating media, e.g., liquid and solids. Indeed, the differences in electromagnetic wave propagations within this media require special attention for the accurate design of D-dot and B-dot sensors. Besides, the lower intensity of DC PD pulses compare to that of AC PD pulses limits certain methods of PD detection. To overcome this limitation, other plausible parameters of PD waveshapes, e.g., their integral (area under waveform), or energy of each pulse, can be studied in the future works to distinguish various types of PDs with more confidence.

CHAPTER XI

LIST OF PUBLICATIONS

Journal Papers

J1. **M. Rostaghi-Chalaki**, K. Yousefpour, J. P. Donohoe, M. Kurum, J. V. Kluss, and C. Park, "Design of Transmission Line and Electromagnetic Field Sensors for DC Partial Discharge Analysis.", IEEE Transactions on Dielectrics and Electrical Insulation, 2020. (**Accepted**)

J2. **M. Rostaghi-Chalaki**, K. Yousefpour, J. V. Kluss, M. Kurum, J. P. Donohoe, and C. Park, "Classification and Comparison of AC and DC Partial Discharges by Pulse Waveform Analysis," Elsevier International Journal of Electrical Power and Energy Systems, 2020. (**Published**)

Conference Papers

C1. **M. Rostaghi-Chalaki**, K. Yousefpour, Z. Ahmed, C. Park, "Transmission Line Design for Individual Partial Discharge Waveshape Measurement." 2020 IEEE Electrical Insulation Conference (EIC), 2020. (**Published**)

C2. J. V. Kluss, M. **Rostaghi-Chalaki**, and Z. Ahmed, "Influence of Sensor Selection for Observing Individual Partial Discharge Waveforms." The International Symposium on High Voltage Engineering. Springer, Cham, 2019. (**Published**)

REFERENCES

[1] E. Gulski and et. al, *Guidelines for partial discharge detection using conventional (IEC 60270) and unconventional methods*. Paris: CIGRÉ, 2016.

[2] R. Piccin, A. R. Mor, P. Morshuis, A. Girodet, and J. Smit, "Partial discharge analysis of gas insulated systems at high voltage AC and DC," *IEEE Trans. Dielectr. Electr. Insul.*, vol. 22, no. 1, pp. 218–228, Feb. 2015, doi: 10.1109/TDEI.2014.004711.

[3] H. Illias, Teo Soon Yuan, A. H. A. Bakar, H. Mokhlis, G. Chen, and P. L. Lewin, "Partial discharge patterns in high voltage insulation," in *2012 IEEE International Conference on Power and Energy (PECon)*, Dec. 2012, pp. 750–755, doi: 10.1109/PECon.2012.6450316.

[4] R. Aldrian, G. C. Montanari, A. Cavallini, and Suwarno, "Signal separation and identification of partial discharge in XLPE insulation under DC voltage," in *2017 1st International Conference on Electrical Materials and Power Equipment (ICEMPE)*, May 2017, pp. 53–56, doi: 10.1109/ICEMPE.2017.7982098.

[5] G. C. Montanari, P. Seri, R. Ghosh, and L. Cirioni, "Noise rejection and partial discharge source identification in insulation system under DC voltage supply," *IEEE Trans. Dielectr. Electr. Insul.*, vol. 26, no. 6, pp. 1894–1902, Dec. 2019, doi: 10.1109/TDEI.2019.008210.

[6] P. H. F. Morshuis, "Partial discharge mechanisms: Mechanisms leading to breakdown, analyzed by fast electrical and optical measurements," 1993, Accessed: Sep. 10, 2020. [Online]. Available: https://repository.tudelft.nl/islandora/object/uuid%3A5e39ece9-bcb1-40e0-8501-cfb963873a78.

[7] Y. Li, K. Zhou, G. Y. Zhu, and Q. G. Zhang, "Effect of DC discharges in mineral oil on degradation characteristics of oil-impregnated pressboard," *IEEE Trans. Dielectr. Electr. Insul.*, vol. 26, no. 5, pp. 1701–1708, Oct. 2019, doi: 10.1109/TDEI.2019.008256.

[8] N. Morette, T. Ditchi, and Y. Oussar, "Feature extraction and ageing state recognition using partial discharges in cables under HVDC," *Electr. Power Syst. Res.*, vol. 178, p. 106053, Jan. 2020, doi: 10.1016/j.epsr.2019.106053.

[9] A. Abbasi *et al.*, "Progress on Partial Discharge Detection under DC Voltage Stress," New Delhi (India), Nov. 2019, pp. 69–76.

[10] A. Pirker and U. Schichler, "Partial discharges at DC voltage - measurement and pattern recognition," in *2016 International Conference on Condition Monitoring and Diagnosis (CMD)*, Sep. 2016, pp. 287–290, doi: 10.1109/CMD.2016.7757811.

[11] S. Abdul Madhar, P. Mraz, A. Rodrigo Mor, and R. Ross, “Physical interpretation of the floating conductor defect patterns under AC and DC stress conditions,” *Int. J. Electr. Power Energy Syst.*, vol. 118, p. 105733, Jun. 2020, doi: 10.1016/j.ijepes.2019.105733.

[12] H. Saadati, P. Werle, J. M. Seifert, E. Gockenbach, and H. Borsi, “Fundamental Difference of Partial Discharge Phenomena under AC and DC Stresses,” in *2018 IEEE International Conference on High Voltage Engineering and Application (ICHVE)*, Sep. 2018, pp. 1–4, doi: 10.1109/ICHVE.2018.8642207.

[13] Z. Cao, Y. Bai, Y. Zhou, G. Wei, Y. Zhang, and J. Wang, “An Investigation of Negative DC Partial Discharge Decomposition of SF6 Under Different Metal Materials,” *IEEE Access*, vol. 8, pp. 35105–35112, 2020, doi: 10.1109/ACCESS.2020.2974536.

[14] I. R. Velo, “Experimental Set-up for partial discharge detection,” *115*, 2015, Accessed: Sep. 10, 2020. [Online]. Available: https://ntnuopen.ntnu.no/ntnu-xmlui/handle/11250/2368008.

[15] W. Zhao, “Partial discharge ageing of polymer insulation under combined AC and DC stress at elevated temperatures,” Ph.D., University of Strathclyde, 2017.

[16] Kreuger, F.H. and Gulski, E., “Computer-aided recognition of partial dicharges using statistical tools,” Delft University Press, 1991.

[17] M. He, “Research in field distortion by cavity presence in HVDC cable and the associated partial discharge characteristics,” masters, University of Southampton, 2016.

[18] A. Mraihi, N. Merbahi, M. Yousfi, A. Abahazem, and O. Eichwald, “Electrical and spectroscopic analysis of mono- and multi-tip pulsed corona discharges in air at atmospheric pressure,” *Plasma Sources Sci. Technol.*, vol. 20, no. 6, p. 065002, Nov. 2011, doi: 10.1088/0963-0252/20/6/065002.

[19] P. H. F. Morshuis and J. J. Smit, “Partial discharges at DC voltage: their mechanism, detection and analysis,” *IEEE Trans. Dielectr. Electr. Insul.*, vol. 12, no. 2, pp. 328–340, Apr. 2005, doi: 10.1109/TDEI.2005.1430401.

[20] E. Lemke, “Using a field probe to study the mechanism of partial discharges in very small air gaps under direct voltage,” *IEEE Electr. Insul. Mag.*, vol. 32, no. 4, pp. 43–51, Jul. 2016, doi: 10.1109/MEI.2016.7528989.

[21] E. Lemke, “A critical review of partial-discharge models,” *IEEE Electr. Insul. Mag.*, vol. 28, no. 6, pp. 11–16, Nov. 2012, doi: 10.1109/MEI.2012.6340519.

[22] Z. Ahmed, “Analysis and De-Noising of Partial Discharge Signals in Medium Voltage XLPE Cables,” Feb. 2016, Accessed: Sep. 10, 2020. [Online]. Available: https://aaltodoc.aalto.fi:443/handle/123456789/19888.

[23] J. V. Kluss, M. R. Chalaki, and Z. Ahmed, “Influence of Sensor Selection for Observing Individual Partial Discharge Waveforms,” in *Proceedings of the 21st International Symposium on High Voltage Engineering*, Cham, 2020, pp. 680–692.

[24] T. Klueter, J. Wulff, and F. Jenau, “Time domain analysis of partial discharges at DC voltage in air and insulation oil,” in *2013 12th International Conference on Environment and Electrical Engineering*, May 2013, pp. 308–312, doi: 10.1109/EEEIC.2013.6549532.

[25] T. Klueter, J. Wulff, and F. Jenau, “Measurement and statistical analysis of Partial Discharges at DC voltage,” in *2013 48th International Universities’ Power Engineering Conference (UPEC)*, Sep. 2013, pp. 1–5, doi: 10.1109/UPEC.2013.6714912.

[26] T. Klueter, J. Wulff, F. Jenau, and D. Wienold, “Evaluation of surface- and corona discharges at DC voltage,” in *2013 13th International Conference on Environment and Electrical Engineering (EEEIC)*, Nov. 2013, pp. 255–259, doi: 10.1109/EEEIC-2.2013.6737918.

[27] U. Fromm, “Partial discharge and breakdown testing at high DC voltage.,” p. 1, 1997.

[28] IEC 60270, *High-voltage test techniques — Partial discharge measurements*, Third edition. 2000.

[29] F. P. Mohamed, W. H. Siew, J. J. Soraghan, S. M. Strachan, and J. Mcwilliam, “The use of power frequency current transformers as partial discharge sensors for underground cables,” *IEEE Trans. Dielectr. Electr. Insul.*, vol. 20, no. 3, pp. 814–824, Jun. 2013, doi: 10.1109/TDEI.2013.6518951.

[30] M. Muhr and et. al, *SENSORS AND SENSING USED FOR NON-CONVENTIONAL PD DETECTION*, vol. D1-102. CIGRE 2006.

[31] J. C. Hernandez and J. Perkel, “Partial Discharge (PD) HV and EHV Power Cable Systems,” in *Cable Diagnostic Focused Initiative (CDFI)*, Georgia Tech Research Corporation (NEETRAC), 2016.

[32] M. D. Judd, O. Farish, and B. F. Hampton, “The excitation of UHF signals by partial discharges in GIS,” *IEEE Trans. Dielectr. Electr. Insul.*, vol. 3, no. 2, pp. 213–228, Apr. 1996, doi: 10.1109/94.486773.

[33] S. Meijer, E. Gulski, and J. J. Smit, “Pattern analysis of partial discharges in SF/sub 6/ GIS,” *IEEE Trans. Dielectr. Electr. Insul.*, vol. 5, no. 6, pp. 830–842, Dec. 1998, doi: 10.1109/94.740764.

[34] M. Elborki, N. Jenkins, P. Crossley, and Z. Wang, “Power transformer PD sources determination using current signals waveshape and pattern distributions,” in *Conference Record of the 2004 IEEE International Symposium on Electrical Insulation*, Sep. 2004, pp. 178–181, doi: 10.1109/ELINSL.2004.1380508.

[35] A.-R. A. M. Makky, H. Abo-Zied, F. N. Abdelbar, and P. Mutschler, “Design of the instrument current transformer for high frequency high power applications,” in *2008 12th International Middle-East Power System Conference*, Mar. 2008, pp. 230–233, doi: 10.1109/MEPCON.2008.4562343.

[36] T. C. Wagoner *et al.*, “Differential-output B-dot and D-dot monitors for current and voltage measurements on a 20-MA, 3-MV pulsed-power accelerator,” *Phys. Rev. Spec. Top. - Accel. Beams*, vol. 11, no. 10, p. 100401, Oct. 2008, doi: 10.1103/PhysRevSTAB.11.100401.

[37] M. M. Weiner, *Monopole Antennas*. CRC Press, 2003.

[38] “Monopole – MicrowaveTools.” http://www.microwavetools.com/monopole/ (accessed Sep. 11, 2020).

[39] M. Hikita, S. Ohtsuka, and S. Matsumoto, “Recent trend of the partial discharge measurement technique using the UHF electromagnetic wave detection method,” *IEEJ Trans. Electr. Electron. Eng.*, vol. 2, no. 5, pp. 504–509, 2007, doi: 10.1002/tee.20201.

[40] J. Lin *et al.*, “Propagation Characteristics of Partial Discharge Pulses in the Cable,” *J. Power Energy Eng.*, vol. 02, no. 09, pp. 112–116, 2014, doi: 10.4236/jpee.2014.29016.

[41] T. Takahashi *et al.*, “AC and DC partial discharge measurements on defective cables,” in *2016 IEEE Electrical Insulation Conference (EIC)*, Jun. 2016, pp. 375–378, doi: 10.1109/EIC.2016.7548617.

[42] “Near and far field,” *Wikipedia*. Jun. 08, 2020, Accessed: Sep. 11, 2020. [Online]. Available: https://en.wikipedia.org/w/index.php?title=Near_and_far_field&oldid=961458165.

[43] A. Bojovschi, W. S. T. Rowe, and A. K. L. Wong, “Electromagnetic Field Intensity Generated by Partial Discharge in High Voltage Insulating Materials,” *Prog. Electromagn. Res.*, vol. 104, pp. 167–182, 2010, doi: 10.2528/PIER10010803.

[44] P. H. F. Morshuis, “Time-resolved discharge measurements,” in *1993 International Conference on Partial Discharge*, Sep. 1993, pp. 43–46.

[45] C. S. Chang, K. H. Lee, and C. Chang, “Recognition of partial discharge waveshape patterns for gas insulated switchgear,” *Aust. J. Electr. Electron. Eng.*, vol. 2, no. 3, pp. 191–197, Jan. 2005, doi: 10.1080/1448837X.2005.11464128.

[46] C. B. Soh, C. K. Liew, S. Y. Cao, K. J. Tseng, P. M. Z. Low, and W. L. Woo, “Partial Discharge Simulation and Detection in 750V DC XLPE Cables,” in *2019 Joint International Symposium on Electromagnetic Compatibility, Sapporo and Asia-Pacific International Symposium on Electromagnetic Compatibility (EMC Sapporo/APEMC)*, Jun. 2019, pp. 391–394, doi: 10.23919/EMCTokyo.2019.8893657.

[47] J. Kim, D. Kim, K. Nam, W. Choi, B. Lee, and J. Koo, “Characteristics of partial discharge by AC and DC,” in *2012 IEEE International Conference on Condition Monitoring and Diagnosis*, Sep. 2012, pp. 489–492, doi: 10.1109/CMD.2012.6416185.

[48] K. Takabayashi, R. Nakane, H. Okubo, and K. Kato, “High voltage DC partial discharge and flashover characteristics with surface charging on solid insulators in air,” *IEEE Electr. Insul. Mag.*, vol. 34, no. 5, pp. 18–26, Sep. 2018, doi: 10.1109/MEI.2018.8445431.

[49] T. Klueter, J. Wulff, F. Jenau, and D. Wienold, “Evaluation of surface- and corona discharges at DC voltage,” in *2013 13th International Conference on Environment and Electrical Engineering (EEEIC)*, Nov. 2013, pp. 255–259, doi: 10.1109/EEEIC-2.2013.6737918.

[50] Xiaohua Li, Guangning Wu, Xueqin Zhang, and Shanshan Bian, “Partial discharge pulse shape detection and analysis under DC condition,” in *2007 Electrical Insulation Conference and Electrical Manufacturing Expo*, Oct. 2007, pp. 48–51, doi: 10.1109/EEIC.2007.4562586.

[51] G. Hoogenraad and J. Beyer, “Digital HVDC partial discharge testing,” in *Conference Record of the 2000 IEEE International Symposium on Electrical Insulation (Cat. No.00CH37075)*, Apr. 2000, pp. 448–451, doi: 10.1109/ELINSL.2000.845545.

[52] G. Hoogenraad, P. H. F. Morshuis, and C. Petrarca, “Classification of partial discharges for DC equipment,” in *Proceedings of Conference on Electrical Insulation and Dielectric Phenomena - CEIDP ’96*, Oct. 1996, vol. 1, pp. 110–112 vol.1, doi: 10.1109/CEIDP.1996.564608.

[53] R. Sarathi and G. Koperundevi, “UHF technique for identification of partial discharge in a composite insulation under AC and DC voltages,” *IEEE Trans. Dielectr. Electr. Insul.*, vol. 15, no. 6, pp. 1724–1730, Dec. 2008, doi: 10.1109/TDEI.2008.4712677.

[54] M. R. Chalaki, K. Yousefpour, Z. Ahmed, and C. Park, “Transmission Line Design for Individual Partial Discharge Waveshape Measurement,” in *2020 IEEE Electrical Insulation Conference (EIC)*, Jul. 2020, pp. 554–557, doi: 10.1109/EIC47619.2020.9158721.

[55] D. I. L. de Villiers, P. W. van der Walt, and P. Meyer, “Design of a Ten-Way Conical Transmission Line Power Combiner,” *IEEE Trans. Microw. Theory Tech.*, vol. 55, no. 2, pp. 302–308, Feb. 2007, doi: 10.1109/TMTT.2006.890065.

[56] T. Huiskamp, F. J. C. M. Beckers, E. J. M. van Heesch, and A. J. M. Pemen, “B-Dot and D-Dot Sensors for (Sub)Nanosecond High-Voltage and High-Current Pulse Measurements,” *IEEE Sens. J.*, vol. 16, no. 10, pp. 3792–3801, May 2016, doi: 10.1109/JSEN.2016.2530841.